UNIVERSITY OF CALIFORNIA

Santa Barbara

Precision Optical Phase Synchronization Over Fiber Links Using Spectrally Pure, Chip-Scale Lasers

A dissertation submitted in partial satisfaction of the

requirements for the degree Doctor of Philosophy

in Electrical and Computer Engineering

by

Grant Matthew Brodnik

Committee in charge:

Professor Daniel J. Blumenthal, Chair

Professor John. E. Bowers

Professor Scott. B. Papp

Professor Luke S. Theogarajan

March 2022

The dissertation of Grant Matthew Brodnik is approved.

_____

Professor John E. Bowers

_____

Professor Scott B. Papp

_____

Professor Luke Theogarajan

_____

Professor Daniel J. Blumenthal, Committee Chair

December 2021

Precision Optical Phase Synchronization Over Fiber Links Using Spectrally Pure, Chip-Scale Lasers

by

Grant M. Brodnik

ACKNOWLEDGEMENTS

First and foremost, I extend my sincere gratitude to my advisor and mentor, Professor Daniel J. Blumenthal. These years in Santa Barbara marked a pivotal moment in my career, and truly, my life. I thank Dan for his constant support, guidance, and his belief in me and my potential through these years. I will cherish the late nights (often into early mornings) at Dan's house working hard on publications with lab mates and a side of pizza or burgers. Dan has instilled in me the work ethic and curiosity-driven approach to research that will continue to motivate me in my career – though the life lessons I will take with me from Santa Barbara extend well beyond the laboratory and classroom. I would next like to thank my committee members, Professor John Bowers and Professor Luke Theogarajan from here at UCSB and Professor Scott Papp from NIST / CU Boulder. Their support – whether it be through thoughtful discussion, kind encouragement, or by providing state-of-art devices to incorporate in the experiments that enabled this body of work – was instrumental in my success and I am grateful for their guidance over these years.

In my early days in the Optical Communications and Photonic Integration (OCPI) Group, I had the pleasure and fortune of learning from the current OCPI students and researchers – Michael Belt, Taran Huffman, Sarat Gundavarapu, and Renan Moreira. In particular, I'd like to thank Sarat Gundavarapu for teaching me the skills to be successful in the lab and for being a great friend. We spent countless days and nights together working on experiments (while eating pizza and burritos – the secret to success) and I will forever cherish those memories. I'd also like to thank Cátia Pinho for her support and guidance through our shared photonics experiments during her time at UCSB as a visiting scholar. Throughout the remainder of my time with the OCPI group, I was able to share the PhD experience with wonderful OCPI colleagues and friends: Mark Harrington, Nitesh Chauhan, Debapam Bose, Jiawei Wang, Andrei Isichenko, Kaikai Liu, and Qiancheng Zhao. These relationships made each day an adventure and joy, and I look forward to staying in touch as the years continue. Beyond the OCPI group, I'd like to thank John Dallyn and Professor Ryan Behunin from Northern Arizona University, and Dr. Paul Morton of Morton Photonics for their support. I will miss our shared meetings, discussions, publications, and collaborations – though I am

hopeful for more over the years! I'd also like to thank Andy Netherton, Akshar Jain, Songtao Liu, Duanni Huang, Minh Tran, Joel Guo, and all the other students and researchers that contributed to the devices and experiments that are incorporated in this body of work.

I am grateful to Emily Jensen for her limitless support and encouragement over these years and for being such an important part of my life. There are countless others along the grad journey that made this time at UCSB a truly wonderful, life-changing experience. I look forward to our continued friendships that began here in Santa Barbara.

Finally, I thank my parents and brothers for their unending support – though the extent of their impact is impossible to capture in words. From a young age, I have been encouraged to pursue passion and curiosity. This has shaped my journey and brought me here to this day, where I have the incredible fortune of continuing a career in something I love and that brings me true joy.

Dedicated to my family

VITA OF GRANT MATTHEW BRODNIK

December 2021

EDUCATION

Doctor of Philosophy in Electrical and Computer Engineering *Dec '21*
University of California, Santa Barbara
Doctoral Advisor: Prof. Daniel J. Blumenthal

Master of Science, Optical Engineering *Aug '16*
Rose-Hulman Institute of Technology
M.Sc. Advisor: Paul O. Leisher, PhD

Master of Science, Mechanical Systems Design Engineering *Aug '16*
Seoul National University of Science and Technology

Bachelor of Science, Optical Engineering *May '14*
Rose-Hulman Institute of Technology
Major: Optical Engineering
Minor: Electrical Engineering

PROFESSIONAL EMPLOYMENT

Graduate Student Researcher *Sep '16 - Dec '21*
Dept. ECE, University of California, Santa Barbara

PhD. Student Research Intern *Jun '18 – Sep '18*
Microsoft Research Lab, Cambridge, UK

PhD. Student Researcher *Jun '15 – Sep '15*
Korea Institute of Science and Technology, Seoul, Korea

Graduate Student Researcher, Grader *Jun '14 –Aug '16*
Rose-Hulman Institute of Technology

PUBLICATIONS

G. M. Brodnik, M. W. Harrington, J. H. Dallyn, D. Bose, W. Zhang, L. Stern, P. A. Morton, R. O. Behunin, S. B. Papp, D. J. Blumenthal. "Optically synchronized fibre links using spectrally pure chip-scale lasers." Nature Photonics 15, 588-593 (2021)

K. Liu, J. H. Dallyn, **G. M. Brodnik**, A. Isichenko, M. W. Harrington, N. Chauhan, D. Bose, P. A. Morton, S. B. Papp, R. O. Behunin, D. J. Blumenthal. "Photonic circuits for

laser stabilization with ultra-low-loss and nonlinear resonators." arXiv:2107.03595 [physics] (2021)

K. Liu, **G. M. Brodnik**, M. W. Harrington, A. Isichenko, Q. Zhao, J. H. Dallyn, R. O. Behunin, P. Morton, S. B. Papp, D. J. Blumenthal. "Self-similar ultra-high Q Si3N4 integrated resonators for Brillouin laser linewidth narrowing and stabilization." (OFC), Jun.

Q. Zhao, M. W. Harrington, A. Isichenko, **G. M. Brodnik**, K. Liu, R. O. Behunin, P. T. Rakich, C. W. Hoyt, C. Fertig, S. B. Papp, D. J. Blumenthal. "Laser frequency drift stabilization using an integrated dual-mode locking Si3N4 waveguide reference cavity." (CLEO), May 2021. STh2B.7

K. Liu, M. W. Puckett, M. W. Harrington, **G. M. Brodnik**, et. al. "Milliwatt threshold ultra-low linewidth photonic integrated Si3N4 Brillouin laser." (CLEO), May 2021. SF2O.1

G. M. Brodnik et al., "Optically synchronized fiber links with spectrally pure integrated lasers." arXiv:2102.05849 [physics] (2021)

G. M. Brodnik et al., "Ultra-Narrow Linewidth Chip-Scale Heterogeneously Integrated Silicon/III-V Tunable Laser Pumped Si/Si3N4 SBS Laser," in Conference on Lasers and Electro-Optics (CLEO) 2020 STu3M.5

M. W. Harrington, **G. M. Brodnik** et al., "Kerr Soliton Microcomb Pumped by an Integrated SBS Laser for Ultra-Low Linewidth WDM Sources," in (OFC), Mar. 2020, pp. 1–3.

G. M. Brodnik, M. W. Harrington et al., "Chip-Scale, Optical-Frequency-Stabilized PLL for DSP-Free, Low-Power Coherent QAM in the DCI," (OFC) 2020, San Diego, California, 2020, p. M3A.6.

G. M. Brodnik et al., "Widely Tunable Optical Local Oscillator Scheme for RF Photonic Down-Conversion," in 2019 IEEE Avionics and Vehicle Fiber-Optics and Photonics Conference (AVFOP), Nov. 2019, pp. 1–2

M. W. Puckett et al., "Silicon Nitride Ring Resonators with 0.123 dB/m Loss and Q-Factors of 216 Million for Nonlinear Optical Applications," in 2019 (CLEO/Europe-EQEC Jun. 2019, pp. 1–1

S. Gundavarapu, **G. M. Brodnik** et al., "Sub-hertz fundamental linewidth photonic integrated Brillouin laser," Nature Photon, vol. 13, no. 1, pp. 60–67, Jan. 2019

T. A. Huffman, **G. M. Brodnik**, C. Pinho, S. Gundavarapu, D. Baney, and D. J. Blumenthal, "Integrated Resonators in an Ultralow Loss Si3N4/SiO2 Platform for Multifunction Applications," IEEE JSTQE, 24, (2018)

G. M. Brodnik, C. Pinho, F. Chang, and D. J. Blumenthal, "Extended Reach 40km Transmission of C-Band Real-Time 53.125 Gbps PAM-4 Enabled with a Photonic Integrated Tunable Lattice Filter Dispersion Compensator," in Optical Fiber Communication Conference, 2018, p. W2A.30

S. Gundavarapu et al., “Integrated Waveguide Brillouin Laser,” arXiv:1709.04512, pp. 1–15, 2017.

G. M. Brodnik, “Development and Validation of an Empirical Temperature-Dependent Voltage Model for Diode Laser Characterization,” MSc. Physics and Optical Engineering Thesis, Rose-Hulman Institute of Technology, 2016

G. M. Brodnik, S. M. Misak, D. G. Dugmore, E. R. Hale, K. A. Middleton, and P. O. Leisher, “Real-time spectrally-resolved imaging of the transverse modes in broad area diode lasers,” CLEO-PR, (2015).

BOOK CHAPTERS

Demis D. John, **Grant Brodnik**, Sarat Gundavarapu, Renan L. Moreira, Michael Belt, Taran Huffman and Daniel J. Blumenthal, Chapter 11 “Low-Loss Photonic Integration: Applications in Datacenters” in “Datacenter Connectivity Technologies: Principles and Practice”, Frank Chang, Ed. River Publishers, 2018.

ABSTRACT

Precision Optical Phase Synchronization Over Fiber Links Using Spectrally Pure, Chip-Scale Lasers

by

Grant Matthew Brodnik

Ultra-narrow linewidth, stable lasers are instrumental in precision scientific applications spanning optical metrology and spectroscopy, low phase noise optoelectronic microwave generation, comparison of atomic clocks, and sophisticated laser ranging systems. In these application spaces, the low-phase noise and frequency stability afforded by spectrally pure lasers is paramount, enabling distribution of precise optical frequency and phase references to remote locations. The most exquisite of these optical sources typically employ sophisticated, highly engineered environmental isolation systems, often relegating their use to tabletop and laboratory-based implementations and limiting their scope to large-scale experiments. Porting these systems to the chip-scale via photonic integration, while maintaining a tolerable trade-off in performance, can provide innovation across previously independent scientific communities and potentially enable entirely new applications that require compact, low-power operation of spectrally pure optical sources.

This dissertation investigates these chip-scale, ultra-narrow linewidth, frequency stabilized laser systems and demonstrates their use in high performance optical phase

synchronization. To realize such sources, techniques common in atomic clock systems and precision metrology are employed to achieve optical sources with simultaneous 1 Hz fundamental linewidths, 30 Hz integral linewidths, and carrier instability better than $2x10^{-13}$ at 50 ms. In addition to realizing these chip-scale sources, experimental efforts involve precision characterization techniques that required development of suitable in-house systems due to the achieved ultra-low-noise performance that limited the use of commercial instrumentation. Next, two independent sources operated together in a fiber-interconnected pair demonstrate the benefits of employing mutually coherent lasers in the context of distributed optical phase synchronization. This approach, termed an optical-frequency-stabilized phase-locked-loop, is demonstrated with a low residual phase error variance of $3x10^{-4}$ rad^2 using only simple, low bandwidth and low power feedback electronics. Finally, this system is employed for carrier phase synchronization in a high modulation order quadrature-amplitude-modulated (QAM) coherent link. These efforts align with the Frequency Stabilized Coherent Optical (FRESCO) link for low-energy data center interconnects (DCIs) and demonstrate the promise of employing chip-scale, spectrally pure sources in tomorrow's low power, high capacity optical communications.

TABLE OF CONTENTS

LIST OF FIGURES

LIST OF TABLES

1 Introduction

1.1 Spectrally pure lasers and precision metrology

Many of today's precision scientific experiments that aim to expand our understanding of this world employ truly exquisite optical sources with high spectral purity and frequency instabilities better than 1 part in 10^{15}. This extreme performance is achieved using techniques developed to stabilize optical carriers to high finesse, ultra-stable optical reference cavities [1] housed in highly engineered environmental isolation systems [2]–[4]. Because of the complex systems and infrastructure required to achieve this performance, these sources have historically been relegated to table- and laboratory-scale realizations. The belief that these systems would continue to occupy entire optical tables and laboratory spaces motivated the early development of methods for distributing precision optical frequency and phase references over fiber links [5]–[10]. These techniques have been crucial in myriad groundbreaking experiments, such as investigations of fundamental physical constants [7] and searches for dark matter [8], interferometry for radio astronomy [10], [13], optical clock comparison [14], [15], and geodesy [16], [17].

For precision applications that require both local and remote sources operating as a transmitter-receiver pair, however, employing large-scale stable laser systems becomes impractical. Alternatively, standard commercial semiconductor lasers can enable ultra-compact footprints and scalable architectures. However, the large linewidths typically associated with these sources does not lend their use for high spectral purity and mutually

coherent operation that precision applications demand, resulting in additional challenges for recovering optical phase.

Bridging these two worlds by applying the host of techniques used in table scale systems [2]–[4] but in compact forms (recognizing potential performance trade-offs but a net gain in system performance) is a worthwhile endeavor. As such, many exciting research efforts today are aligned with developing narrow linewidth integrated lasers stabilized to compact reference cavities to realize chip-scale, spectrally pure optical sources [18]–[27].

This body of work demonstrates several of such sources and their use in high performance optical phase synchronization over fiber links. By first realizing spectrally pure lasers at the chip-scale, high performance optical phase synchronization can be achieved using only simple, low power feedback loops. First, the cavity-stabilized stimulated Brillouin scattering (CS-SBS) laser with ~1 Hz fundamental linewidth (FLW), ~30 Hz integral linewidth (ILW), and Allan deviation of fractional frequency instability (ADEV FFI) better than $2x10^{-13}$ at 50 ms, using chip-scale technologies is presented. Next described is a fiber-connected pair of these stabilized lasers as a transmitter and receiver for high performance optical phase synchronization. This realizes the optical-frequency-stabilized phase locked loop (OFS-PLL), achieving an ultra-low residual phase error variance of $3x10^{-4}$ rad^2 optical phase synchronization using only low power, low bandwidth (<1 MHz) feedback loops [6], [7]. Finally, this approach is demonstrated in a FREquency Stabilized Coherent Optical (FRESCO) link [28]–[30] as a step toward DSP-free performance that offers promise for bringing spectrally efficient, high-order QAM links to tomorrow's greener data center interconnect.

1.2 Structure of thesis and contributions

The structure of this dissertation and contributors to each chapter are as follows, and further listed below: Professor Daniel J. Blumenthal (D.J.B) was the thesis and research advisor for the full body of work presented. Professor John E. Bowers (J.E.B), Professor Scott. B. Papp (S.B.P.), and Professor Luke Theogarajan (L.T.) served as thesis committee members and supported the results with helpful discussion, guidance in realizing these complex experiments, and contributions of key photonic devices.

Chapter 2 discusses the background content and state-of-art necessary for presenting this work in proper context. Current approaches to optical phase recovery for coherent communications are discussed and state-of-art approaches in realizing narrow linewidth laser sources are reviewed.

Chapter 3 presents the techniques used for characterizing frequency noise, linewidths, and stability of the high spectral purity sources investigated in this work. These systems were realized in simple laboratory setups using readily accessible optical and electrical components.

Contributors: G.M.B. constructed and characterized each noise measurement system. M.W. Harrington (M.W.H.) and A. Isichenko (A.I.) assisted with construction of experiments and measurement automation for characterizing laser noise. S.B.P assisted greatly with the design and approach for measuring close-to-carrier noise and stability of heterodyned laser sources.

Chapter 4 presents the cavity-stabilized stimulated Brillouin scattering (CS-SBS) laser, with brief discussion on SBS-based linewidth narrowing and chip-scale reference cavity

stabilization. Includes measurements of frequency noise, stability (<$2x10^{-13}$ at 50 ms), and linewidths (~ 1 Hz fundamental linewidth and ~ 30 Hz integral linewidths) using the approaches presented in Chapter 3.

Contributors: D.J.B., P. A. Morton (P.A.M.), and S.B.P oversaw design and construction of linewidth narrowing approaches and system level considerations. P.A.M. contributed the extended cavity narrow linewidth pump laser sources [31], and D. Huang (D.H. et. al., [32]) contributed the heterogeneously integrated pump laser for the experiments in [33] that were assisted by S. Liu. D. Bose (D.B.). fabricated the SBS laser resonator (with additional contributions given in [34]). W. Zhang (W.Z.) and L. Stern (L.S.) designed, fabricated, and supplied the chip-scale >1 Billion Q reference cavity [18] with oversight by S.B.P. G.M.B. designed, constructed, and characterized the stable SBS laser systems, including laser frequency noise and stability measurements. M.W.H and A.I. assisted with system construction and frequency noise measurements and characterization. J. H. Dallyn (J.H.D.) and Professor R. O. Behunin (R.O.B.) contributed greatly with detailed modeling of cavity stabilization and noise dynamics of SBS lasing, thereby supporting experimental results.

Chapter 5 presents two stable lasers connected over fiber to realize the optical-frequency-stabilized phase locked loop (OFS-PLL). The spectral purity and stability achieved by the stable SBS lasers enable phase synchronization performance with residual phase error ~$3x10^{-4}$ rad^2 using only low bandwidth feedback loops.

Contributors: D.J.B and S.B.P supported design of the phase synchronization approach using spectrally pure lasers. L.T. contributed to design considerations and experimental realizations of optical phase locking using low power electronics. G.M.B. developed,

constructed, and characterized the experimental setups. M.W.H supported experiments and measurements, and A.I. additionally supported experiments with lab-automated infrastructure. K. Liu (K.L.) contributed with discussion on models of closed loop noise dynamics.

Chapter 6 demonstrates high performance optical phase synchronization operating in a high order QAM coherent link, achieving 256-QAM at 10 GBd and 64-QAM at 56 GBd. This has been termed the FREquency Stabilized Coherent Optical (FRESCO) link [28]–[30]

Contributors: D.J.B. devised and supported the FRESCO approach. G.M.B. constructed and optimized the coherent link testbed, and developed and characterized the FRESCO system. M.W.H. assisted greatly with experimental realization of the FRESCO systems. A. M. Netherton (A.M.N.) assisted with initial demonstrations of the FRESCO link [30].

Chapter 7 summarizes the key results of this thesis and discusses promising future directions for this technology and approach to compact, spectrally pure sources for tomorrow's low energy optical phase synchronization architectures.

2 Background and state-of-art

2.1 Optical phase synchronization over fiber links

This chapter presents background information on optical phase synchronization over fiber links. Particular focus is given to the discussion of employing spectrally pure, stabilized lasers as local and remote sources with each laser independently exhibiting high coherence. When connected over fiber, the two sources are able to interoperate with high *mutual coherence*, or an optical phase relationship that is well-behaved and evolves in a predictable manner over time, as presented in Figure 2.1. This approach allows high performance optical phase synchronization with simplified, low power electronics.

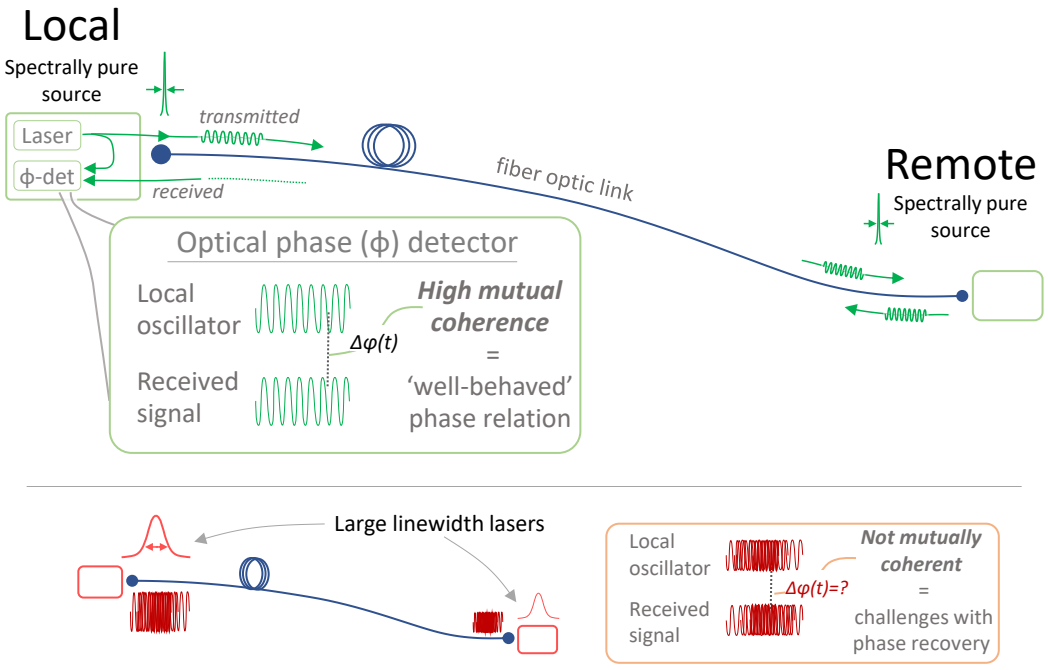

Figure 2.1. Two lasers connected over a fiber optic link for optical phase comparison and synchronization. When using two lasers that each independently exhibit high spectral purity and stability, the pair of sources are able to operate together with high mutual coherence, i.e., the optical phase relation between the two sources is well-behaved and evolves in a predictable manner. This mutually coherent performance simplifies and enables precision optical phase synchronization.

This method of employing compact, mutually coherent sources contrasts standard approaches [35]–[44] to optical phase synchronization that use high bandwidth, electrical and optical phase locked loops (E/OPLLs) to correct for the larger phase noise inherent to larger linewidth commercial semiconductor lasers. These phase lock architectures are discussed and compared in terms of phase lock performance, power consumption, and compatibility with high order modulation formats.

Next, narrow linewidth lasers that have been developed in recent years are reviewed. Approaches for linewidth narrowing and laser stabilization that are common in time and frequency standards experiments are discussed. These techniques and key results are compared in terms of performance, complexity, and system size. Particular focus is given to research efforts toward compact, chip-scale, and waveguide based technologies.

Optical phase locked loops

An optical phase locked loop is realized by comparing the phase error between two optical sources and actively tuning the optical phase of one laser to match the phase of the other [35]–[44]. A simplified diagram of an OPLL is shown in Figure 2.2.

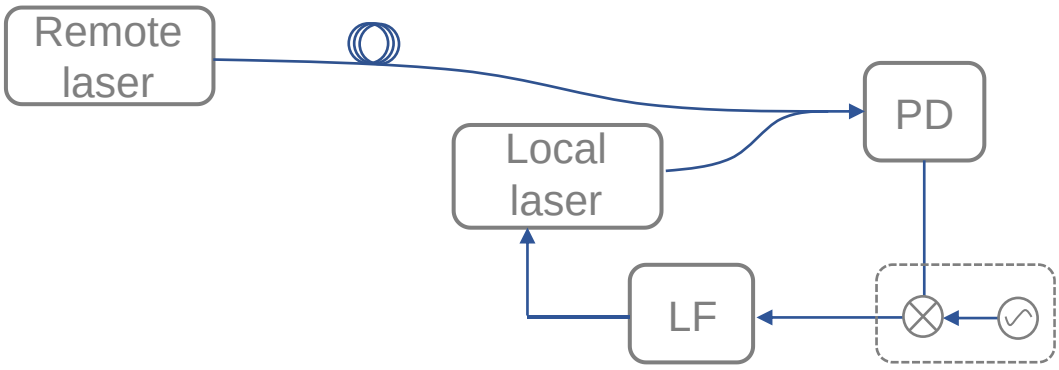

Figure 2.2. Diagram of an optical phase locked loop. Two lasers are optically mixed onto a photodiode to generate a phase error signal. For a homodyne loop, (lasers are phase locked at the same carrier frequency) the error signal is directly processed by the loop filter (LF). For a heterodyne phase lock, a frequency synthesizer is electrically mixed with the error signal (dotted subsystem)

Under closed loop operation, a key metric for characterizing loop performance is the residual phase error, typically reported by the power spectral density (PSD) of phase error or as the residual phase error variance, σ_ϕ^2 in units of [rad^2]. Minimizing the residual phase error corresponds to better performance, by attaining a tighter tracking of the optical phases between the two lasers. With finite loop gain and loop bandwidth [42] that limits the amount of phase correction an OPLL can support, it follows that another approach to minimize the residual phase error could be two employ lasers with lower phase noise, or equivalently, *lower linewidths*. This can be appreciated by a simple relation between reference and LO laser fundamental linewidths, loop bandwidth, and residual phase error variance developed in analyses of OPLLs shown in Eq. 2.1

$$\sigma_\phi^2 = \frac{(\delta\nu_{tot})}{B} \qquad 2.1$$

where B is the feedback loop noise bandwidth and $\delta\nu_{tot}$ is the sum of the reference and local oscillator fundamental linewidths [44]. When using standard commercial lasers with linewidths of several MHz, the loop bandwidths required for practical phase locking can exceed hundreds of MHz [36], placing strain on integration approaches and demanding high speed electronics that consume several Watts. Herein lies the central theme of the work presented in this thesis: by first making efforts to reduce the independent linewidths of the lasers employed in an optical phase lock, the residual phase error can be greatly decreased while using only low bandwidth feedback and low power electronics. Chapter 5 explores this approach and demonstrates high performance phase synchronization realized at the chip-scale by employing compact, spectrally pure lasers. In an application demonstration of a high capacity optical coherent communications link, the impact of low residual phase error

is shown to enable transmission formats with increased spectral efficiency as discussed in Chapter 6.

2.2 Laser noise and stability

Substantial efforts have been invested over recent decades to develop optical sources with exceptional spectral purity and long term stability. These systems typically find use in precision metrology experiments, such as for distribution of frequency references [5]–[9], research in physical constants [10]–[13], and for comparing atomic clocks [4], [14], [15], [45], [46] such as those used for geodesy [16], [17] and tests of fundamental physical laws [12]. To realize sources with such spectral purity and stability, one common approach is to stabilize a narrow linewidth laser to an ultra-high-quality factor (Q) optical reference cavity in a Pound-Drever-Hall [1], [47] feedback loop. In a well-designed system, the stability of the laser is then determined by the stability of the reference cavity. As such, great care is taken to realize optical reference cavities with extreme insensitivity to frequency noise sources and thermal drift, which often requires table scale systems. These efforts result in lasers with extremely stable average frequency, though not necessarily ultra-narrow fundamental linewidths[1]. Porting these cavities to the chip-scale with a tolerable performance trade-off can broaden the use of this approach to new and varied commercial-scale applications. Further, combining reference cavity stabilization with narrow fundamental linewidth lasers [21], [23], [25], [26] can realize optical sources with low noise across all offset frequencies – a true spectrally pure source.

[1] the importance of these considerations is application dependent, e.g., narrow fundamental linewidths in communications can be more important than stable average frequency as will be discussed in Chapter 6

Characterizing laser noise

Frequency and phase noise of lasers are commonly characterized by power spectral densities (PSD) of frequency fluctuations, $S_f(f)$ [Hz^2/Hz], and/or of phase fluctuations, $S_\phi(f)$ [rad^2/Hz] where f is the Fourier frequency offset from carrier [48]. In these representations, common noise phenomena have identifiable slopes that can be described by power laws as functions of offset frequency, f, given by a general form for $S_f(f)$ in Eq. 2.2,

$$S_f(f) = \sum_\alpha h_\alpha f^\alpha \qquad 2.2$$

where h_α is the intensity coefficient for the noise process with power law exponent α. We note that phase, being the time integral of frequency, is related to the frequency representations by $1/f^2$ (power law exponent, $\beta = \alpha - 2$). Sample power spectral densities with power law noises are shown in Figure 2.3 and summarized for various noise terms in Table 2.1.

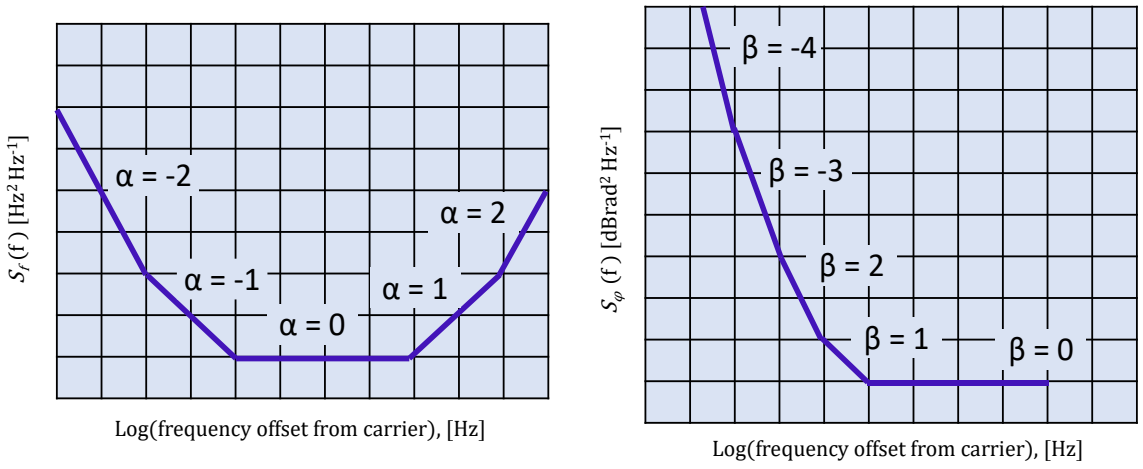

Figure 2.3. Frequency and phase noise power spectral densities with representative power law noises

To characterize laser stability, the Allan variance (AVAR) of fractional frequency instability (FFI) is commonly used, defined by Eq. 2.3 below [48], [49]

$$\sigma_\tau^2(\tau) = \frac{1}{2(M-1)} \sum_{i=1}^{M-1} [y_{i+1} - y_i]^2 \qquad 2.3$$

where τ is a measurement observation interval in seconds. Extensive additional information and analyses are given in seminal Refs. [48]–[50].

In the results presented in this work, a modified form is used, termed the overlapping Allan deviation, and will be referred to as ADEV throughout the text[2]. The use of overlapping samples rather than consecutive / stepped sampling improves confidence of stability estimates at the cost of greater computational complexity [48]. A plot of power law noises in ADEV is shown in Figure 2.4 and a table relating frequency and phase noise power spectral densities and ADEV is shown in Table 2.1.

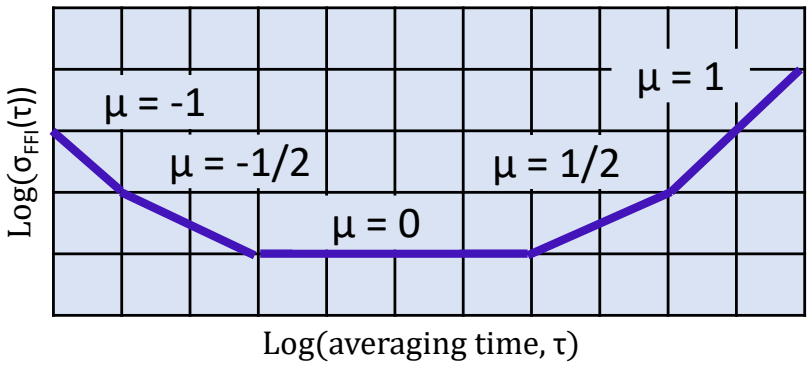

Figure 2.4. Allan deviation and power law noise slopes, for use in tandem with Table 2.1 to relate frequency / phase noise power spectral densities and ADEV power law noise slopes.

[2] Measuring 'sigma' as a function of 'tau' results in these plots sometimes being referred to in literature as 'sigma-tau' plots

Table 2.1. Summary of power laws noises and their slopes in frequency and phase noise power spectra, and in Allan deviation, (frequency modulation FM, phase modulation PM). Lasers typically exhibit random walk FM and flicker FM at lower Fourier offsets, and white FM at high offsets

Noise process	$S_f(f) = h_\alpha f^\alpha$	$S_\phi(f) = h_\beta f^\beta$	$\sigma_{FFI}(\tau)$
	α =	β =	μ =
Random walk FM	-2	-4	1/2
Flicker FM	-1	-3	0
White FM	0	-2	-1/2
Flicker PM	1	-1	-1
White PM	2	0	-3/2

For a white-frequency-noise-only laser with frequency fluctuations governed by quantum phase noise processes [51]–[53], the power spectral density of frequency fluctuations will display a flat noise (slope $\alpha = 0$) at all offset frequencies with corresponding noise coefficient h_0. This type of noise gives rise to a pure Lorentzian lineshape with width $\pi \cdot h_0$ (with units of h_0 in [Hz^2/Hz]). This particularly important concept of a quantum-limited linewidth is commonly referred to interchangeably in literature as the fundamental linewidth, Lorentzian linewidth, and instantaneous linewidth. Due to the identifiable shape of white noise in the frequency noise PSD, a common method for estimation of this linewidth is to extract the value of white frequency noise at high frequency offsets (where environmental and technical noise do not dominate) and scale by π [54], [55]. This is the method employed in this work, and this lineshape will be referred to as the *fundamental linewidth* (FLW) throughout the text.

In practice, however, a laser will suffer from additional noise due to environmental and technical sources and therefore will have a broadened lineshape that is no longer a pure Lorentzian. This linewidth is commonly referred to interchangeably in literature as the

effective linewidth, total linewidth, and integral linewidth. Due to the presence of these higher order noise terms, the lineshape, and therefore linewidth, is dependent on the observation time of the measurement. Care must therefore be taken when evaluating results that simply report a laser 'linewidth' and no explicit definition, or qualifier of measurement approach and observation timescales. Further, calculation of a lineshape from a noise spectrum must be numerically evaluated [54]. Nonetheless, effective methods have been developed to calculate integral linewidths, such as the *β-separation method* [54] and *integration of phase noise* approaches [6], [23], [56]. In this work, the term used to describe this broadened lineshape will be the *integral linewidth* (ILW) and is calculated using both of the previously described methods. Further detail is given in Chapter 3.

In Figure 2.5 below, a sample curve of power spectral density of frequency fluctuations and Allan deviation fractional frequency instability are shown and identify laser noise signatures as they manifest in lineshape behavior.

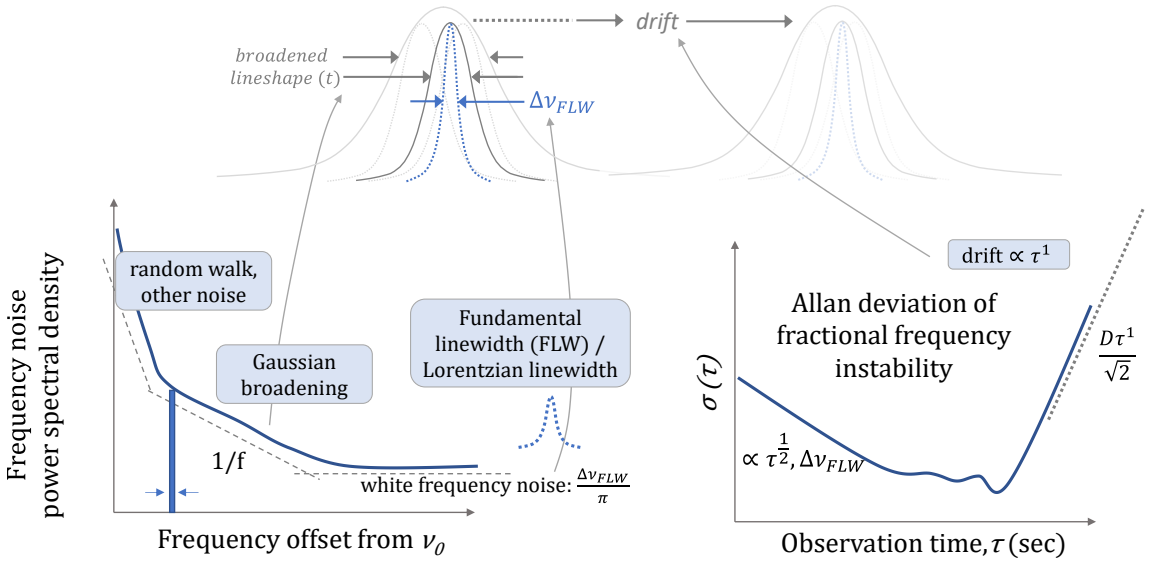

Figure 2.5. Sample laser lineshape and power spectral density of frequency fluctuations (in units of Hz^2Hz^{-1}), and Allan deviation of fractional frequency instability. White frequency noise gives rise to Lorentzian or fundamental linewidth, $\Delta\nu_{FLW}$. Flicker frequency noise, or 1/f noise, leads to Gaussian broadening of laser lineshape that is a function of observation time [54]. Other noise terms lead to lineshape jitter and instability and drift of lineshape over time. These longer timescale effects are often presented in ADEV, and e.g., drift is linear vs. observation time τ. Though not commonly plotted for short timescales, high frequency offset noise can still be readily identified in ADEV, such as white frequency noise (laser FLW) with ADEV slope of $\tau^{-1/2}$.

Reference cavities for stability and narrow integral linewidth

The best performing cavity-stabilized lasers are typically realized using ultra-high-Q optical reference cavities that are rendered insensitive to external noise sources, often by housing such devices in vacuum enclosed environmental isolation systems [2], [3]. These approaches are capable of supporting laser integral linewidths below 10 mHz with carrier instabilities of 4×10^{-17} at timescales between 1 and 10 seconds [3]. In smaller form factors, chip-scale stabilized lasers have been realized by locking semiconductor or stimulated Brillouin scattering lasers to whispering gallery mode resonators [21]–[24], photonic integrated waveguide spirals [20], [27], [57], thermally engineered waveguide resonators [58], [59], and compact Fabry-Perot resonators [18]. With a trade-off in stability due to

their compact size and lack of sophisticated environmental isolation chambers, these technologies are still capable of impressively low frequency instability on the order of ~$1x10^{-13}$ at timescales between 1 ms and 100s of ms. These cavities are compared in terms of reported integral linewidths and system size in Figure 2.6.

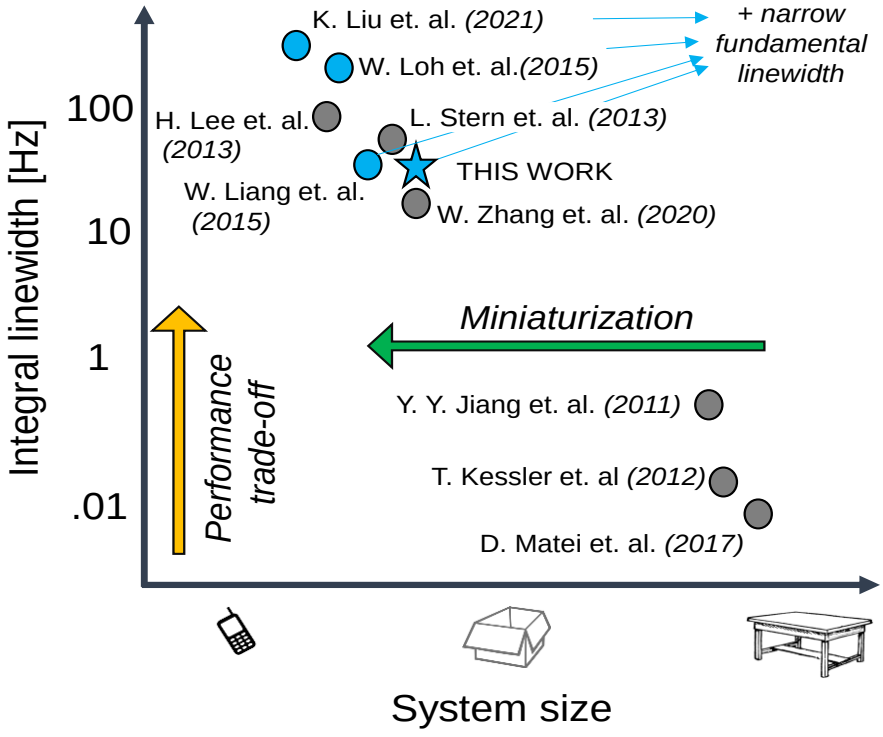

Figure 2.6. Comparison of stable laser reference cavity systems in terms of total system size (est., cm^3) and reported integral linewidths. Selected works are Refs. [2]–[4], [18]–[20], [22], [23], [26], [60]. It is noted that several of these systems (blue) also demonstrate narrow fundamental linewidths [22], [23], [26], [60], though are not explicitly reported in this comparison of stability and integral linewidths as determined by reference cavity performance.

Narrow fundamental linewidth, compact lasers

In combination with cavity stability, a spectrally pure source will have a narrow fundamental linewidth and correspondingly low phase noise at high offset frequencies. Development of narrow fundamental linewidth sources has seen great strides in especially

recent years. Sub-Hz fundamental linewidth lasers have been demonstrated in waveguide platforms that are amenable to CMOS foundry fabrication, by leveraging stimulated Brillouin scattering physics [55] and recently, self-injection locking distributed feedback (DFB) lasers to high-Q spiral waveguide resonators [27], [57]. Wafer scale heterogeneously integrated Si/III-V lasers have demonstrated sub kHz fundamental linewidths [32], [61]. Commercialized ultra-narrow linewidth lasers can readily achieve fundamental linewidths on the order of tens-of-Hz with significant output powers approaching 200 mW [31].

2.3 Spectral purity and optical phase synchronization

Combining the stability and improved close-to-carrier noise achieved by reference cavity stabilization with the low phase noise afforded by ultra-narrow fundamental linewidths can realize optical sources with low noise at all carrier offset frequencies [21], [26], [60]. Connecting two of these sources over fiber optic links can then enable high performance carrier phase synchronization using only low bandwidth loops by relaxing the demands of the phase lock bandwidth and electronics. An illustration describing the two stage approach to linewidth narrowing and cavity stabilization and its impact on phase lock demand is shown in Figure 2.7.

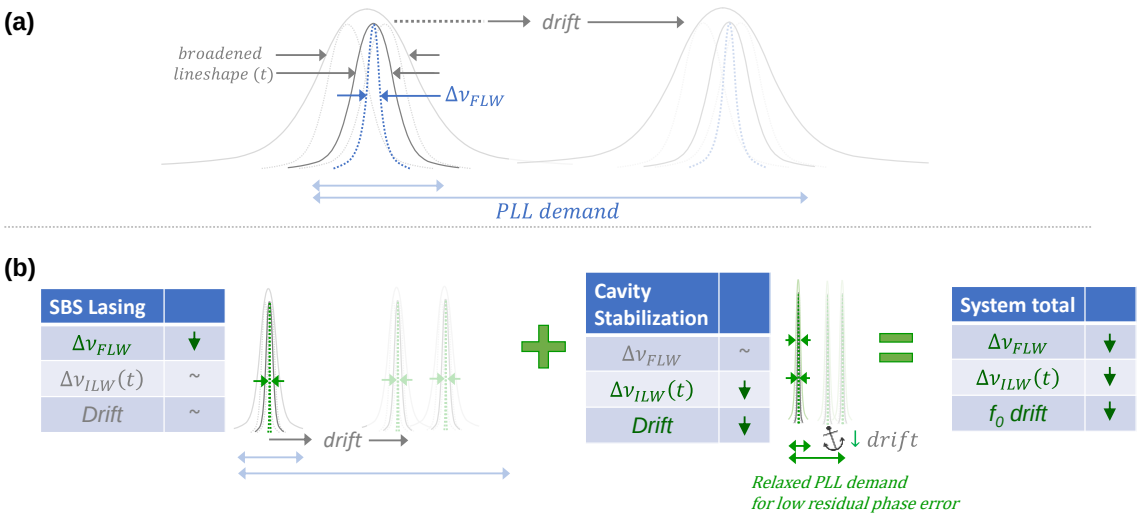

Figure 2.7. Illustrative comparison of a free running laser (a) with fundamental linewidth $\Delta\nu_{flw}$ and integral linewidth, $\Delta\nu_{ILW}(t)$, that is a function of observation time. Lineshape drifts linearly with time. A phase locked loop must act to correct for phase error, determined by phase noise of the laser sources. The loop must have sufficiently high bandwidth to compensate high frequency fluctuations, i.e., phase noise determined by $\Delta\nu_{flw}$ as well as a large enough dynamic range to maintain lock over lineshape drift. (b) By reducing $\Delta\nu_{flw}$ via SBS lasing and reducing $\Delta\nu_{ILW}(t)$ and drift by cavity stabilization, the demands for a phase lock are greatly reduced.

An approach that realizes this performance, shown in Figure 2.8, is the chip-scale, optically synchronized link where a spectrally pure source is used for the transmit and receive lasers at the fiber link end points. The high mutual coherence between transmit and receiver stable SBS lasers results in ultra-low residual phase error and improved phase lock capture- and hold-in range over a non-stabilized link. Further, the linewidth reduction properties of the SBS laser reduce the mutual phase noise at frequency offsets outside the bandwidth of the final optical phase lock, offering a performance improvement over OPLLs realized with large linewidth lasers that require high bandwidth electronics. This high performance phase synchronization system is used to enable an ultra-high capacity, high spectral efficiency coherent link.

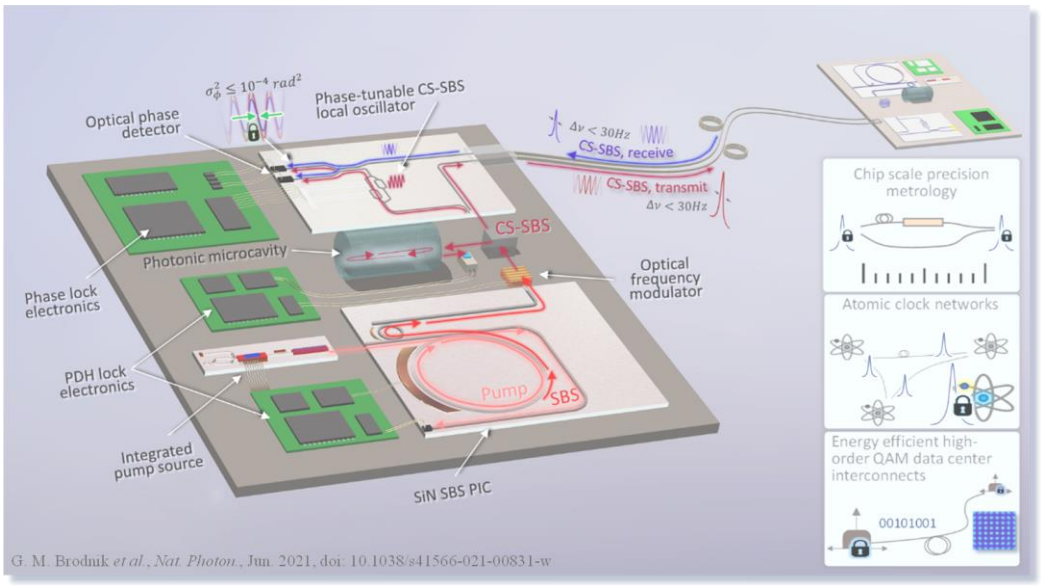

Figure 2.8. A precision optical-phase synchronized fiber link can be realized with independent cavity stabilized SBS lasers. SBS lasing is performed using an ultra-low-optical-loss SiN photonic integrated circuit (PIC) [55] for first-stage phase noise reduction of the fundamental linewidth to <1 Hz. Carrier stabilization is implemented with low-bandwidth sub-megahertz PDH feedback loops and locking to a compact reference cavity with quality factor (Q) of one billion [18]. The stable SBS laser sources provide spectrally pure carriers for a low-bandwidth optical-frequency-stabilized phase locked loop. This type of compact, carrier-stable link can enable applications in precision metrology, distributed atomic timekeeping and high-capacity coherent fiber-optic communications [60].

3 Characterizing laser noise and stability

As new technologies enable practical realizations of optical sources with ultra-high spectral purity [27] and stability, accessible techniques [61]–[64] are required in laboratory settings to characterize such exquisite sources. This chapter discusses several of such techniques used to measure frequency noise and carrier stability that are used here to characterize the narrow linewidth lasers developed throughout this thesis. Broadly speaking, the measurements fall into class of techniques called 'frequency discrimination,' i.e., converting fluctuations in an oscillator's frequency to fluctuations in a measurable electrical signal that can be sampled and processed offline.

In the optical domain, direct frequency discrimination of the laser at carrier frequencies of ~193 THz was achieved using a fiber-based asymmetric Mach-Zehnder interferometer (aMZI) as a fringe side optical frequency discriminator (OFD) [60], [63], [65]. Additional details of this technique are provided in the Section 3.1. This measurement, directly made on a single optical carrier, is suitable for high offset frequencies from carrier. However, environmental noise in the fiber delay of the asymmetric MZI dominates at carrier offsets below ~1 kHz, thus requiring a second technique to characterize frequency noise and stability at offsets closer to carrier (<1 kHz). The OFD method combined with a suitable second method for measuring these lower frequency offsets can yield the full power spectral density of frequency fluctuations from several Hz carrier offset to several tens of MHz offsets, providing a both broad and detailed view of laser frequency noise.

A suitable second method that targeted these close in frequency offsets optically heterodyned two lasers and used an electrical frequency discriminator (EFD) [60], [62] to convert fluctuations of the intermediate frequency (IF) beat note signal to voltage

fluctuations. The IF frequency fluctuations were processed offline in a similar manner to the OFD. This EFD technique yields the combined noise dynamics of each of the lasers that are optically mixed. If the frequency noise of each of the heterodyned lasers are similar, the independent noise contributions of each source cannot be uniquely identified. This mutual noise is a particularly important measurement of interest for this work – for an optical phase lock, lasers are optically mixed for phase discrimination in a phase locked loop [35], and their mutual noise is key in setting demands for loop design and governing phase lock performance [37]. If desired, independent laser noise *can* be uniquely measured using the EFD approach by heterodyning the laser under test with an ultra-stable reference laser (with superior frequency noise and stability), which yields combined noise dynamics that are determined primarily by the laser under test. The EFD technique applied in both of these measurement regimes is discussed in more detail in Section 3.2 and key results are presented in Chapter 4.

Long term stability and drift are characterized by the commonly employed Allan deviation (ADEV) [48]–[50], [66]. For these measurements, the time domain frequency fluctuations as measured by the EFD method were processed offline for overlapping ADEV of fractional frequency instability (FFI) and are discussed in more detail in Section 3.3 with key results reported in Chapters 4 and 5.

These methods for characterizing frequency and phase noise power spectra and ADEV FFI provide the most complete description of a laser's frequency dynamics. However, it is often convenient and appropriate to extract key parameters that capture certain aspects of oscillator behavior from these measurements to enable simple comparisons between sources. Throughout this work, key parameters used to describe these optical sources are the

fundamental linewidth (FLW) [54], [67], integral linewidth (ILW) [6], [23], [54], and ADEV [48]–[50], [66] of the fractional frequency instability (FFI) observed at various timescales. Fundamental linewidths were calculated by extracting the white noise floor of the frequency noise PSD (in units of Hz^2/Hz) at high carrier offsets and scaling by π [54]. Integral linewidths were calculated using two methods: the *β-separation* method [54] and an *integration of phase noise* method [6], which are discussed in more detail in Section 3.4.

3.1 Optical frequency discrimination

Frequency noise (FN) power spectral densities, $S_\nu(f)$ in units of Hz^2Hz^{-1}, of the optical sources were measured using frequency discrimination techniques for carrier offset frequencies ranging from 1 Hz to 10 MHz. At high frequency offsets of 10 MHz down to 10 kHz, FN was measured with an optical frequency discriminator [63], [65] (OFD) in the form of a fiber optic asymmetric Mach-Zehnder interferometer (aMZI), shown in Figure 3.1

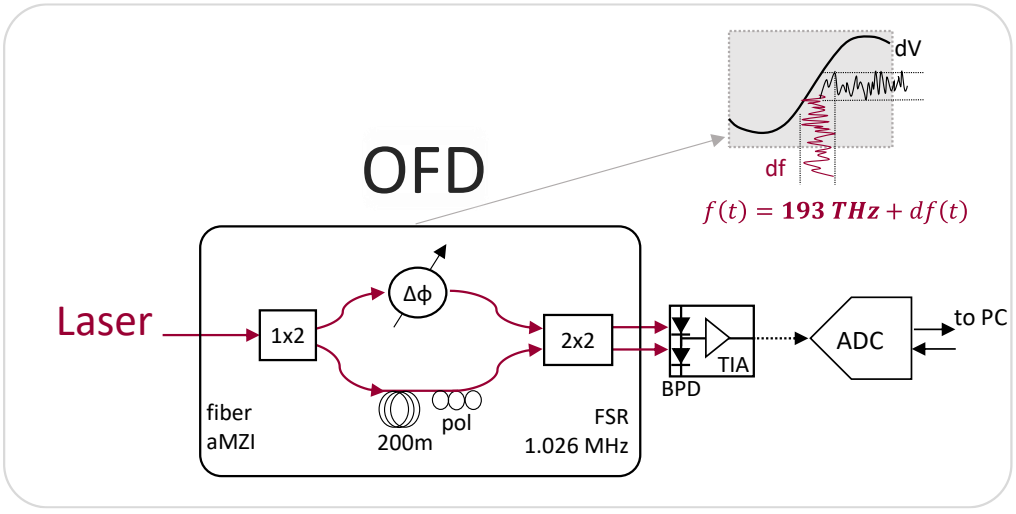

Figure 3.1: Optical frequency discriminator (OFD) for measuring frequency noise directly on an optical carrier. Asymmetric Mach-Zehnder interferometer (aMZI), polarization controller (pol), free spectral range (FSR), balanced photodiode (BPD), transimpedance amplifier (TIA), analog-to-digital convertor (ADC), personal computer (PC)

The aMZI incorporates a 3 dB optical splitter to form two independent optical paths, one consisting of a 200 m optical fiber delay line and polarization controller and the other with a voltage-controlled fiber phase shifter. This 200 m delay line corresponds to a free spectral range (FSR) of 1.026 MHz. OFD measurements were made directly with optical carriers as input, with the fiber phase shifter providing slow (~ 1 Hz) adjustments to the relative phase of the optical paths to achieve quadrature biasing of the aMZI. An output 2-by-2 combiner photo-mixed the optical signal on a Thorlabs PDB450C balanced photodetector (BPD). Optical frequency fluctuations of the laser under test were converted into analog voltage fluctuations and sampled by an analog-to-digital converter (ADC) and processed offline for spectral characterization. The ADC sampling was performed using a Keysight DSOX1204G digital storage oscilloscope triggered when the optical carrier is at quadrature of the aMZI transfer function. With known peak-to-peak voltage fluctuations, V_{pp}, and aMZI optical time delay, τ_d, the voltage PSD, $S_V(f)$ in V^2Hz^{-1} were converted to frequency noise, $S_\nu(f)$ in units of Hz^2Hz^{-1} as a function of carrier offset frequency, f, by (Eq. 3.1) [55], [61], [63], [65]

$$S_\nu(f) \;=\; S_V(f)\left[\frac{f}{sin(\pi f \tau_D)\; V_{pp}}\right]^2 \qquad 3.1$$

This conversion between the voltage PSD to the frequency noise PSD results in artificial spurs at integer multiples of the aMZI FSR due to the $sin(\cdot)$ term in the denominator, which can be filtered offline using a median filter in the data processing step.

Limitations of the OFD

Frequency noise measurements using this standard OFD approach can be limited in several ways. At close to carrier offsets (< ~1 kHz), acoustic noise in the fiber delay line and

fiber patch cables of the aMZI can dominate the measured power spectra, masking true laser noise that falls below this level. This is especially restrictive for measuring the cavity stabilized lasers developed in this work, where the close-to-carrier noise is low (<1x10^2 Hz^{2}Hz^{-1}). An example of OFD based fiber noise dominating a laser FN measurement is shown in Figure 3.2 below.

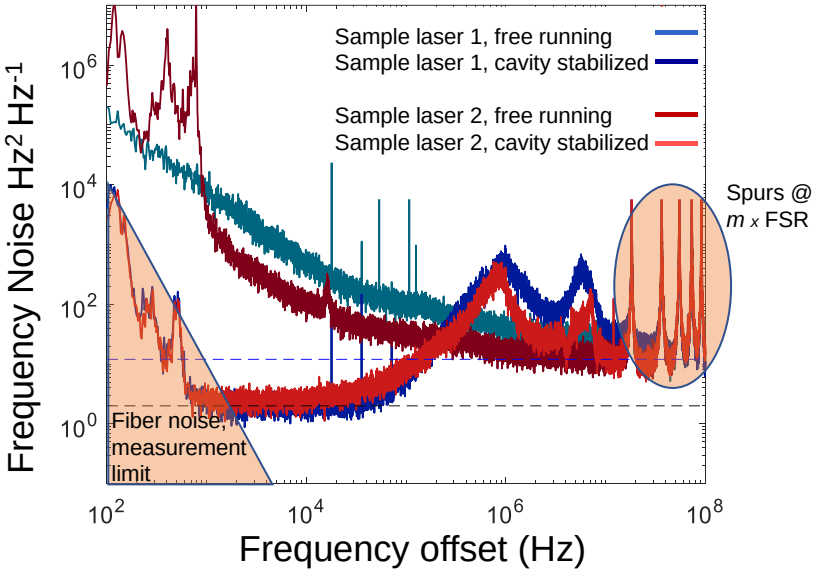

Figure 3.2. Examples of OFD based frequency noise measurements of two different external cavity lasers (ECLs). During free running operation the OFD is able to accurately measure frequency noise down to 100 Hz offset. When each laser is stabilized to a reference cavity, the OFD cannot accurately measure frequency noise at carrier offsets below ~ 1 kHz due to fiber noise in the aMZI dominating the measured FN. Spurs generated when inverting the aMZI transfer function are seen at integer multiples of the free spectral range (FSR).

A second potential limitation of the OFD approach can be imposed by technical or shot noise in the photodetection process, limiting the minimum noise floor that can be measured and therefore limiting the minimum fundamental linewidth extracted from the FN spectrum [27], [68]. This noise is white in the voltage power spectral density, resulting in a noise with slope that scales as f^2 in the frequency noise power spectral density. While this was not a limitation in this work, the noise floor limit can be improved by applying optical domain cross-correlation approaches as demonstrated in Ref. [27], [68].

3.2 Electrical frequency discrimination

To make close-to-carrier measurements below the OFD fiber noise limit for carrier offsets below ~1 kHz, low and intermediate offset frequency noise can be measured on the heterodyne beat note between two independent lasers [62]. Using an electrical frequency discriminator (EFD), relative frequency fluctuations in the intermediate frequency (IF) signal can be converted to a voltage signal and sampled by an ADC and processed offline in a similar manner to the OFD approach. The EFD-based system constructed for the experiments in this work is shown in Figure 3.3. Schematic for measuring mutual laser noise via optical heterodyne and electrical frequency discrimination (EFD) on the intermediate frequency (IF).Figure 3.3.

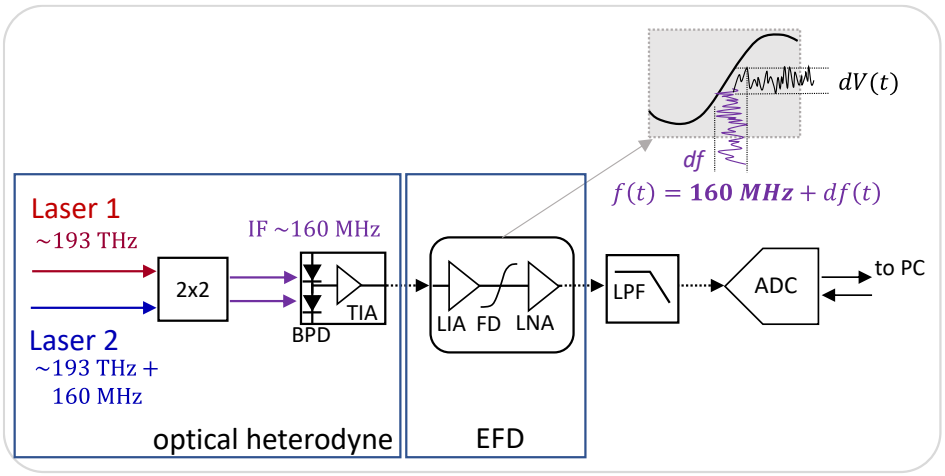

Figure 3.3. Schematic for measuring mutual laser noise via optical heterodyne and electrical frequency discrimination (EFD) on the intermediate frequency (IF). Two lasers are optically combined via a 2x2 fiber combiner. The two output ports are mixed on a balanced photodetector (BPD) with built-in transimpedance amplifier (TIA). The EFD consists of a limiting amplifier (LIA), frequency discriminator (FD) and low-noise amplifier (LNA). A low pass filter (LPF) prevents aliasing of high frequency noise into the region of interest. The voltage signal is digitally sampled by and analog to digital convertor (ADC) and processed offline.

In this system, two lasers were tuned to have a difference frequency on the order of several hundred MHz and optically combined using a 2x2 fiber combiner. The two outputs

were mixed on a balanced photodetector (BPD, Thorlabs 470C) with built-in transimpedance amplifier (TIA). The photomixing process results in an intermediate frequency in the RF domain, suitable as the input to a commercial electrical frequency discriminator module (Miteq FMDM-160). The particular EFD used in this work is based on a Foster-Seeley discriminator circuit which converts frequency fluctuations in an RF signal to a voltage signal. The input of the FMDM module has a limiting amplifier (LIA) to reduce the impact of amplitude fluctuations on the desired output that is proportional to frequency fluctuations. A low-noise amplifier (LIA) amplifies the FMDM output to voltages suitable for sampling on an ADC. The sampled voltage signal, *v[t]*, scaled by the EFD discriminator constant, *D* [Hz· V^{-1}], are the relative frequency fluctuations of the signal under test.

EFD calibration, limitations

This section discusses standard operation of an EFD based optical heterodyne measurement system, which includes calibrating the discriminator constant, measuring the linear region and zero crossing of the discriminator, and characterizing noise floor limits of the EFD approach.

Proper calibration of the EFD discriminator constant, *D* [Hz·V^{-1}], is critical for accurate measurements of frequency noise. This constant is affected by several factors: the nominal sensitivity of the electrical frequency discriminator[3] (provided by manufacturer and based on the particular RF circuit design), voltage amplifiers and filters on the output stage of the

[3] The electrical frequency discriminator used in this thesis is a Narda/Miteq FMDM-160 with nominal sensitivity of 100 mV/MHz, center frequency of 160 MHz, and approximate bandwidth of 35 MHz.

EFD, and impedance of the ADC device or instrument used for the sampling. It is therefore necessary and good practice to measure this constant before making any EFD measurement and after any change in the configuration of the electrical chain (such as insertion of electrical filters or changes in the instrument used for sampling). For the experiments in this work, the EFD discriminator constant was measured by step-sweeping an RF synthesizer (Rohde and Schwarz SMP04) across the EFD to trace out its frequency-to-voltage transfer function. The slope of the line fit to the linear region of the EFD from frequencies of ~160± 10 MHz corresponds to the discriminator constant, *D*. With the IF signal in the linear region near the center frequency of 160 MHz, the voltage output scaled by the discriminator constant is the relative frequency error of the IF signal. A sample discriminator transfer function and discriminator action are shown in Figure 3.4.

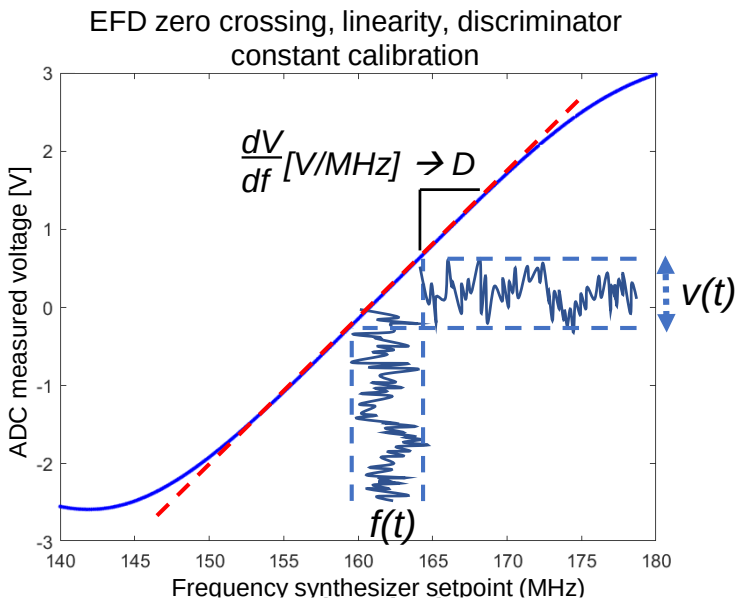

Figure 3.4. A sample calibration measurement of the electrical frequency discriminator (EFD). By step sweeping an RF frequency synthesizer across the frequency discriminator, the zero-crossing, linearity, and discriminator constant (*D*, slope of linear fit, red-dotted line) can be measured. An RF signal tuned to the zero crossing will have its frequency fluctuations, *f(t)*, converted to voltage fluctuations, *v(t)*.

For the EFD measurements in this work, calibration sweeps were fully automated and conducted before every experiment. A sample of this calibration, returning the zero-crossing frequency and discriminator constant in units of mV/MHz is shown in Figure 3.5.

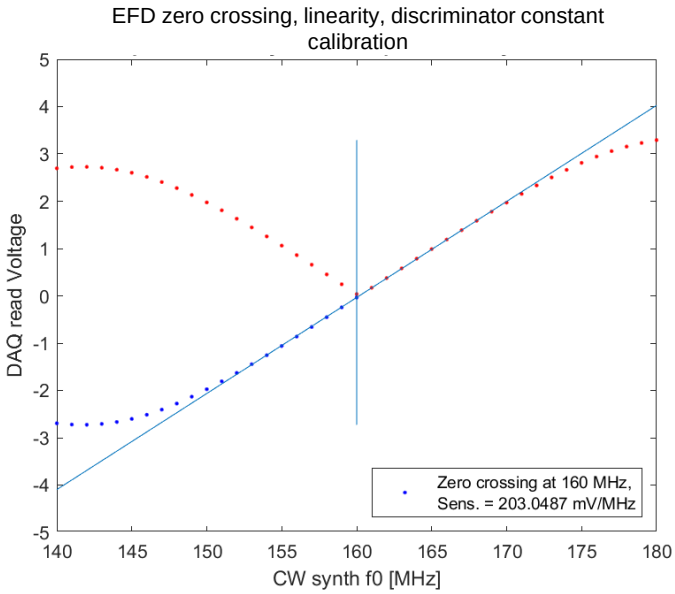

Figure 3.5. Sample output of the automated calibration of EFD discriminator constant and zero crossing by step sweeping a programmable RF synthesizer.

The noise floor of the EFD system was characterized in several stages. First, the noise floor of the ADC electrical sampling instrument (National Instruments Data Acquisition Unit, NIDAQ USB-6259) as imposed by quantization and electrical noise of the ADC was characterized. The NIDAQ USB-6259 is a 16-bit 1.25 MSa/s ADC unit with multiple voltage input and output channels. Its noise floor is dependent on the user-settable ADC range, which can be set for voltage ranges as low as ± 0.1 Volts to a maximum ± 10 Volts. The noise voltage power spectral density for each of these ADC settings was measured by recording ADC samples for a 50 Ω shunted input (zero voltage signal applied) and is shown in Figure 3.6.

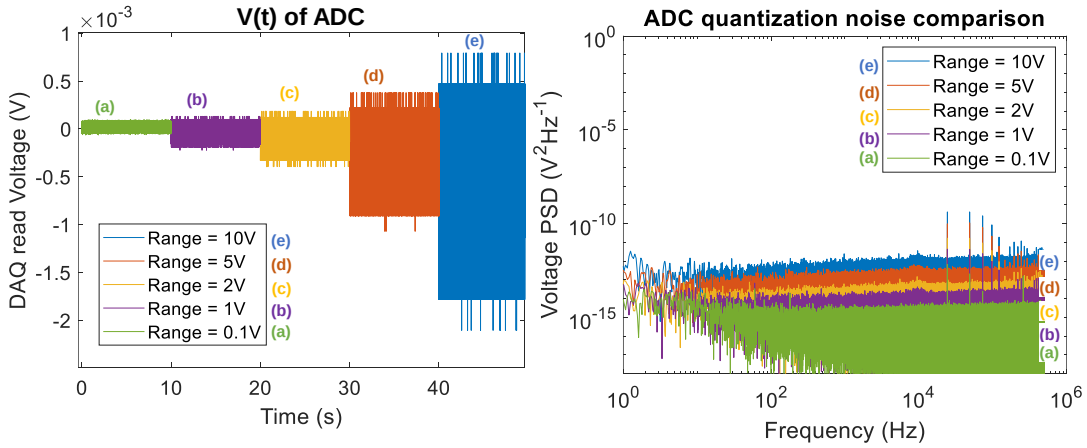

Figure 3.6. With the input to the ADC shunted with 50 Ω (zero voltage applied), samples were recorded for ADC ranges between 0.1 V and 10V (time domain, left). The voltage power spectral density (right) shows a minimum noise floor of ~1x10^{-15} V^2/Hz for the ADC range of ±0.1 V.

The minimum noise floor voltage PSD occurs for an ADC range setting of ± 0.1 V. Though using this range for EFD measurements results in the lowest ADC noise floor, it sets the most restrictive operation window for characterizing a test signal – the voltage to be sampled by the ADC in this regime must not exceed ± 0.1 V or the recorded data will reach the measurement rails. With an EFD discriminator constant of ~200 mV/MHz, this range of ± 0.1 V corresponds to a frequency range of ± 200 kHz meaning the IF signal under test must not drift out of the window 160 ± 200 kHz over the duration of the entire measurement.[4] For test signals that may drift beyond this window, a larger ADC span must be selected.

To map the minimum noise floor of the full EFD system, a simple experiment was conducted using a high spectral purity (phase noise ≪ EFD noise floor) RF frequency synthesizer as the signal under test. A CW frequency synthesizer set to 160 MHz was directly connected to the input of the EFD as shown in Figure 3.7.

[4] For optical heterodyne IF signals, this level of stability is typically only achieved for lasers that are locked to ultra-stable, environmentally isolated reference cavities.

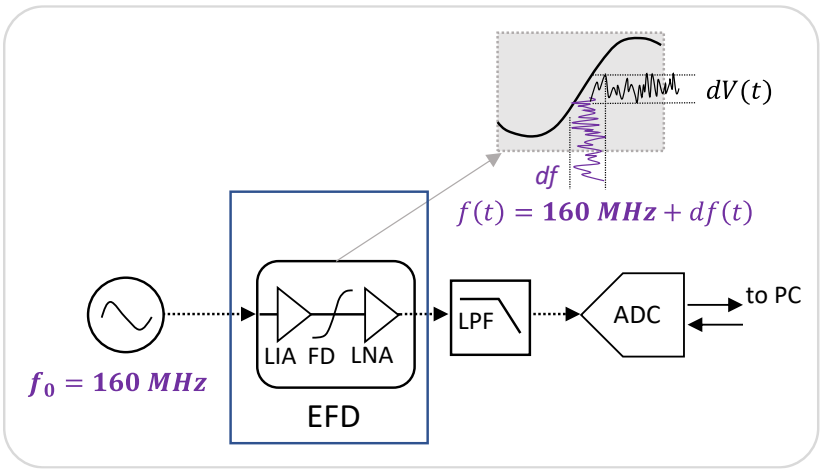

Figure 3.7. Experiment to measure the minimum frequency noise that can be characterized by the electrical frequency discriminator system. A high spectral purity CW RF synthesizer was used to generate a 160 MHz signal for the EDF input.

The frequency noise measured in this configuration corresponds to the measurement limit of the EFD system (since the true frequency noise of the RF frequency synthesizer is much lower than achievable with an EFD based measurement). This measurement of the RF source is shown in Figure 3.8.

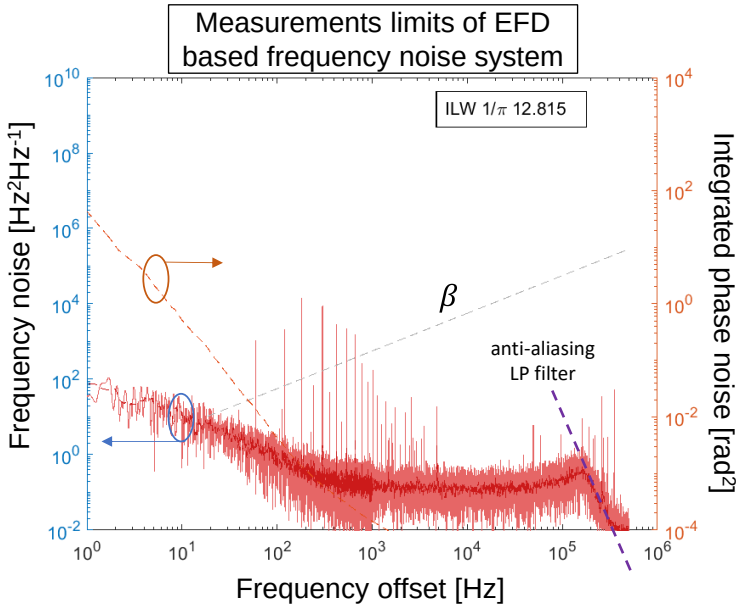

Figure 3.8. The minimum frequency noise that can be measured using the EFD system. Note the spurs at integer multiples of 60 Hz, due to power line noise in system electronics. Integrated phase noise surpasses $1/\pi$ rad^2 at a frequency offset of ~13 Hz.

Referring to Figure 3.8, the measurement limit floor of the EFD shows ~ 0.1 Hz^2/Hz white noise between ~1 kHz to ~100 kHz. The noise floor exhibits typical electronic flicker frequency noise with slope of 1/f that dominates at carrier offsets below ~1 kHz. These measurements align well with the sensitivity limits of the EFD approach reported in Ref. [9]. Power line noise spurs at integer multiples of 60 Hz are also evident, which can be removed in the data processing step.

Aliasing effects on close-to-carrier EFD measurements

When making EFD based frequency noise measurements on signals that have low close-to-carrier noise, care must be taken to ensure that high-frequency-offset noise is not aliased down to the measurement region of interest. This can occur, for example, for a measurement on the IF beat note between two lasers that are stabilized to reference cavities. In this scenario, it is possible for the stabilized lasers to have close-to-carrier (in-loop) frequency noise driven down below the level of out-of-loop noise at higher frequency offsets. The broadband noise can be aliased down to the low-frequency-offset regions measured by the EFD, resulting in an artificial measurement limit of white noise that has the same value as the far-from-carrier noise. An example of this is shown in Figure 3.9.

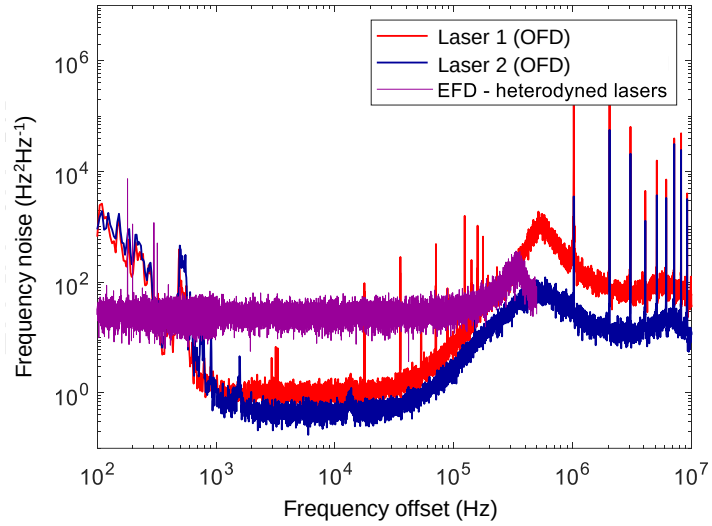

Figure 3.9. Example of high-frequency-offset noise aliased down to the low-frequency-offset measurement regions where EFD measurements are made. Independent optical frequency discriminator (OFD) measurements of FN for two lasers are shown (red, blue). Note the 'fiber noise limit' for OFD traces below 1 kHz. The heterodyne FN as measured by the EFD is expected to be the sum of the two OFD traces but shows aliased white noise (purple) at a value of ~40 Hz^2Hz^{-1}

Figure 3.9 above shows optical frequency discriminator measurements of two independent, cavity stabilized lasers with similar values of frequency noise (note the characteristic 'fiber noise limit' of the OFD approach for offsets below ~1 kHz). The EFD measurement made on the heterodyne between these two lasers is expected to match the sum of the independent FN traces. However, since the close-to-carrier noise of each laser is below their respective far-from-carrier noises (owing to cavity stabilization), high-frequency-offset noise is aliased down to the region of interest and results in an artificial white noise limit.

This issue can be overcome by adding an anti-aliasing filter after the EFD output and before the ADC sampling occurs to reject far-from-carrier noise aliasing into the region of interest. The filter designed for the system in this work was a 5th order Butterworth LC (π) filter, shown in Figure 3.10.

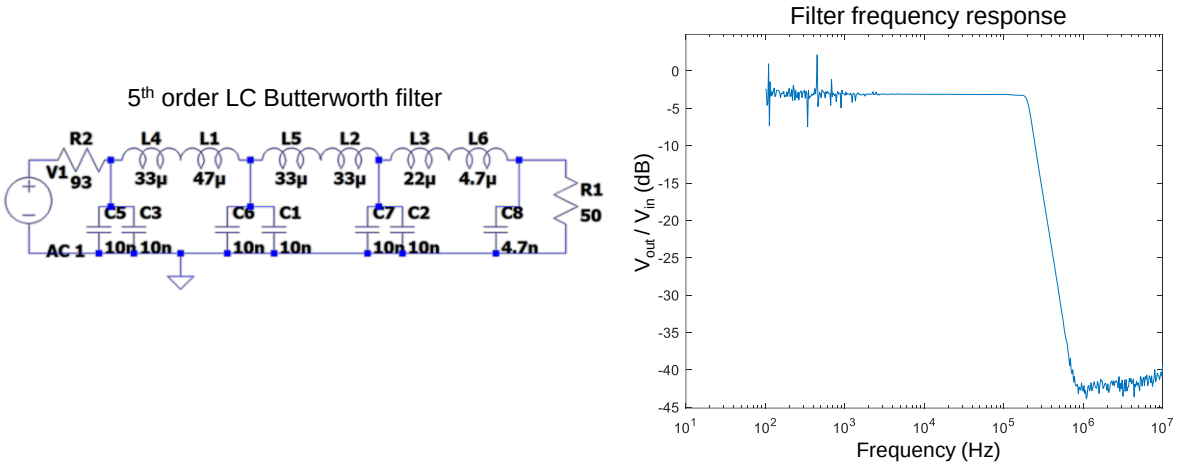

Figure 3.10. A 5th order Butterworth filter was designed as an anti-aliasing filter for the EFD system. The filter cutoff was chosen to be 200 kHz. The frequency response of the filter was measured with a step-swept frequency source showing a flat passband up to the cutoff of 200 kHz.

With the inclusion of the anti-aliasing filter, measurements of true heterodyne laser noise down to the noise floor of the EFD from frequency offsets of 1 Hz to 100 kHz were possible and reported in Chapters 4 and 5.

3.3 Laser stability and Allan deviation

Laser stability was characterized by calculating the overlapping Allan deviation ADEV of fractional frequency instability (FFI) [48] of the two-laser heterodyne IF signals as measured by the EFD system. A sample ADEV FFI measurement made on two cavity stabilized lasers is shown in Figure 3.11 and lineshape characteristics as they manifest in the ADEV are discussed.

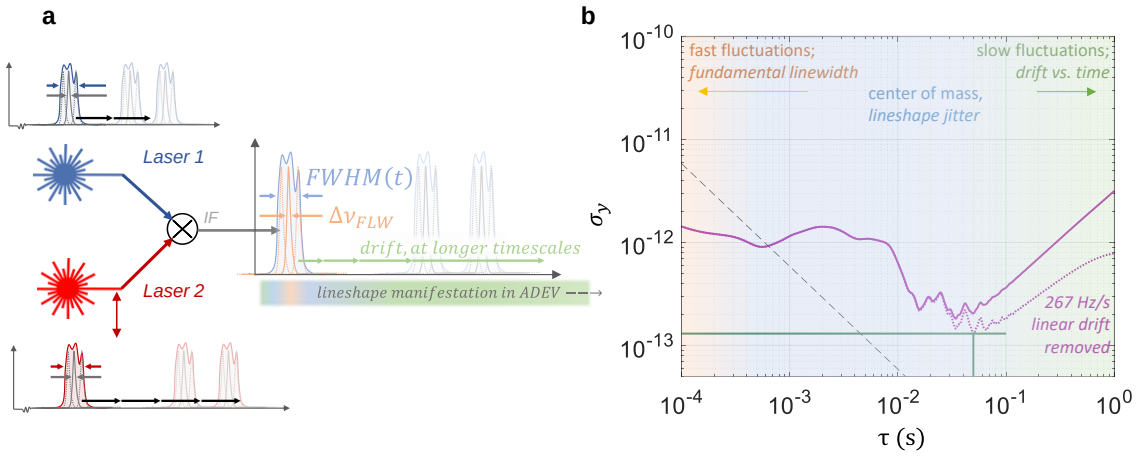

Figure 3.11. (a) Two lasers are heterodyned to generate an intermediate frequency (IF) signal to be measured by electrical frequency discriminator. The IF signal inherits the combined noise and stability of each of the independent lasers. (b) Sample ADEV plot (purple) with labeled regions governed by fast, center of mass, and slow fluctuations in the measured fractional frequency instability. A linear drift of 267 Hz/s is subtracted (purple, dotted).

Figure 3.11 illustrates that laser lineshape is a function of observation time and that lineshape characteristics manifest in the ADEV FFI as labeled in Figure 3.11b. For the sample ADEV plot shown, at short timescales, high-frequency fluctuations (as would be governed by fundamental laser Lorentzian linewidth) determine the ADEV. Shown in Figure 3.11b as the black dashed line is an ADEV trace of a signal with only white frequency noise, displaying a slope of $\tau^{-1/2}$. At intermediate timescales (100 μs to ~100 ms, or frequency fluctuations 0.1 Hz to 10 kHz), the laser lineshape is broadened from the fundamental Lorentzian linewidth to an effective, or integral linewidth (ILW) that is a function of observation time. This is shown as the light blue lineshape, labeled *FWHM(t)*, and the light blue region of the ADEV. Technical and environmental noise in each laser impact this region of the ADEV. At longer timescales (>100ms), laser drift dominates the ADEV.

3.4 Key laser noise parameters, linewidth definitions

Throughout this work, several key parameters describing laser linewidth are used to simply comparisons of lineshape between sources. Among these are the fundamental linewidth (FLW) and integral linewidth (ILW, calculated using two separate methods).

Fundamental linewidth

A laser's fundamental linewidth (also commonly called the instantaneous linewidth, Lorentzian linewidth, and/or quantum limited linewidth) gives rise to a white frequency noise power spectral density and a Lorentzian lineshape [54]. Due to this white frequency noise characteristic, a laser's fundamental linewidth can be calculated by extracting the white noise floor at high offset frequencies (where environmental and technical noise do not dominate) and scaling by π [54] to report the FLW full-width half-maximum (FWHM). The optical frequency discriminator measurements are well suited for this task, as they are capable of measurements beyond 1 MHz where laser noise is determined by this fundamental noise.

Integral linewidth

Due to environmental and technical sources, laser lineshape in practice is broadened from its FLW Lorentzian shape to an 'effective', or integral linewidth. Since the frequency noise is no longer purely white, the lineshape is no longer a pure Lorentzian and is dependent on observation time. The frequency noise power spectra and to an extent, ADEV FFI, fully capture these dynamics. However, single parameters that aim to capture important lineshape characteristics can simplify comparison between independent sources, motivating the use of multiple methods for calculating integral linewidths. Two such

methods are employed in this work: the *β-separation* approach [54] and an *integration of phase noise* approach [6], [23], [56]. The suitability of ILW calculations is application dependent, motivating the use of multiple methods in this work.

The *β-separation* method [54] identifies regions of laser frequency noise with high modulation index that contribute to lineshape broadening, rather than modulation that occurs in the wings of a laser power spectrum. The threshold that separates these two regions of frequency noise is termed the *β-separation line*, which is derived and defined in Ref. [54] and given again below by Eq. 3.2

$$\beta(f) = \frac{8\,ln(2)\cdot f}{\pi^2} \qquad 3.2$$

where *f* is the frequency offset from carrier. The area, *A*, of frequency noise, $S_\nu(f)$ in units of Hz^2Hz^{-1}, is the portion of frequency noise that contributes to lineshape broadening. This area can be calculated by Eq. 3.3 below.

$$A = \int_{f_{low}}^{\infty} H\big(S_\nu(f) - \beta(f)\big)\cdot S_\nu(f)\,df \qquad 3.3$$

Here, *H(·)* denotes the Heaviside function. The lower cutoff of the integral, f_{low}, is the minimum frequency offset for the particular measurement performed. In this work, the low frequency cutoff for measurements that later apply the *β*-separation ILW routine is typically 1 Hz, corresponding to a sample period of 1 sec. For practical laser noise, the calculation of this broadened integral linewidth will not converge[5] due to the presence of flicker and higher power law noise dominating closer-to-carrier, which is discussed in more detail in Refs.

[5] if measured to a Fourier frequency offset of 0 Hz – practical measurements have finite measurement time.

[54], [56]. After calculating the area, *A*, for a particular laser, the *full-width at half-maximum (FWHM)* is then given by Eq. 3.4 below.

$$\Delta\nu_{ILW,\beta} = FWHM = (8\ln(2)\cdot A)^{\frac{1}{2}} \tag{3.4}$$

Being a modulation index approach, ILWs calculated using this method are especially sensitive to low-frequency-offset fluctuations and laser drift. Additionally, this method is dependent on observation time, or the lower frequency bound on the integration of frequency noise. This is noteworthy because measuring lasers (and especially stabilized lasers) over longer timescales is critical for accurate reporting of their performance, though this may result in reporting a larger integral linewidth as calculated by the β-separation method. Care must be taken then when reporting or comparing results by including measurement timescales or integration ranges for integral linewidths. Further details on this method are provided in the founding material by *Domenico et al*, Ref. [54].

The second approach integrates phase noise from an offset frequency of infinity (or the highest measured frequency offset) down to the value at which the integral equals $1/\pi$ rad^2 [6], [23], [56], shown in Eq. 3.5,

$$\frac{1}{\pi}rad^2 = \int_f^\infty S_\phi(f)\,df \tag{3.5}$$

where $S_\phi(f)$ is the power spectral density of phase fluctuations in units of rad^2 Hz^{-1}, related to the power spectral density of frequency fluctuations by Eq. 3.6,

$$S_\phi(f) = \frac{S_\nu(f)}{f^2} \tag{3.6}$$

For a laser with only white frequency noise (governed by only its fundamental linewidth and no environmental or technical noise), the integral relation of Eq. 3.5 is satisfied when the lower bound on the integral is the offset frequency that corresponds to the FWHM of the laser lineshape [56]. This method can be applied to lasers with arbitrary frequency noise spectra to report the offset frequency corresponding to $1/\pi$ rad^2. It is important to note that this method, since its integration starts at the highest measured offset frequency and integrates down in Fourier frequency offset, is *unaffected by any noise that occurs below the offset frequency corresponding to the '1/π rad^2' offset*. As such, integral linewidths calucated by this method will typically be *lower than those reported by the β-separation approach* because it does not increase with increasing observation times (or, integrating over frequency ranges closer-to-carrier). Thus, in the efforts of transparency in reporting integral linewidth results, both of these methods are reported in tandem and/or explicitly identified in-line with integral linewidth results.

The high spectral purity lasers developed in this work have sufficiently narrow ILWs that EFD based measurements are required for subsequent ILW calculations. In Figure 3.1 below, the noise floor of the EFD system is again shown, with both ILW calculation methods reported, corresponding to the minimum possible measurements of ILW of the EFD.

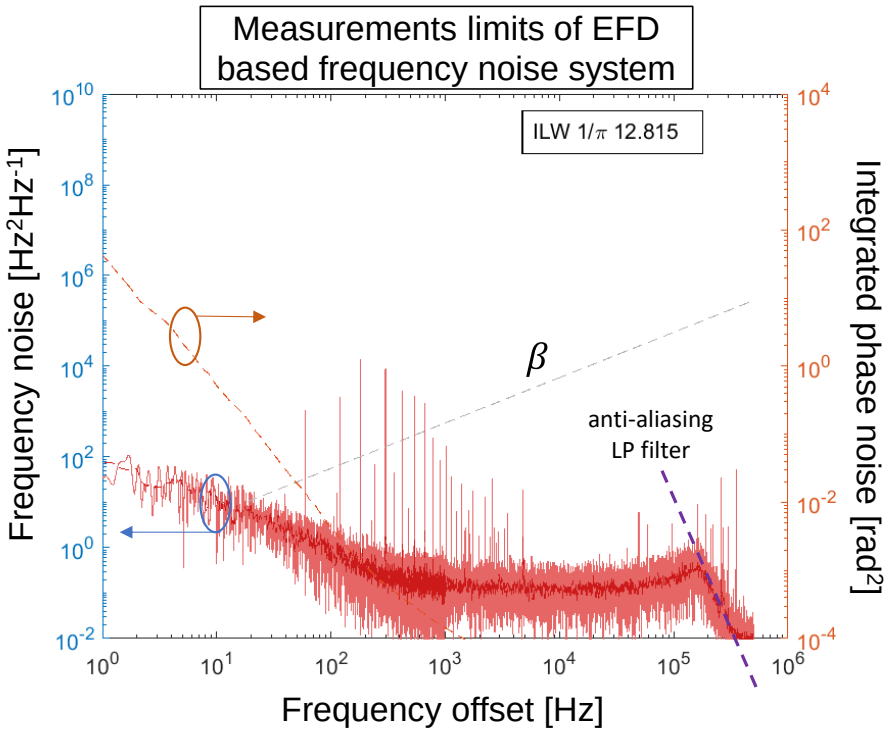

Figure 3.12. Frequency noise measurement limit of the EFD system. Integral linewidths of this frequency noise PSD were calculated using two methods, the β-separation approach [54] and phase noise integration [6], [23], [56] corresponding to the minimum ILW that can be measured by EFD.

The associated minimum measurable ILWs when using the EFD system constructed here are ~13 Hz as calculated by the phase noise integration approach, and ~47 Hz as calculated by the β-separation approach. This performance is suitable for accurate FN and ILW characterization of the lasers developed in this work, but measurements below these values such as those achieved with state-of-art table scale systems [2], [69] require a different approach [62].

In summary, this section has described optical and electrical frequency discriminator methods to measure power spectral densities of frequency and phase noise, and to measure Allan deviation of fractional frequency instability. These measurements enable the

extraction of key parameters to describe laser lineshape and stability. These methods and the key parameters used throughout this work are summarized again in Figure 3.13.

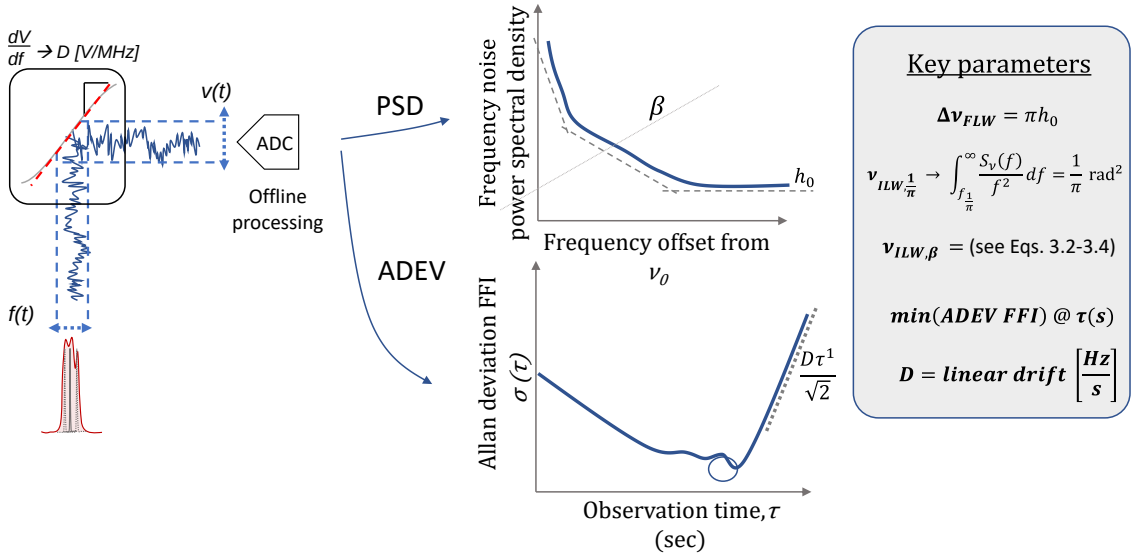

Figure 3.13. Frequency discriminators are used to convert optical and/or electrical carriers frequency fluctuations to a voltage signal that is digitized and processed offline. Data is processed offline to provide power spectral densities of frequency fluctuations and overlapping Allan deviation of fractional frequency instability. Key parameters used throughout this work to characterize laser lineshape and stability are summarized.

4 Chip-scale, spectrally pure stable lasers

4.1 Summary

This chapter presents the cavity-stabilized stimulated Brillouin scattering (CS-SBS) laser. This high spectral purity source leverages SBS lasing for fundamental linewidth narrowing, followed by a Pound-Drever-Hall (PDH) [1], [47] stabilization feedback loop to a chip-scale, ultra-high-Q optical reference cavity to both anchor the carrier and reduce the integral linewidth. The two-stage approach to linewidth narrowing developed in this work results in a several-Hz fundamental linewidth and tens-of-Hertz integral linewidth laser source with a carrier instability of ~2×10^{-13} at 100 ms [60] [6].

The first stage of the stable SBS laser is a resonantly pumped stimulated Brillouin scattering laser in a SiN ultra-low-loss ring resonator to reduce pump laser fundamental linewidth [55], [60], [70] and is discussed in Section 4.2. Measurements of frequency noise using both OFD and EFD systems are presented. Applicability to future, compact photonic integration is demonstrated with SBS linewidth narrowing of a heterogeneously integrated silicon / III-V laser [32] reducing FLW of the pump by a factor of ~600x [33]. Key results employing commercial ultra-narrow linewidth external cavity semiconductor lasers [31] as the SBS pump source are reported.

The second stage in the stable SBS laser locks the SBS laser carrier using a PDH feedback loop to an ultra-high Q optical reference cavity [18], [71] to stabilize the carrier

[6] These sections follow closely the results presented in Ref. [60].

and reduce the integral linewidth. Details of the stabilization approach, experimental setup, and measurements of ADEV fractional frequency instability of the stable SBS laser are presented in Section 4.3. A pictorial representation of the two stage linewidth narrowing and stabilization approach is shown in Figure 4.1. SBS lasing (stage 1) reduces the fundamental linewidth of a pump laser, correspondingly observed by a reduction in far-from-carrier white noise. Stabilization of the SBS laser (stage 2) reduces integral linewidth and drift, correspondingly observed as a reduction in close-to-carrier noise within the bandwidth of the PDH loop. Under closed loop operation with the carrier closely tracking the cavity resonance, frequency noise and drift of the stabilized laser is determined by the noise and drift of the cavity itself. Efforts can be made to reduce environmental noise affecting the cavity, such as by using temperature and vibration isolation enclosures, and lead to operation limited by photothermal and thermorefractive noise within the cavity itself [18], [26], [72].

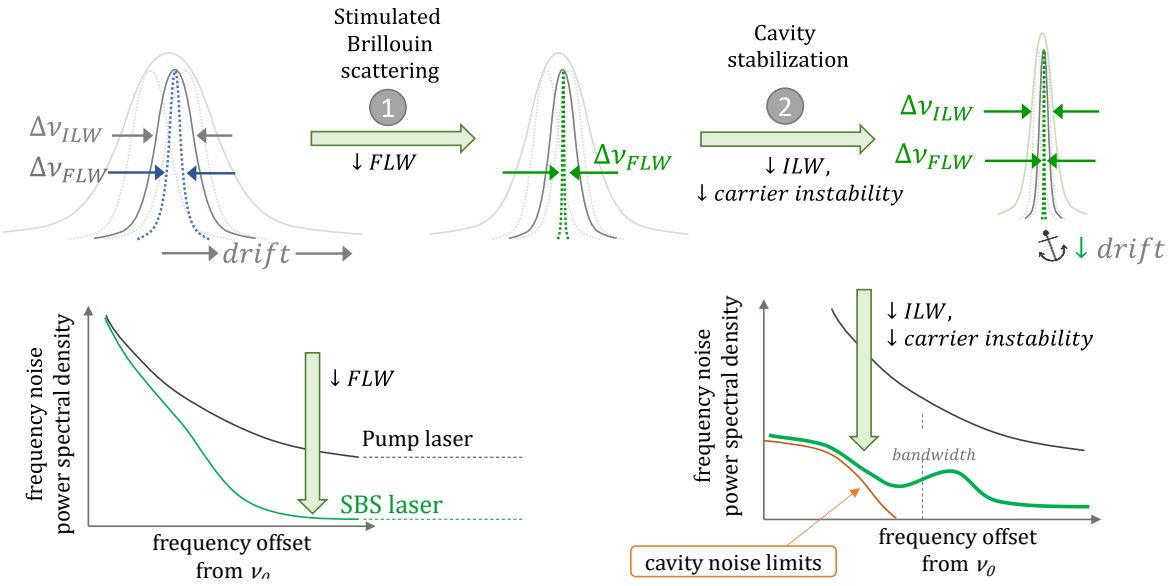

Figure 4.1. Two-stage approach to realizing a spectrally pure source with frequency noise reduction at all Fourier offset frequencies. First stage (1), Stimulated Brillouin scattering (SBS), reduces the fundamental linewidth of a pump laser (reduction in far-from-carrier, white noise) [55], [73]. The second stage (2), cavity stabilization, reduces integral linewidth and frequency drift.

Long term, robust operation of the stable SBS laser required auxiliary servo loops that actively monitored and maintained laser tunability to cavity resonances (necessary due to, for example, limited frequency tunability of acousto-optic modulators). These considerations are discussed in Section 4.5.

4.2 SBS lasing for narrow fundamental linewidth

The first stage in realizing the chip scale, high spectral purity source leverages SBS lasing for its well-known fundamental linewidth narrowing properties [34], [55], [73]–[75]. Resonant SBS lasing is realized in a weakly confined SiN ultra-low optical loss platform [70], where high optical quality factor (Q) ring resonators are realizable and critical for efficient pump linewidth reduction. In particular, the seminal work by *Debut et al* [73] shows that the reduced pump linewidth as transferred to the Stokes spectrum is given by (Eq. 4.1)

$$\Delta\nu_{s,p} = \frac{\Delta\nu_{pump}}{K^2} \tag{4.1}$$

where $\Delta\nu_{s,p}$ and $\Delta\nu_{pump}$ are the FWHM of the transferred pump noise to Stokes and pump fundamental linewidths, respectively, and the term K^2 is the linewidth reduction factor related by (Eq. 4.2)

$$K = 1 + \frac{\gamma_A}{\Gamma_c} \tag{4.2}$$

Here, γ_A and Γ_c represent the acoustic wave damping rate and cavity loss rate, respectively. Maximizing K, and therefore, improving the pump linewidth reduction factor, can be achieved by reducing the SiN cavity loss rate (decreasing photon loss) and increasing the

acoustic damping rate (increasing phonon loss). These are simultaneously realized in the SiN ring resonator device employed in this work, with a high-optical Q of 30 Million and with no guidance of acoustic modes. A rigorous treatment of Brillouin dynamics [34], [75] presents the total SBS fundamental linewidth as *a combination of linewidth broadening due to pump phase diffusion, $\Delta\nu_m^{tr}$, and from spontaneous scattering, $\Delta\nu_m$* where the contribution from scattering is dominated by thermomechanical noise from thermal phonons. The thermal phonon number at room temperature (~570) is small compared to spontaneous photons in semiconductor lasers, and therefore supports pump linewidth narrowing [34]. The total fundamental linewidth, $\Delta\nu_{SBS}$ for the SBS laser after including these contributions is then given as Eq. 4.3

$$\Delta\nu_{SBS} = \Delta\nu_m + \Delta\nu_m^{\mathrm{tr}} = \Delta\nu_m + \frac{\Delta\nu_{pump}}{K^2} \qquad 4.3$$

and therefore with large pump linewidth reduction factors is lower-limited by spontaneous phonon scattering. Further details of the SiN device fabrication and SBS lasing dynamics are developed in great detail in Refs. [34], [55], [70], [75].

An experimental schematic of pump fundamental linewidth reduction resulting in narrow fundamental linewidth of the first SBS Stokes tone (S1) is shown in Figure 4.2.

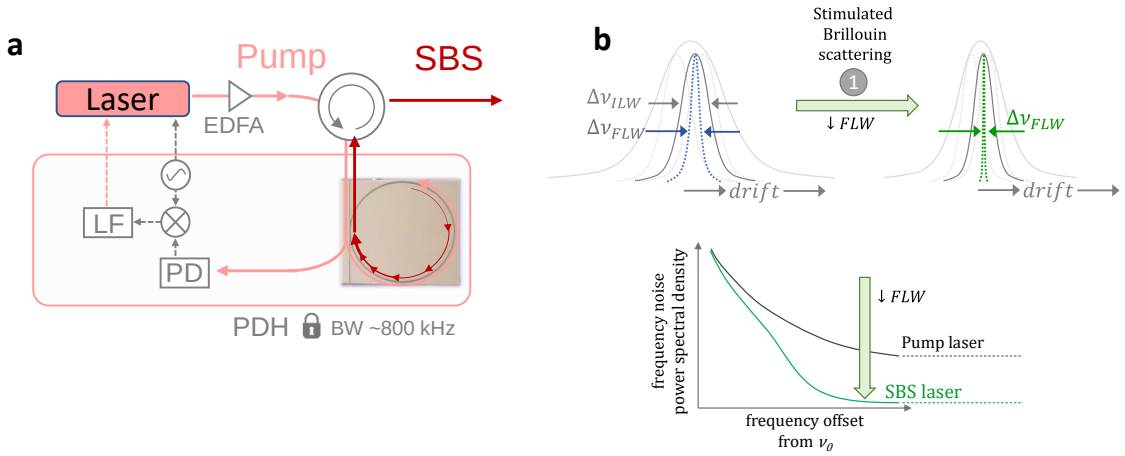

Figure 4.2. a) A pump laser is Pound-Drever-Hall (PDH) locked to a SiN ring resonator for efficient SBS lasing and to track the resonance for thermal tuning of the SiN SBS laser carrier. The PDH loop consists of a frequency synthesizer to generate PDH sidebands, a photodiode (PD), electrical mixer, and loop filter (LF). An erbium-doped fiber amplifier (EDFA) amplifies the pump laser. b) SBS lasing reduces the fundamental (Lorentzian) linewidth of the pump laser. The integral linewidth and drift can remain high for reasons such as unsuppressed technical and environmental noise transferred from the pump, thermal instability and acoustic noise affecting the SiN chip, and thermal noise (photothermal / thermorefractive) within the SiN ring resonator [55].

A pump laser is Pound-Drever-Hall (PDH) [1], [47] locked to a ~30 Million Q SiN ring resonator [34], [60] for efficient SBS lasing and to track the SiN resonance, enabling thermal tuning of the SiN PIC and therefore tuning of the SBS carrier frequency. The PDH loop consists of a voltage controlled oscillator (VCO) to generate PDH sidebands by direct current modulation of the pump laser. A photodiode (PD) detects the pump signal out of the transmission port of the resonator which is then electrically mixed with the VCO signal to downconvert the PDH sidebands and generate the PDH error signal. A proportional-integral-derivative (PID) loop filter (LF, Vescent D2-125), processes the error signal and generates servo signal that is used to tune the pump laser frequency by current control. Under closed loop operation, the pump laser closely tracks the SiN resonance with a bandwidth of ~ 800 kHz. While locked, the pump laser optical power is amplified with an

erbium doped fiber amplifier (EFDA) to reach on-chip power necessary to initiate SBS lasing.

For the 30 Million Q SiN SBS devices used in this work, threshold for first order Stokes (S1) generation is ~10 mW on-chip [55]. Increasing pump power results in decreasing fundamental linewidth of S1, with the narrowest FLW occurring just before onset of S2 lasing with on-chip optical power at a factor of 4x over S1 threshold [55], [75]. With pump linewidth reduction factors on the order of several hundred for this SiN ring resonator SBS laser design, the S1 fundamental linewidth can be reduced to below 1 Hz [55], [75].

Si/III-V heterogeneously integrated laser pumped SBS

This section presents results for an SBS laser pumped by a heterogeneously integrated InP on silicon photonic (Si/III-V) extended distributed Bragg reflector (E-DBR) laser [32]. A ~600x reduction of laser fundamental linewidth from 1.1 kHz down to 1.8 Hz (extracted from white noise floor of frequency noise measurement) and a ~9x reduction in integral linewidth from ~110 kHz to ~12 kHz (calculated using a standard integration of phase noise approach [6], [23], [56] from 10 MHz offset to the value at which integration equals $1/\pi$ rad^2) is shown. Being a waveguide integrated SiN SBS laser pumped by a heterogeneously integrated SiPh / III-V laser, this demonstration shows promise for fully integrated, CMOS foundry compatible ultra-narrow fundamental linewidth lasers. An experimental schematic for the integrated SBS laser is shown below in Figure 4.3. Results presented here follow closely Ref. [33].

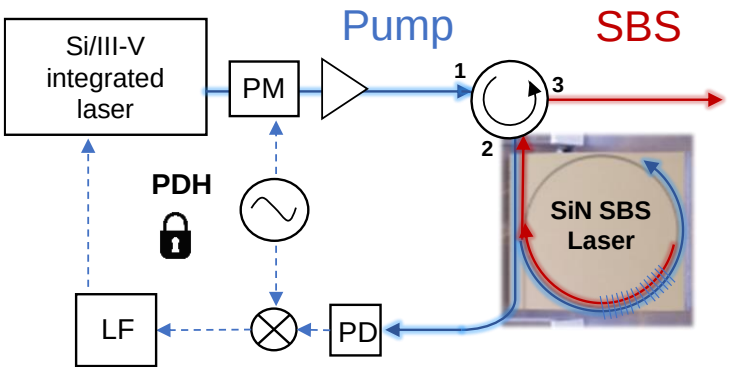

Figure 4.3. SBS lasing setup with Si/III-V pump laser. Pound-Drever-Hall (PDH) feedback loop maintains laser lock for resonant SBS pumping. PDH loop consists of RF frequency synthesizer, optical phase modulator (PM), photodiode (PD), electrical mixer, and loop filter (LF). Error signal feedback to gain section of pump laser achieves laser tuning.

The Si/III-V heterogeneously integrated E-DBR laser [32] was fabricated at the wafer-scale (4″ silicon-on-insulator SOI wafer) by leveraging the low loss wafer-bonding silicon platform [76]. With an integrated 15-mm long, low-kappa (κL = 0.375), low-loss (0.2 dB/cm), narrow bandwidth (2.9 GHz) silicon Bragg grating, the laser exhibits ~1.1 kHz fundamental linewidth and stable, long term single mode operation. The Si/III-V pump laser was fiber coupled and locked to the Si/Si_3N_4 SBS laser with a standard PDH loop to maintain pump alignment to the SiN ultra-high-Q (~30M) optical resonance for resonant SBS operation [55]. A proportional-integral^2-derivative (PI^2D) loop filter (Vescent D2-125) was used to process the PDH error signal and generate the servo signal for the PDH lock. The PDH loop bandwidth was ~ 600 kHz with maximum gain occurring below 100 kHz with integrator poles tuned to 50 kHz and 100 kHz. The servo signal was fed directly to the gain section of the Si/III-V pump laser to achieve frequency tuning via current injection.

Laser frequency noise was measured using the OFD approach for the free-running pump laser, SiN-stabilized pump laser, and SBS laser. The ‘free-running’ pump laser refers to the configuration for which the pump laser is operating under normal single mode conditions

with no PDH stabilization feedback. The SiN stabilized pump laser in the presented results refers to the Si/III-V laser FN under PDH closed-loop operation, stabilizing the pump laser carrier to the SiN 30M Q ring resonator optical resonance. In this configuration, the SiN resonance is 'cold', i.e., low optical input power (< -10 dBm), well below S1 lasing threshold. As the pump power is increased with the EDFA, S1 lasing initiates and the SBS laser frequency noise was then measured, corresponding to the third configuration. For each configuration, the FLW was calculated by estimating the white noise floor from the frequency noise PSD, and the ILWs were calculated using the β-separation method [54] and integration of phase noise method [6], [23], [61], as described previously in Chapter 3. Frequency noise results are presented in Figure 4.4.

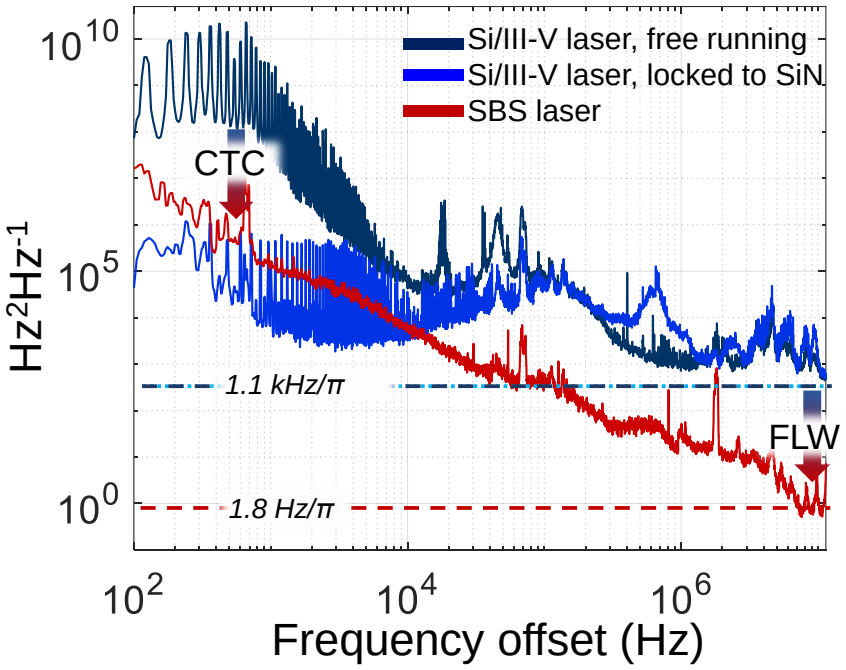

Figure 4.4. Optical frequency noise measured using an optical frequency discriminator (OFD) for the following configurations: 1) Si/III-V laser free running (with 60 Hz line noise from wall power supply used in these initial experiments resulting in FM modulated laser noise) 2) Si/III-V laser PDH locked to SiN high-Q optical resonance under cold cavity conditions (low optical power, i.e. below SBS threshold), and 3) SBS laser. Fundamental linewidth (FLW) and close-to-carrier (CTC) noise are both reduced.

The free-running pump laser FN (dark blue) falls to a minimum frequency noise level of ~ 350 Hz^2Hz^{-1}. Taking this as the white noise floor and scaling by π, the FLW of the laser is ~ 1.1 kHz [32]. The pump laser close-to-carrier (CTC) noise at frequencies below 10 kHz rises to > $1x10^8$ Hz^2Hz^{-1}, with spurs at odd integer multiples of 60 Hz power line noise from laboratory power supplies (i.e., not inherent to laser operation). Additional technical noise spurs can be observed between frequency offsets of 10 kHz to 100 kHz.

The pump laser was then locked to the SiN ring resonator optical resonance under cold cavity conditions (on-chip power below -10 dBm), shown as the light blue trace of Figure 4.4 and representing closed-loop operation. A servo bump is observed at an offset frequency of ~ 600 kHz, the PDH loop bandwidth. Beyond the loop bandwidth and servo bump, the closed-loop laser frequency noise closely follows the free running, or open-loop frequency noise as expected. Within the loop bandwidth, the laser frequency noise is improved due to the stabilization to the high-Q SiN resonator. Close-to-carrier noise, including the power line harmonics, is reduced by several orders of magnitude.

With the pump laser PDH locked to the SiN resonance, pump power was then increased using an EDFA to initiate SBS lasing with on-chip threshold of ~10 mW and up to ~40 mW, just under the onset of cascaded lasing of higher order Stokes tones occurs [34], [55], [75]. The frequency noise of the SBS laser is shown in Figure 4.4 in red. The white noise floor far-from-carrier was reduced down to ~ 0.6 Hz^2Hz^{-1}, corresponding to a FLW of ~ 1.8 Hz and a reduction from pump laser FLW of ~ 600x. In comparison to the free-running pump laser, frequency noise at all other offsets was reduced. In comparison the pump laser locked to the SiN resonance (cold-cavity conditions), frequency noise of the SBS laser is slightly

higher at low frequency offsets from photothermal and thermorefractive noise due to high intracavity optical powers necessary for SBS lasing, or 'hot-cavity' operation [26].

Fundamental and integral linewidths (ILWs calculated by β-separation [54] and $1/\pi$ [6], [23], [61] methods) for each laser configuration and for SBS lasing are summarized in Table 4.1 below.

Table 4.1. Summary of fundamental and integral linewidths of the Si/III-V pumped SBS laser

	Si/III-V free running	Si/III-V locked to SiN	SBS
FLW ($\pi \cdot h_0$)	1.1 kHz	1.1 kHz	1.8 Hz
ILW (*β-sep method*)	4.78 MHz	115 kHz	59.6 kHz
ILW (*1/π method*)	106 kHz	116 kHz	11.5 kHz

With a ~600x reduction in FLW and ~9x reduction in integral linewidth ($1/\pi$ method), this demonstration of SBS lasing for linewidth narrowing using a Si/III-V heterogeneously integrated pump laser shows promise for future, waveguide integrated and CMOS foundry compatible narrow linewidth sources. Due to the presence of larger non-white frequency noise close-to-carrier (and correspondingly, a lineshape that diverges with longer observation times or larger integration timescales), the integral linewidths calculated by the β-separation method are larger than those calculated by the $1/\pi$ method (see Chapter 3.4 for more detail).

4.3 Reference cavity stabilization for stable carrier, narrow ILW

This section discusses the second stage in realizing a spectrally pure SBS source, PDH locking of an SBS laser to a chip-scale optical reference cavity, to anchor the carrier and reduce laser frequency noise within the loop bandwidth. The result is a drastic decrease in

integral linewidth and reduction of laser carrier drift. Measurements of frequency noise spanning carrier offsets of 1 Hz to 1 MHz using OFD and EFD methods are presented. ADEV of fractional frequency instability (FFI) results are shown. Fundamental and integral linewidths are calculated from the frequency noise spectra.

As previously discussed, SBS lasing enables an ultra-narrow fundamental linewidth, but the carrier can remain relatively unstable leading to a broadened integral linewidth at intermediate timescales and drift of the laser lineshape at longer timescales. A PDH lock of the SBS laser to a stable reference cavity [18] reduces frequency noise within the loop bandwidth which and correspondingly reduces the integral linewidth and drift. .An illustration of an SBS laser stabilized to a chip-scale Fabry-Perot (FP) ultra-stable reference cavity is shown in Figure 4.5.

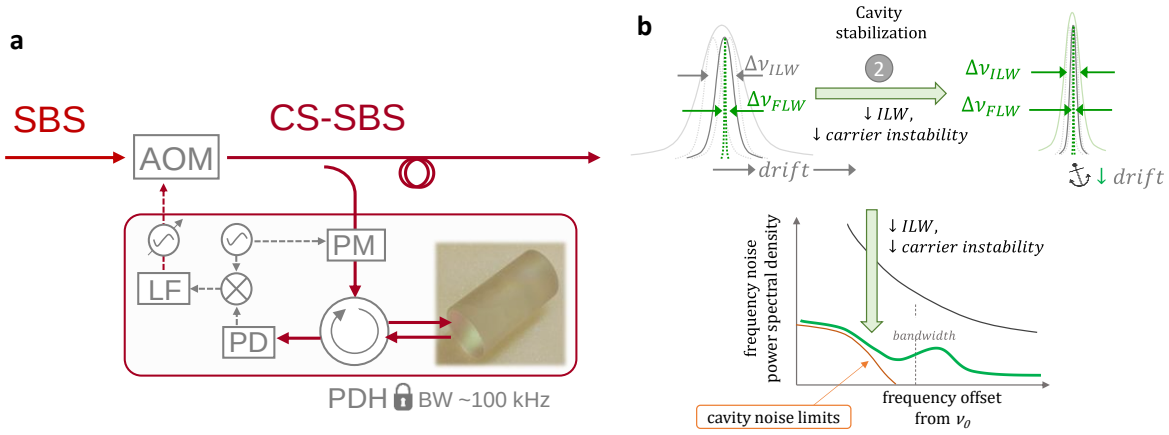

Figure 4.5. a) An SBS laser is stabilized to a chip-scale optical reference cavity using a standard Pound-Drever-Hall feedback loop. An acousto-optic modulator (AOM) is used to frequency tune the SBS laser. The PDH loop consists of a frequency synthesizer, optical phase modulator (PM), avalanche photodiode (PD), electrical mixer, loop filter (LF) and voltage controlled oscillator. The cavity-stabilized stimulated Brillouin scattering (CS-SBS) laser is the stable output of the AOM under closed loop operation [60]. This second stage that stabilizes the SBS carrier reduces integral linewidth and drift (b), thus realizing a source with reduced frequency noise at all Fourier offset frequencies and spectrally pure operation.

In this work, the reference cavity used in SBS stabilization experiments was a >1 Billion Q Fabry-Perot (FP) chip-scale bulk cavity housed in an environmental isolation enclosure[7]. More details on the cavity design and fundamentals can be found in Ref [18].

Frequency tunability of the SBS laser was achieved using a fiber coupled acousto-optic modulator (AOM) configured in frequency shifter mode (using the first order diffraction mode, rather than fundamental as is common for AOM based high extinction switches). In this configuration, the AOM shifts the optical frequency by the RF frequency that drives the AOM. By driving the AOM with a tunable RF source, such as a voltage controlled oscillator (VCO), the SBS laser optical carrier is made actively tunable. This approach enables closed loop control of the SBS laser frequency, as is necessary for a PDH lock. Another approach to frequency tuning SBS laser carriers without the use of an AOM can be realized via photothermal tuning of the SBS cavity, as was done in Ref. [21]. SiPh integrated single sideband (SSB) modulators could also be used to tune laser carriers in an integrated form factor [77].

The chip-scale compact reference cavity [18] and experimental setups are shown in Figure 4.6 and Figure 4.7. An aluminum and Teflon enclosure was fabricated to environmentally isolate the cavity from thermal and vibrational noise, with multiple sub-enclosures and Teflon spacers to optimize isolation. Additional information on enclosure design for minimizing environmental noise can be found in Ref. [18]. Sealed windows on the metal enclosure enable free-space optical coupling to the cavity mode.

[7] The >1 Billion Q optical reference cavities were provided by collaborators at The National Institute of Standards and Technology (NIST). Details on the cavity design and team of contributors are provided in Ref. [18]

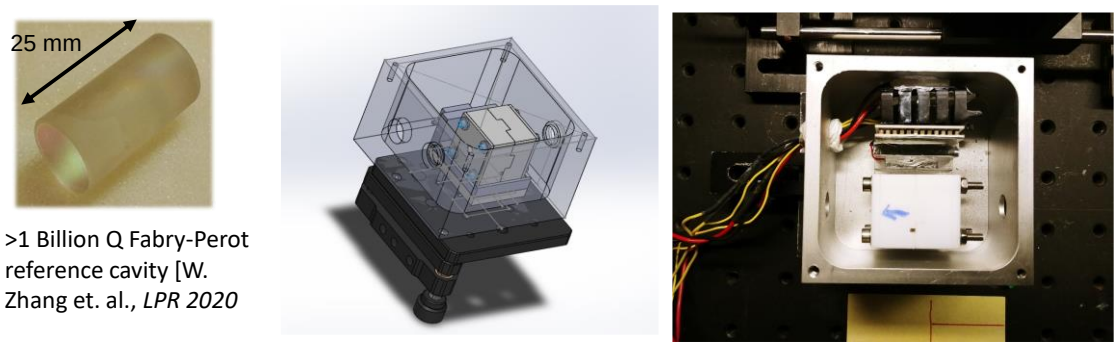

Figure 4.6. Unhoused optical reference cavity [18] (left). 3D model of the fabricated enclosure to house the cavity (middle). Cavity secured inside the enclosures, with electrical access to thermo-electric coolers (TEC) for temperature control.

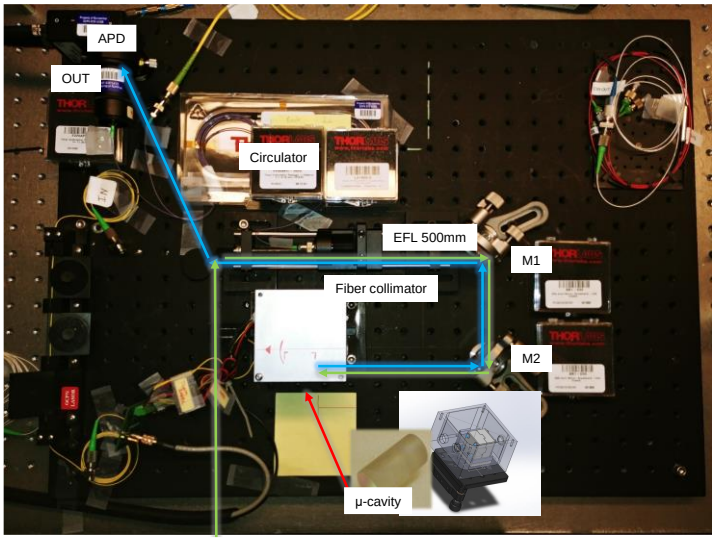

Figure 4.7. Tabletop setup of fiber collimator to free space coupling of the laser mode to the fundamental cavity mode of the Fabry-Perot resonator. A lens with 500 mm effective focal length and two turning kinematic-mounted mirrors enabled optical alignment.

4.4 Combining SBS linewidth narrowing and cavity stabilization

By combining the two previously described subsystems for linewidth narrowing (SBS lasing for FLW reduction and cavity stabilization for ILW reduction), the cavity-stabilized stimulated Brillouin scattering (CS-SBS) laser is realized. The full experimental setup for this stable SBS laser is shown in Figure 4.8.

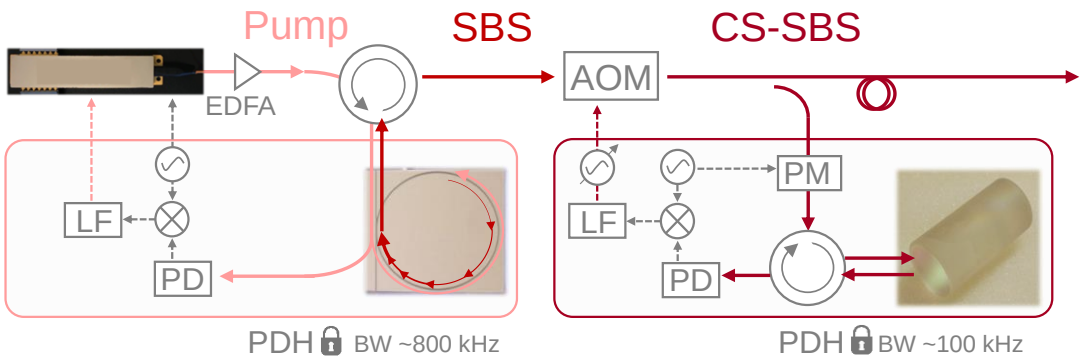

Figure 4.8. The cavity stabilized stimulated Brillouin scattering (CS-SBS) laser. The pump laser (extended cavity diode laser, ECDL [31]) is amplified by an erbium doped fiber amplifier (EDFA) to pump the SBS laser. An acousto-optic modulator enables frequency tunability of the SBS carrier necessary for the Pound-Drever-Hall (PDH) lock to a >1 Billion Q Fabry-Perot reference cavity [18].

The frequency noise was measured for the pump laser, SBS laser, and CS-SBS laser to demonstrate the reduction in laser frequency noise at each stage. Frequency noise of optical carriers was directly measured using the OFD system previously described in Chapter 3. The OFD measurements are suitable for high frequency offsets and extraction of fundamental linewidth. However, fiber noise in the OFD system limits FN measurements at offset below ~ 10 kHz, requiring ans EFD method to be used for close-to-carrier measurements and drift. An EFD measurement on a beat note intermediate frequency required a second laser for an optical heterodyne. To enable these measurements, a stable SBS laser (Figure 4.8) of the same design was constructed, forming a 'transmitter' and 'receiver' pair (Tx/Rx). ADEV FFI for the heterodyne of the two stable SBS lasers was also calculated from the EFD results. A schematic showing the Tx-Rx pair of the stable lasers and measurement locations for the OFD and EFD systems is shown in Figure 4.9. The results presented here follow closely the published results in Ref. [60].

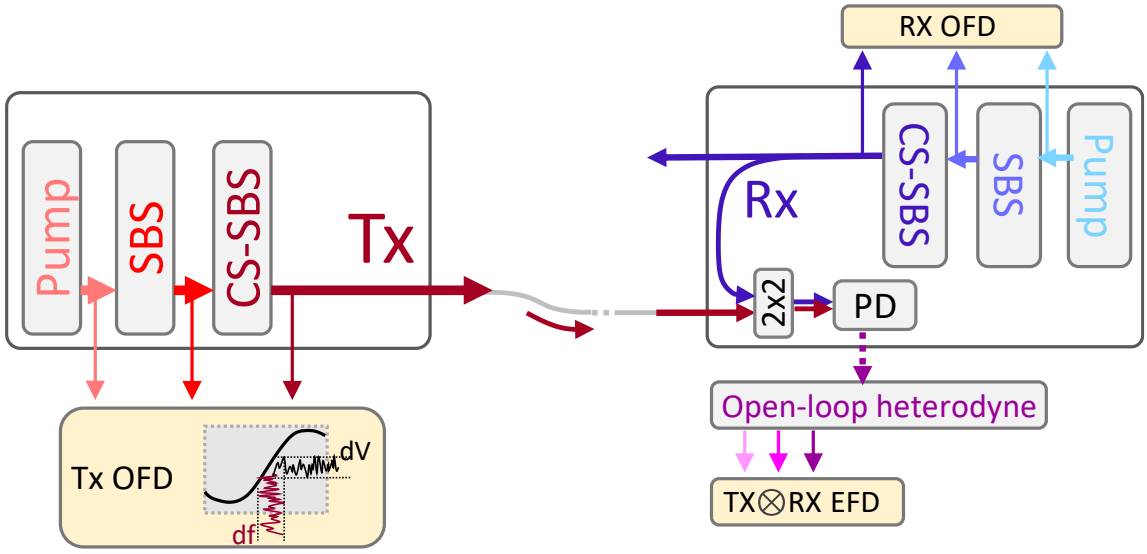

Figure 4.9. Linewidth narrowed, cavity stabilized lasers connected as transmitter (Tx) and receiver (Rx) pair. Frequency noise of Tx and Rx Pump, SBS, and cavity stabilized SBS (CS-SBS) optical carriers were measured with optical frequency discriminator (OFD). The Tx-Rx heterodyne beat note frequency noise was measured using an electrical frequency discriminator (EFD).

Far-from-carrier frequency noise

Frequency noises of the transmitter and receiver pump, SBS, and CS-SBS lasers measured with the OFD system[8] are presented in Figure 4.10.

[8] Optical frequency discriminator measurements are median-filtered to remove artificial spurs due to inverting the MZI transfer function (having zeros at integer multiples of FSR), resulting in smoothed traces presented here.

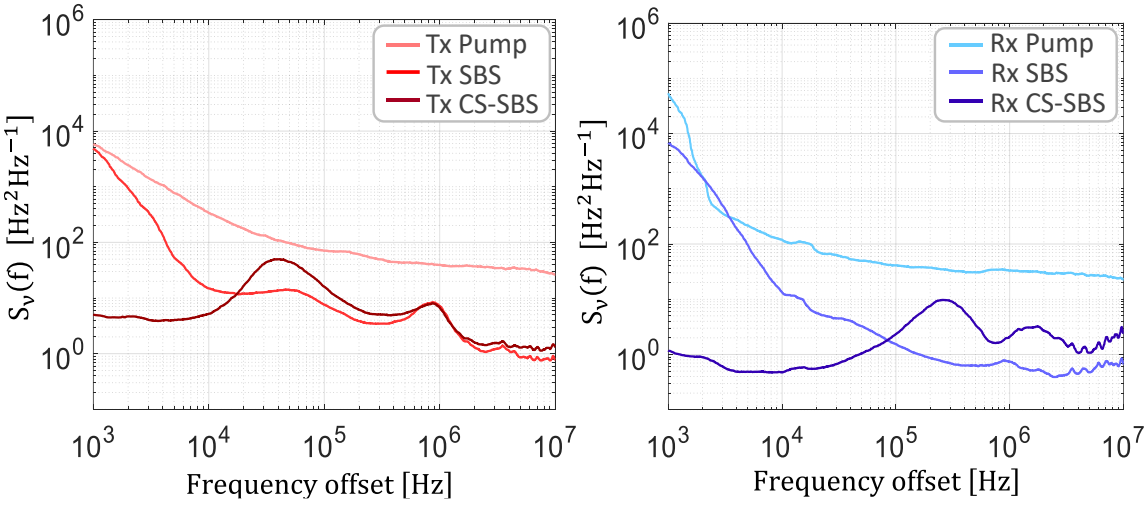

Figure 4.10. Frequency noise of pump, SBS, and cavity-stabilized SBS (CS-SBS) transmitter (Tx) and receiver (Rx) lasers made using an optical frequency discriminator (OFD).

The FN traces presented in Figure 4.10 demonstrate key aspects of the two-stage linewidth narrowing approach of cavity-stabilized SBS laser: 1) reduction of far-from-carrier noise (fundamental linewidth) via SBS lasing, and 2) reduction of close-to-carrier noise via cavity stabilization. Comparing the Tx/Rx pump (light red/blue) laser frequency noise at high offset frequencies (>1 MHz) to frequency noise of the SBS laser (medium red/blue), the effect of SBS linewidth narrowing is evident with a reduction of FN from ~ 30 Hz^2Hz^{-1} down to ~ 1 Hz^2Hz^{-1}. Close-to-carrier noise remains high due to photothermal [26] and technical noise.

The effects of cavity stabilization are apparent when comparing FN traces for Tx/Rx SBS lasers (medium red, blue) and Tx/Rx cavity-stabilized SBS lasers (dark red, blue). The bandwidths of the PDH loops are ~50 kHz and ~200 kHz for Tx and Rx stable SBS lasers, respectively, based on locations of the servo bumps due to gain peaking in the feedback loops. Within these loop bandwidths, SBS laser noise was reduced by the active

stabilization to the reference cavities, from ~ $1x10^4$ Hz^2Hz^{-1} to a minimum of ~ 5 Hz^2Hz^{-1} for Tx and ~ 0.5 Hz^2Hz^{-1} for the Rx stable SBS laser.

Close-to-carrier frequency noise

To characterize the effects of cavity stabilization at offset frequencies below 1 kHz, the electrical frequency discriminator system described in Section 3.2 was employed to measure the heterodyne beat note between Tx and Rx pump, SBS, and stable SBS lasers as shown in Figure 4.11. The EFD measurements are stitched into the summed FN of each independent Tx/Rx laser as measured by the OFD system and previously plotted in Figure 4.10.

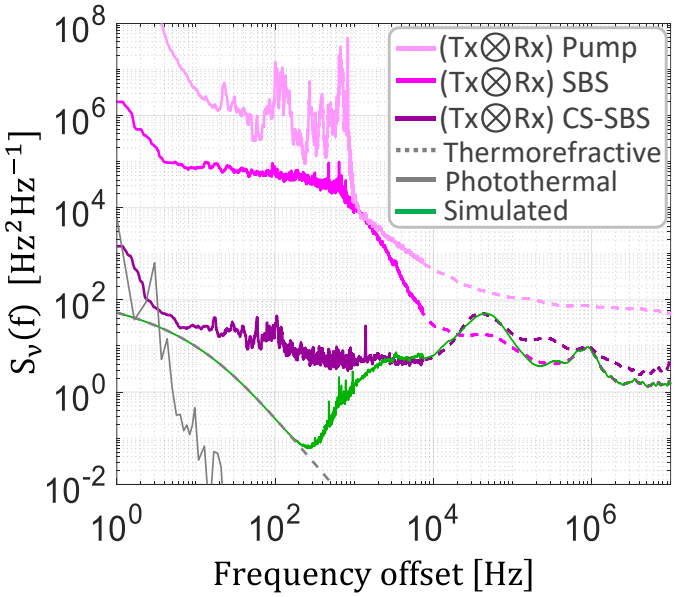

Figure 4.11. Close-to-carrier frequency noise for the beat note between Tx and Rx pump lasers (light purple), SBS lasers (medium purple), and cavity stabilized SBS (CS-SBS, dark purple) lasers using an electrical frequency discriminator. Dotted lines are the summed optical frequency noises of Tx and Rx measured by OFD (plotted in Figure 4.10). Cavity thermal noise limit (grey dashed) and photothermal noise (grey solid) are shown. A simulation of a CS-SBS laser limited only by cavity thermal noise is shown (green).

Close-to-carrier noise was slightly reduced by the SBS lasing stage, as observed in comparing beat note frequency noise of the pump lasers (light purple) and SBS lasers (medium purple). Frequency noise of the SBS lasers at carrier offsets below ~10 kHz was

dominated by photothermal noise in the SiN cavity, or conversion of optical power fluctuations to frequency noise of the SiN resonance. This results in the low-pass filter shape with cutoff frequency of ~ 1 kHz observed in the SBS FN traces, governed by the time constant of power fluctuations being converted to material temperature fluctuations affecting the optical mode of the resonator [26].

The effects of cavity stabilization can be observed by comparing the FN of the Tx/Rx SBS beat note (medium purple) with the Tx/Rx stable laser beat note (dark purple). Close-to-carrier noise at offsets below ~ 1 kHz was reduced by ~ 4 orders of magnitude, from $1x10^5$ Hz^2Hz^{-1} down to ~ 10 Hz^2Hz^{-1}. Frequency noise of the CS-SBS lasers approached the fundamental thermal noise of the reference cavity (plotted in grey dashed). Photothermal noise is also plotted (grey solid) showing the conversion of optical intensity noise to frequency noise within the reference cavity. A simulation of an SBS laser stabilized to the reference cavity limited by only fundamental thermal noise is shown in green[9].

Allan deviation fractional frequency instability (FFI)

The Allan deviation (ADEV) fractional frequency instability (FFI) of the heterodyne beat note between Tx/Rx CS-SBS lasers was characterized using the EFD and is shown in Figure 4.12. The time domain signal of frequency fluctuations is plotted on the left, with and without linear drift of 803 Hz/s removed.

[9] Cavity thermal noise limits, photothermal noise limits, and simulations of a stabilized laser limited only by cavity thermal noise were conducted by J. Dallyn and are gratefully acknowledged [60]

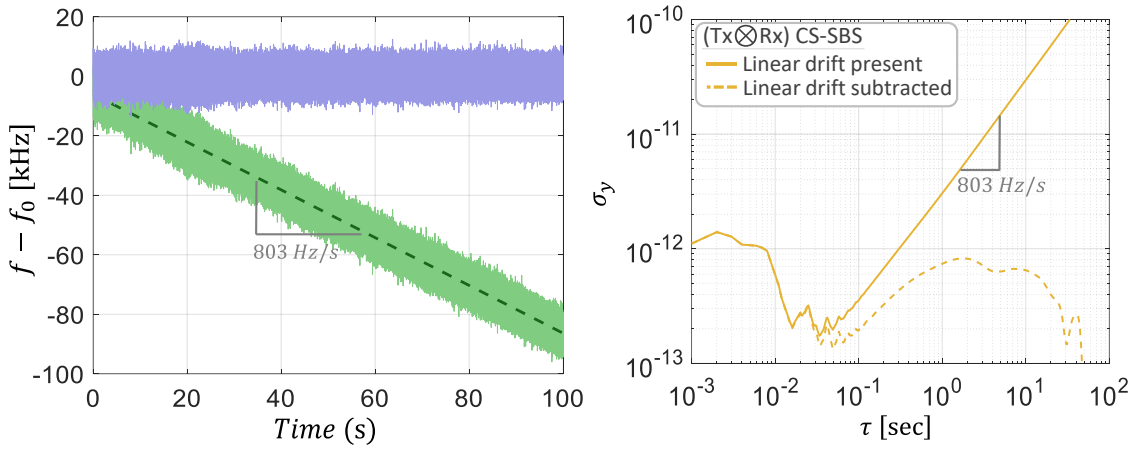

Figure 4.12. Time domain frequency fluctuations of the heterodyne beat note between transmit and receiver (Tx/Rx) cavity stabilized SBS (CS-SBS) lasers with linear drift of 803 Hz/s present (green) and removed (blue). Overlapping Allan deviation (ADEV) fractional frequency instability (FFI) reaches a minimum of < $2\text{x}10^{-13}$ at observation period τ of ~50 ms. Impact of drift is shown by subtracting the linear 803 Hz/s (dotted yellow).

Overlapping Allan deviation (ADEV) fractional frequency instability (FFI), $\sigma_y(\tau)$, reaches a minimum of < $2\text{x}10^{-13}$ at observation period τ of ~50 ms. Impact of drift is shown by subtracting linear drift 803 Hz/s (dotted yellow).

Integral linewidths

Integral linewidths were calculated by the two methods (β-separation [54] and integration of phase noise [6], [23], [61]) described in Section 3.4 using the frequency noise measurements of the heterodyne beat note between transmit and receive cavity-stabilized SBS lasers.

Integral linewidth calculations using the β-separation method [54] are visualized in Figure 4.13, with FN regions exceeding the β-separation line, and therefore contributing to linewidth, shaded in solid colors.

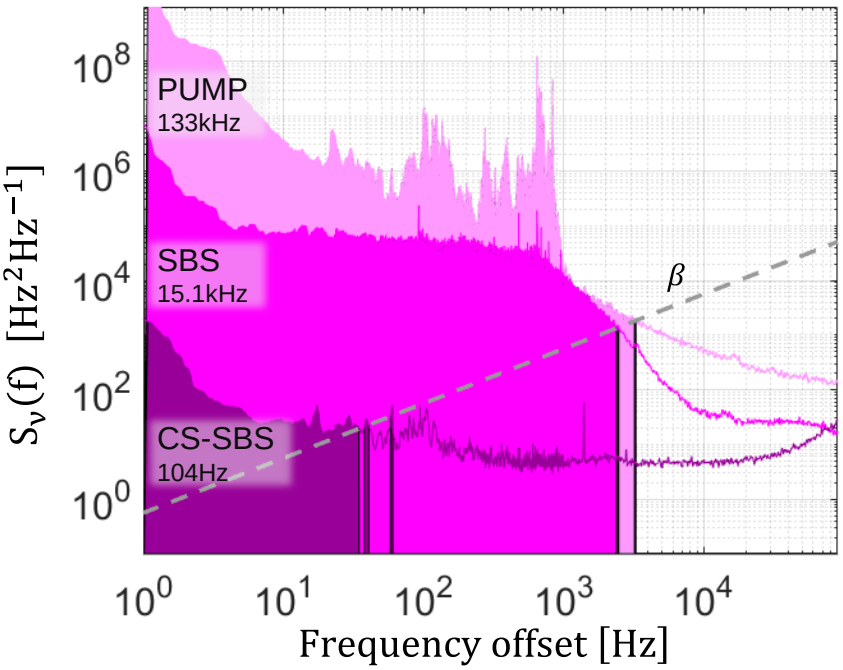

Figure 4.13. Visualization of the β-separation approach to calculating integral linewidths [54]. Frequency noise that exceeds the β-separation line contributes to linewidth broadening.

As calculated by the *β*-separation method, the integral linewidth of the heterodyne beat note between the transmit and receive pump lasers was found to be 133 kHz. After the SBS lasing stage for reducing fundamental linewidth, the heterodyne beat note ILW of the SBS lasers was calculated as 15.1 kHz. After the cavity stabilization stage, employed for reduction of integral linewidth and drift, the CS-SBS heterodyne ILW was reduced to 104 Hz. This corresponds to a ~1280x reduction in ILW of the pump laser in comparison to the CS-SBS laser.

The second approach to calculating ILW, reverse integration of phase noise [6], [23], [61] is visualized in Figure 4.14 for heterodyne beat notes of pump, SBS, and CS-SBS lasers. The y-axis is the integrated phase noise from the highest measured offset frequency down to *f*, the offset frequency on the x-axis (the integral relation is given by Eq. 3.5).

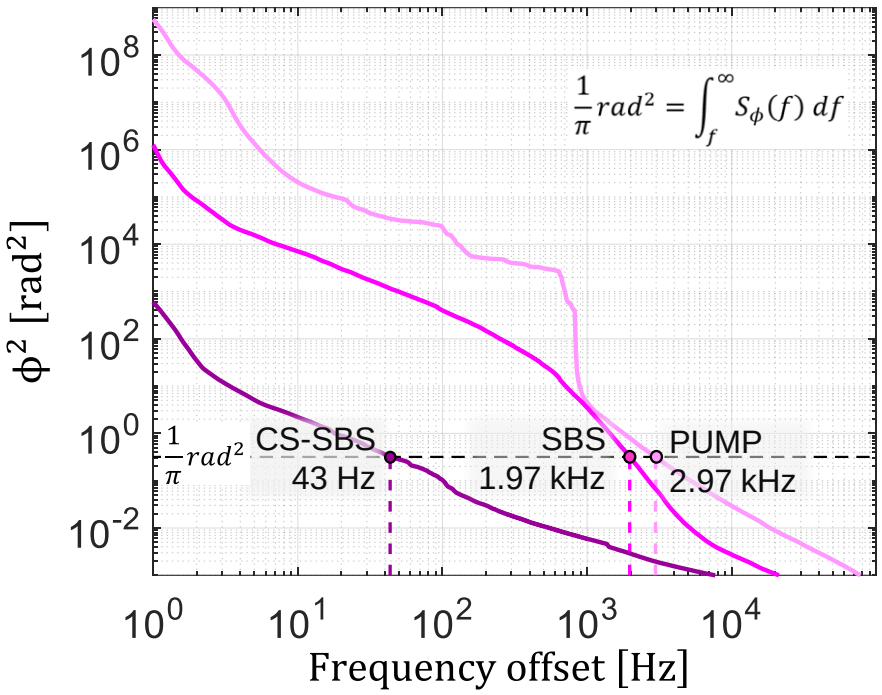

Figure 4.14. Integration of phase noise for heterodyne beat notes between transmit and receive pump lasers (light purple), SBS lasers (medium purple), and cavity stabilized SBS lasers (dark purple), from highest offset frequency down to 1 Hz. Dotted line shows level of $1/\pi$ rad^2.

The offset frequency at which the integrated phase noise equals $1/\pi$ rad^2 is the associated '$1/\pi$' integral linewidth. The ILWs of the heterodyne beat note between Tx/Rx pump lasers, SBS lasers, and CS-SBS lasers were found to be 2.97 kHz, 1.97 kHz, and 43 Hz, respectively. Since the heterodyne beat note measured by the EFD captures the combined noise of both lasers under test, the ILWs calculated using the associated FN are the combined linewidths of the two independent lasers. Assuming Gaussian lineshapes and equal contribution from each laser to the 43 Hz heterodyne linewidth, each independent optical linewidth for the Tx and Rx CS-SBS lasers is estimated to be ~30 Hz. This estimate assumes $1/\sqrt{2}$ contribution from each source, stemming from RMS addition of equal linewidths in which Gaussian FWHMs add [78]. A summary of fundamental linewidths for

the independent transmit and receive pump, SBS, and stable SBS lasers and of the integral linewidths for their respective heterodyne beat notes are shown in Table 4.2.

Table 4.2. Summary of FLW and ILWs

	$\Delta\nu_{FLW}$ (OFD)	*ILW* (EFD, Tx-Rx beat note)	
	$\Delta\nu_{Tx}, \Delta\nu_{Rx}$	(1/π)	(β-sep)
Pump	90 Hz, 60 Hz	3.0 kHz	133 kHz
SBS	1.4 Hz, 0.9 Hz	1.97 kHz	15.1 kHz
CS-SBS	1.8 Hz, 1.8 Hz	43 Hz	104 Hz

Here again it is noted that due to the presence of non-white frequency noise close-to-carrier (and correspondingly, a lineshape that diverges with longer observation times or larger integration bounds closer-to-carrier), the integral linewidths calculated by the β-separation method are larger than those calculated by the 1/π method (see Chapter 3.4 for more detail).

While the Tx-Rx heterodyne beat note EFD measurements are suitable for capturing the combined noise of two lasers, uniquely identifying Tx and Rx noise contributions required a different measurement approach. To overcome this limitation, the Tx and Rx lasers were independently heterodyned with a narrow linewidth fiber laser stabilized to an ultra-stable, commercial state-of-art reference cavity (Stable Laser Systems notched cavity) serving as an 'ideal' reference laser. With the frequency noise and stability of the reference laser far superior to the chip-scale stable lasers, the heterodyne beat note measured by this setup is dominated by the test laser noise and therefore suitable for uniquely characterizing each Tx and Rx stable laser independently. A plot of these reference laser heterodyne beat note EFD measurements with Tx and Rx stable lasers is shown in Figure 4.15.

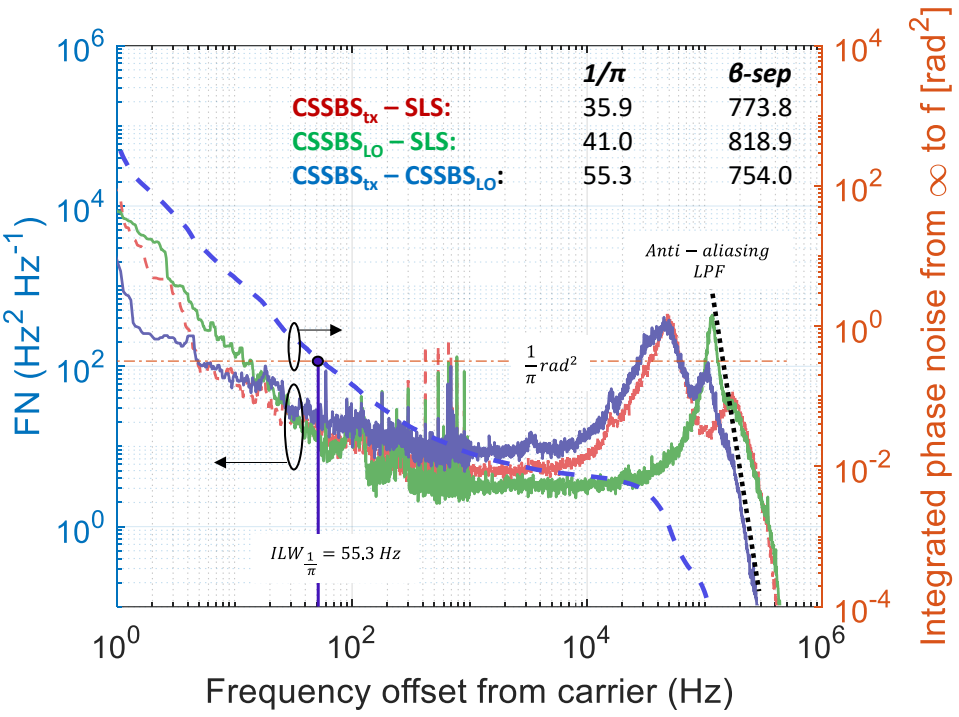

Figure 4.15. EFD measurements (with anti-aliasing low-pass filter) of the heterodyne beat note between a commercial, ultra-stable reference laser system (Stable Laser Systems SLS) and transmit/receive (Tx/Rx) cavity-stabilized SBS lasers. Integral linewidths calculated by phase noise integration [6], [23], [61].

Assuming the noise and stability of the SLS reference laser to be much better than either of the test lasers, the traces for frequency noises of the SLS heterodyne with Tx and Rx stable lasers (plotted in red (Tx) and green (Rx)) are taken to represent the unique noise of each independent stable laser (and will be referred to as independent FN for each laser moving forward). Also plotted is the heterodyne between the Tx and Rx stable lasers (blue). We would expect the sum of the independent FN traces for the Tx and Rx stable lasers (red, green) to match the frequency noise of the heterodyne between them (blue) if the following conditions are true:

1) The stable SBS laser noises are uncorrelated
2) The SLS reference laser noise does not contribute to its heterodyne measurements with the CS-SBS lasers

Violating item (2) would result in the sum of the 'independent' CS-SBS traces to be greater than the plotted heterodyne (blue) due to a non-negligible contribution of SLS noise to each heterodyne measurement. However, at low offset frequencies the noise of the Tx-Rx CS-SBS heterodyne actually falls *below* both frequency noises of the Tx and Rx CS-SBS lasers. This implies that item (1) is not met – the independent Tx and Rx CS-SBS laser noises are not uncorrelated. This is possibly explained by coupled drift of the chip-scale reference cavities when the measurements were taken; with both stabilization cavities drifting in the same direction, the relative drift would in fact be lower than the absolute drift. This is reasonable, as the reference cavity drift in these experiments was primarily determined by the long timescale (hours/daily) laboratory temperature fluctuations – since the cavities shared a lab space, their drift was coupled.

4.5 Spectral map of optical resonances and frequency tuning

The cavity-stabilized SBS laser involves resonant optical structures with varied free spectral ranges (FSRs) and tunability in each stage of linewidth narrowing. In stage one, the pump laser is locked to the SiN high-Q resonance for SBS lasing. In stage two, the SBS laser is locked to the ultra-high Q stable reference cavity resonance. Additionally, the system employed optical devices with limited frequency tunability and dynamic range, such as the limited single mode operation regions of the pump lasers and limited frequency tunability of acousto-optic modulators (AOMs). Achieving long term, robust operation required careful mapping and positioning of optical resonances and design of auxiliary servos to actively monitor these alignments. A simplified stable SBS laser system schematic

with lasers and key resonant devices color-coded and the associated spectral map are shown in Figure 4.17 and Figure 4.17.

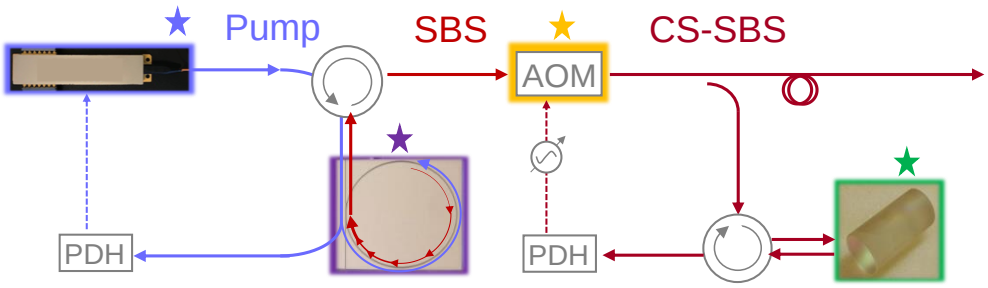

Figure 4.16. Schematic of the CS-SBS laser with key resonant and/or frequency tunable elements color-coded: pump laser (blue), SiN ring resonator (purple) for SBS lasing (red), acousto-optic modulator (AOM, yellow) operated as a frequency tuner, chip-scale ultra-stable optical reference cavity (green), and cavity-stabilized SBS laser (dark red).

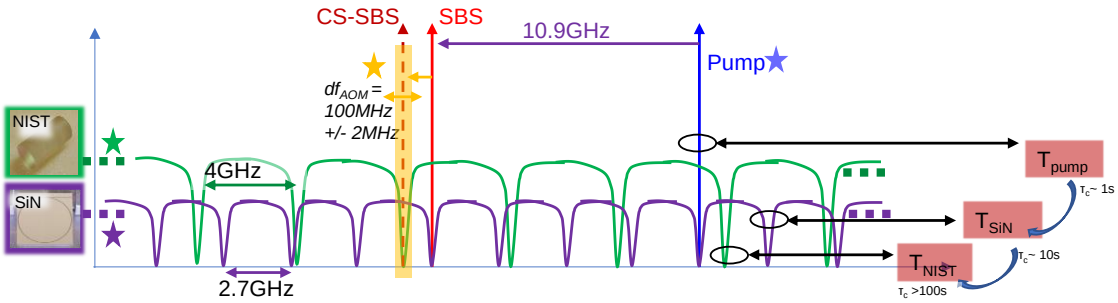

Figure 4.17. Spectral map of key resonant and/or frequency tunable elements color-coded to match reference schematic in Figure 4.16 per the following: pump laser (blue), SiN ring resonator (purple) for SBS lasing (red), acousto-optic modulator (AOM, yellow) operated as a frequency tuner, chip-scale ultra-stable optical reference cavity (green), and cavity-stabilized SBS laser (dark red dotted).

Since the final stabilization element is the chip-scale reference cavity (green), its resonance frequency ultimately determines the CS-SBS carrier frequency (dark red, dotted). Therefore, a straightforward manner to understand the relations shown in the spectral map is by tracing the stages in reverse order, from the CS-SBS laser to pump laser, as follows:

1) Under closed-loop operation, the CS-SBS laser (dark red, dotted) was locked to a resonance of the chip-scale stable reference cavity (green).

2) The frequency tunability required to enable this lock was achieved using an acousto-optic modulator (AOM, yellow) with nominal frequency shift of 100 MHz and operation window ± 2 MHz (yellow). As such, the SBS laser carrier (red) was nominally at a frequency blue-shifted from the reference cavity by ~ 100 MHz.
3) In the SBS generation process, the first order Stokes SBS lasing is frequency offset from the pump laser (blue) by a Brillouin frequency shift of ~ 10.9 GHz [55].
4) The pump laser frequency was therefore positioned at a frequency greater than the CS-SBS laser by 10.9 GHz + 100 MHz ≈ 11 GHz.

For long term operation, an auxiliary servo loop was required to maintain tunability within the AOM operation window of ± 2 MHz. Without active monitoring, the AOM servo signal can reach its tuning limits due to SBS carrier frequency drift caused by environmental temperature fluctuations of the lab (and therefore temperature drift of the SiN PIC). This monitor was implemented by periodically reading (every ~ 5 seconds in a software defined loop) the servo signal of the AOM and triggering a 'correction' if the signal neared the limits of its range. The applied correction was an adjustment to the temperature of the SiN device to shift the frequency of the SBS laser, recentering the SBS carrier in the AOM operation window. The pump laser for SBS generation, being PDH locked to the SiN resonator, would respond by tracking the resonance shift to the new setpoint. After numerous temperature shifts over the span of a day, the pump laser would begin to reach its current-tuned single mode region limits. The pump laser therefore also required monitoring and correction using a feedback loop to the setpoint temperature of its cavity grating [31]. With these auxiliary feedback loops actively coordinating coarse resonance and tuning alignments, the CS-SBS laser was routinely operated in uninterrupted fashion over entire

days. This level of reliability was critical for CS-SBS laser demonstrations in further system-scale experiments, such as the optical phase synchronization discussed in Chapter 5 and the coherent link demonstration in Chapter 6.

5 Optical phase synchronization over fiber

5.1 Summary

In this chapter, transmitter and receiver stabilized lasers are optically phase synchronized to realize the optical-frequency-stabilized phase locked loop (OFS-PLL) [60]. To do this, the receiver-side stable laser is made tunable using a single-sideband modulator or AOM to form a tunable local oscillator (LO). Optically mixing the transmit and tunable LO stable laser carriers on balanced photodetector generates the phase error signal for a homodyne phase lock [35]. The error signal is processed using low frequency (<1 MHz) analog proportional-integral-derivative (PID) electronics and fed back to the tunable LO to close the loop. Performance of the loop is characterized by measuring the residual phase error power spectral density (PSD) of the phase lock under closed loop operation. Benefits of employing the stable lasers for the OFS-PLL are demonstrated by achieving an ultra-low residual phase error variance using only low bandwidth, low power electronics.

In Section 5.2, key parameters and metrics of an optical phase lock are defined and discussed. A linear, time-invariant (LTI) model of an optical phase locked loop is briefly reviewed and a block diagram of a standard OPLL is compared to the experimental realization of the OFS-PLL. Simple models of an OPLL using parametric laser phase noise are presented to show the impact of using narrow linewidth lasers in an OFS-PLL to achieve ultra-low residual phase error. A model comparison of residual phase error for OPLLs employing various standard lasers is then presented alongside CS-SBS lasers.

Section 5.5 demonstrates the OFS-PLL operation and characterizes performance in terms of the previously defined standard phase locked loop metrics [79]. Finally, Section 5.6 briefly discusses future opportunities for the OFS-PLL, such as waveguide integration of reference cavities, single sideband modulators, and pump lasers and co-location of low power bipolar-CMOS electronics.

5.2 Simple model OPLLs, key parameters

In this section, an optical phase locked loop [35]–[37], [39]–[43], [80]–[82] is reviewed as a linear time-invariant (LTI) negative feedback system. Standard LTI analysis and tools are applied to optical phase lock performance for lasers that have various phase noise power spectral densities (PDSs). Key terms and parameters that describe PLL (and OPLL) performance are defined and discussed.

First, several parameters commonly used to characterize PLL operation and performance are defined:

Table 5.1. List of common terms used to describe phase locked loops and their performance

Term	Symbol	Definition	Units	Reference(s)
PLL order	1^{st}, 2^{nd}, …	polynomial order of denominator of closed loop system transfer function; number of poles of system	-	[79]
PLL type	I, II, …	number of ideal integrators; poles at origin[10]	-	[79]

[10] PLLs that have a frequency-controllable oscillator (e.g., voltage/current controlled oscillators) are at minimum a Type I system. *Frequency* is tuned directly, while the error signal measures *phase*. Phase is the time integral of frequency, therefore the unit behaves as an integrator (places a pole at origin)

pull-in range	-	maximum frequency difference between reference and tracking oscillators for which engaging the PLL results in successful lock acquisition. Including a loop that acts on frequency error rather than phase error is sometimes employed to extend pull-in range	Hz	[79]
lock-acquisition range	-	maximum frequency difference between reference and tracking oscillators for which engaging the PLL results in successful lock acquisition *with no fringe slips (phase error goes directly to locked state with no excursion exceeding ± π/2)*	Hz	[79]
hold-in range	-	under closed-loop operation, reference and tracking oscillator frequencies can be nominally tuned apart (phase lock servo resists this and continues to maintain lock), until lock disengages. The 'free running' frequency difference at which this occurs is hold-in range	Hz	[79]
bandwidth	BW	frequency offset for unity gain of a stable loop	Hz	-
residual phase error power spectral density	$S_{\phi,e}$	Power spectral density of the residual phase error signal (in-loop phase error)	rad^2/Hz	[79]
residual phase error variance	σ_ϕ^2	Variance of the residual phase error signal (in-loop phase error). Can be calculated by integrating $S_{\phi,e}$	rad^2	[35]–[38], [79]

A simple block diagram showing components of a standard phase locked loop is shown in Figure 5.1.

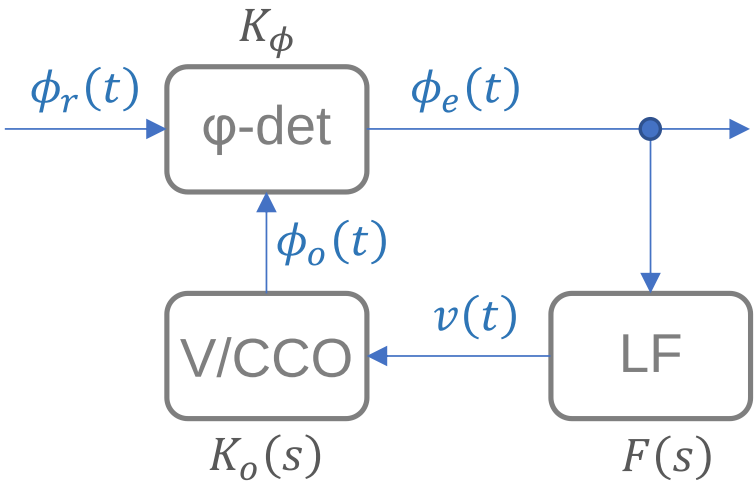

Figure 5.1. Block diagram of a standard reference tracking phase-locked-loop. The phase detector (*ϕ-det*) outputs the phase error between the input reference signal and a voltage/current controlled oscillator (V/CCO). The phase error is processed by a loop filter (LF) and fed back to the tunable oscillator. Under closed-loop operation, the tunable oscillator tracks the frequency and phase of the input reference signal.

In this reference tracking feedback system, the phase of a tunable oscillator (voltage or current controlled oscillator, V/CCO) is actively controlled to match the phase (and therefore by default, frequency) of the reference signal. A phase detector (ϕ-det) receives the reference and tunable oscillator signals and outputs the phase error (voltage proportional to the phase error). In this work, the phase detector will be assumed to be linear and represented by a frequency independent gain with units of [V/rad]. A loop filter (LF) with Laplace domain frequency response, *L(s)*, processes the phase error signal, generating the servo signal for the tunable oscillator. Under closed loop operation, this loop acts to tune the local oscillator to match the frequency and phase of the reference signal. Ideally, this would result in the LO perfectly tracking the reference with a phase error equal to zero. However, finite gain, bandwidth, and additional noise sources result in imperfect phase tracking. Measuring the phase error signal therefore yields a critical metric of phase lock

performance, the residual phase error. It is reported in this work by the power spectral density of residual phase fluctuations, $S_{\phi e}(f)$ [rad^2/Hz], and by the residual phase error variance, σ_ϕ^2 [rad^2], which can be calculated as the integral of $S_{\phi e}(f)$.

The phase locked loop can be extended to optical frequencies by using lasers as the reference and tunable oscillators, thus realizing an OPLL. A simplified block diagram of a standard OPLL is shown in Figure 5.2.

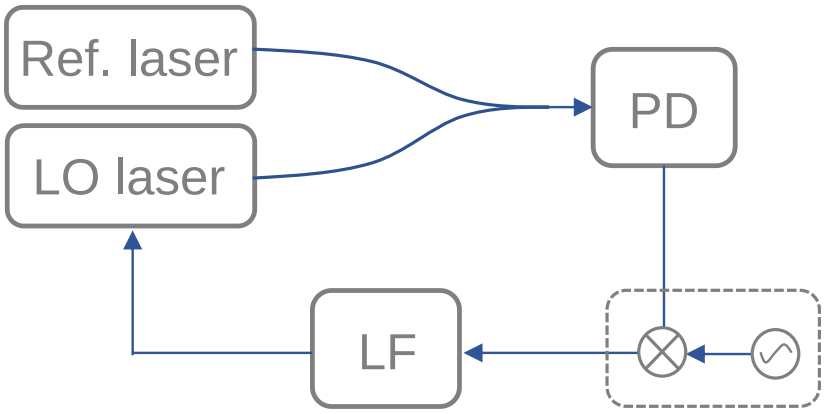

Figure 5.2. Diagram of an optical phase locked loop. Two lasers are optically mixed onto a photodiode to generate a phase error signal. For a homodyne loop, (lasers are phase locked at the same carrier frequency) the error signal is directly processed by the loop filter (LF). For a heterodyne phase lock, a frequency synthesizer is electrically mixed with the error signal (dotted subsystem).

In this configuration, a tunable local oscillator laser is optically mixed with a reference laser to measure the phase error between the sources. In a homodyne OPLL, the error signal is directly processed by the loop filter and fed back to the LO to close the loop. Under closed loop operation, the LO tracks the reference laser phase at the *same* optical frequency. For a heterodyne OPLL, the error signal is electrically mixed with a constant wave (CW) frequency reference (dotted box in Figure 5.2). This results in the loop acting to tune the LO such that the *beat note between the two lasers* is phase locked to the CW synthesizer signal. As such, the LO laser tracks the reference laser at a frequency and phase *offset* equal to that

of the CW source. This is commonly employed to enable precise control of laser frequency offsets by tuning the frequency of the CW source.

Signal propagation through an OPLL is shown in Figure 5.3. Laplace domain transfer functions are labeled for the loop filter (LF), LO laser, and phase detector (ϕ-det).

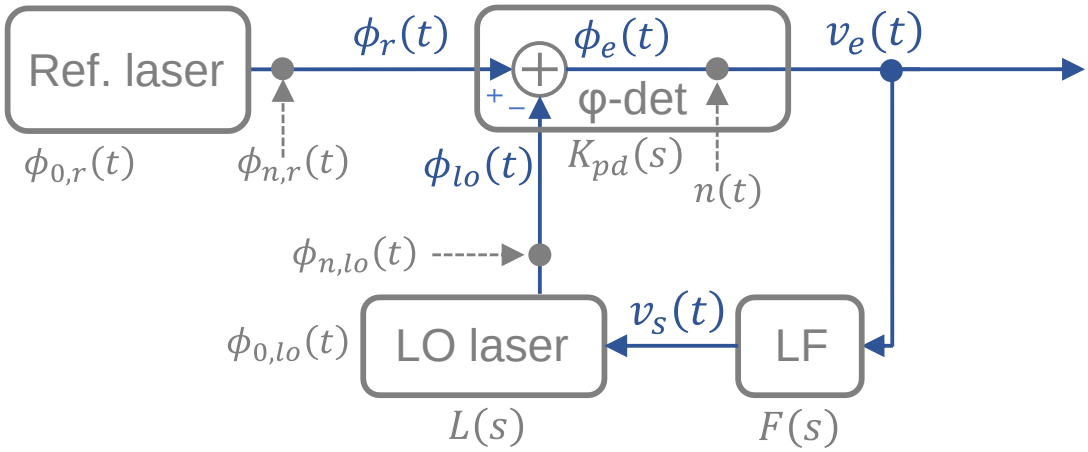

Figure 5.3. Optical phase locked loop showing phase propagation and explicitly labeled noises for reference and local oscillator lasers and phase detector (ϕ-det). Transfer functions are labeled for loop filter (LF), LO laser, and phase detector.

The reference and local oscillator are each given nominal phase and phase noise terms as by Eqs. 5.1 and 5.2

$$\phi_r(t) = \phi_{0,r}(t) + \phi_{n,r}(t) \qquad 5.1$$

$$\phi_{lo}(t) = \phi_{0,lo}(t) + \phi_{n,lo}(t) \qquad 5.2$$

The phase detector[11] performs a subtraction of the reference and LO phases [rad] scaled by a constant gain, K_{pd} [Volts/rad], yielding a phase error signal with units of [Volts] in Eq. 5.3

[11] Using a photodetector as a phase detector will have a sinusoidal output with phase error as the argument of the sin(·). The small angle criterion, $sin(\theta) \approx \theta$, enables linearization of the phase detector response and loop. This is acceptable for 'tight' phase locks (low phase error $\phi \approx 0$), such as those described in this work.

$$v_e(t) = K_{pd}(s) \cdot \phi_e(t) + n_{pd}(t) = K_{pd}[\phi_r(t) - \phi_{lo}(t)] + n_{pd}(t) \qquad 5.3$$

A noise term, $n_{pd}(t)$, is included to capture noise in the phase detection process (shot noise, photodetector noise, electronics noise in amplifier circuits). A photodetector bandwidth response modeled as a low-pass filter can be additionally included. The balanced photodetector employed in this work has 3 dB bandwidth ≫ loop bandwidth, and its frequency response is therefore modeled as a constant gain.

The error signal is processed by the loop filter with Laplace domain transfer function, $F(s)$ [V/V]. Shaping of this loop filter is the primary parameter space for which an engineer can control the behavior of the feedback system. Proper design is therefore critical for optimizing loop performance and achieving a stable loop that minimizes residual phase error. Additional information on PLL filter design (and extended to OPLLs) is given in [35]–[43], [79]–[82]. Common loop filters are proportional-integral-derivative (PID) or subsets [35]–[43], [79]–[82] due to the ease of design and implementation with simple analog electronics. The loop filter assumed in this work is a proportional-integral (PI) controller of the form (first order active filter) given in Eq. 5.4

$$F(s) = K_p \cdot \left(1 + \frac{T_i}{s}\right) \qquad 5.4$$

where K_p is a proportional gain and T_i is the frequency at which the controller switches from integral gain to proportional gain.

The output of the loop filter is the servo signal, $v_s(t)$ [V], which is fed to the frequency tunable LO, closing the OPLL. The LO laser transfer function, $L(s)$, contains a nominal frequency tuning gain, K_L [Hz/V], and a normalized frequency modulation (FM) response of

the laser. In practice a semiconductor laser will typically have a 3 dB tuning FM response on the order of several MHz, limited by a phase reversal due to competition between thermal and carrier tuning mechanisms [38], [82], [83]. If, however, the tuning mechanism for the OPLL is driven by, for example, a voltage controlled oscillator, the FM response may be as low as 10s or 100s of kHz and an accurate model will necessarily include this effect. In this work, the tuning frequency roll-off is empirically modeled as a unity gain low pass filter [38].

Applying standard linear time-invariant (LTI) analysis tools [42], [79], the open-loop transfer function for the system in Figure 5.3 is given in Eq. 5.5 as,

$$G(s) = K_{pd}F(s)L(s) \tag{5.5}$$

The corresponding closed-loop transfer function, *H(s)*, is then given by Eq. 5.6 as,

$$H(s) = \frac{G(s)}{1 + G(s)} \tag{5.6}$$

As previously mentioned, the effect of directly tuning a laser's *frequency* to engage a *phase* lock corresponds to an ideal integrator behavior with Laplace domain representation of *1/s*. The laser transfer function (assuming unity FM response over the <1 MHz loop bandwidths discussed in this work) can then be written as,

$$L(s) = K_L \cdot \frac{1}{s} \tag{5.7}$$

and substituted into the closed loop response to yield

$$H(s) = \frac{K_{pd}K_L\,F(s)}{s + K_{pd}K_L\,F(s)} \tag{5.8}$$

Finally, the power spectral density of the residual phase error, $S_{\phi,e}$ [rad^2/Hz], is given as Eq. 5.9 below,

$$\begin{aligned} S_{\phi,e} &= S_{\phi,r\otimes LO}\cdot\left|\frac{1}{1+G(s)}\right|^2 + S_n\cdot\left|\frac{\frac{G(s)}{K_{pd}}}{1+G(s)}\right|^2 \\ &= S_{\phi,r\otimes LO}\cdot|1-H(s)|^2 + \frac{S_n}{K_{pd}^2}\cdot|H(s)|^2 \end{aligned} \tag{5.9}$$

where $S_{\phi,r\otimes LO}$ [rad^2/Hz] is the combined power spectral density of phase fluctuations, assuming uncorrelated noise, for the reference and local oscillator lasers and S_n [V^2/Hz] is the voltage power spectral density of noise in the phase detection process (includes shot, photodetector, and electronics noise).

5.3 OPLL residual phase error for white-noise-only lasers

This section uses the relations developed in the previous section to model an OPLL employing two lasers with equal phase noise PSDs described purely by a fundamental linewidth. For such a laser, the frequency noise PSD is white with a constant value, h_0 [Hz^2/Hz] where $h_0 = \delta\nu/\pi$ and $\delta\nu$ is the fundamental linewidth in [Hz] [54]. The combined, uncorrelated phase noise for these two lasers is then given as Eq. 5.13

$$S_{\phi,r\otimes LO} = S_{\phi,r} + S_{\phi,LO} = 2\cdot\frac{S_f}{f^2} = 2\cdot\frac{h_0}{\pi f^2} \tag{5.10}$$

With the closed-loop transfer function and noises as defined previously, the free-running combined phase noise PSD of the two lasers and the closed-loop residual phase error PSD is plotted in Figure 5.4. The seven traces shown are for two lasers with equal fundamental linewidths, decade spaced from 1 Hz to 1 MHz (i.e., 1, 10, 100…).

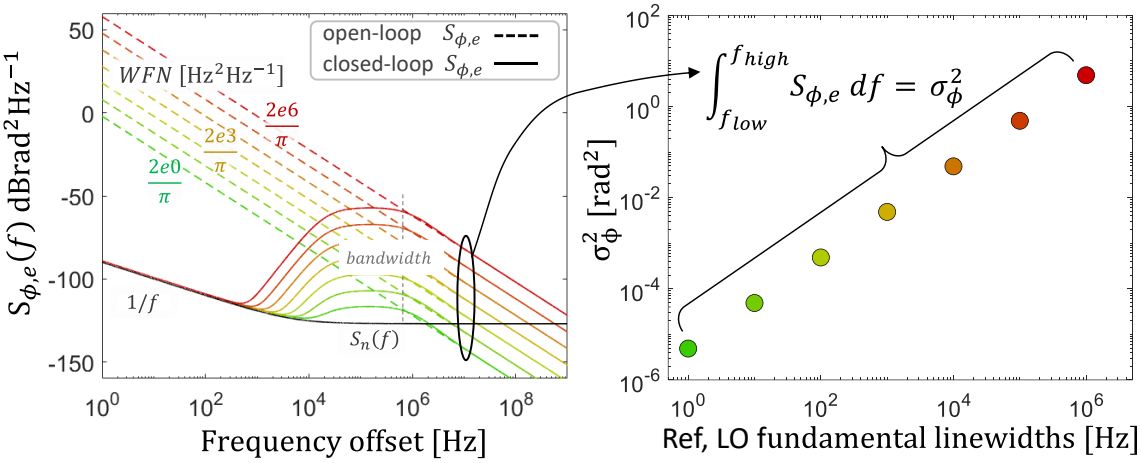

Figure 5.4. a) Open- and closed-loop total phase error power spectral densities for two lasers having equal fundamental linewidths of 1 Hz to 1 MHz. Integration of each of the closed-loop residual phase error PSDs yields the plotted residual phase error variances, σ_ϕ^2, in (b).

Integrating the closed-loop residual phase error PSDs yields the residual phase error variances plotted in Figure 5.4 (right). There is a clear benefit to using lasers with narrow FLWs, as the modeled residual phase error variance for two 1 Hz FLW lasers is less than $1x10^{-5}$ rad^2. Residual phase error variance increases with increasing FLW, up to just under $1x10^{-1}$ rad^2 for two 1 MHz FLW lasers. This disparity in achieved σ_ϕ^2 for these two cases is the difference between enabling high-order QAM transmission, and enabling only QPSK [84]. With respect to the linewidth narrowed sources developed in this thesis, this result demonstrates the benefit of SBS lasing to first reduce the FLW of a laser for use in an optical phase locked loop.

5.4 OPLL residual phase error for practical lasers

Next, OPLL performance in terms of achievable residual phase error variance is modeled for lasers having additional higher order noise (e.g., flicker frequency). The added noise strains the phase tracking ability of the OPLL within its loop bandwidth, resulting in untracked phase noise at closer-to-carrier frequencies and a larger residual phase error variance. In Figure 5.5 below, this is modeled for two lasers with the same FLWs as above, but now with the following additional defined frequency noises: h_0 = FLW/π; h_1 = 1x10^6·h_0; h_2 = 1x10^3·h_1.

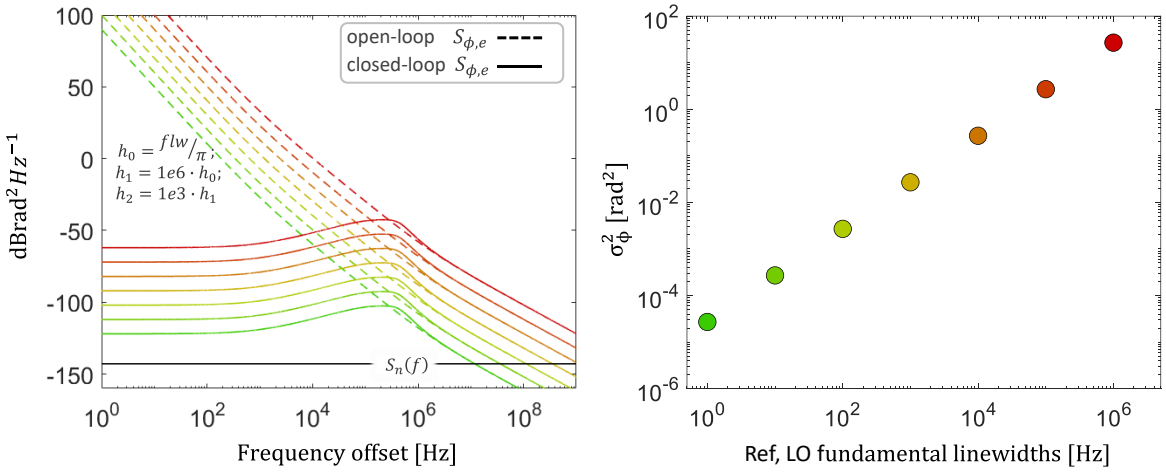

Figure 5.5. Open- and closed-loop residual phase error power spectral densities for two lasers (Reference and local oscillators: Ref/LO) having equal fundamental linewidths of 1 Hz to 1 MHz. Lasers also have higher order noise terms with relation between values shown in (left) of (a). Integration of each of the closed-loop residual phase error PSDs yields the plotted residual phase error variances, σ_ϕ^2, in (b).

The degradation in residual phase error is apparent, as none of the cases achieve performance limited by detector noise. The untracked phase discursions are dominated by laser noise. The plot of residual phase error variances shows an increase of nearly an order of magnitude for each case when compared to the plots in Figure 5.4, where each laser noise was only a governed by its fundamental linewidth. It should also be noted that the plotted

residual phase errors share the same linear trend (though shifted up by a ~constant value) versus fundamental linewidths as shown in the white-noise-only lasers case in Figure 5.4. This further highlights the challenge of using large fundamental linewidth lasers in an OPLL, especially with the goal of using only low bandwidth (<MHz) feedback loops for low energy phase locking. Any laser phase noise occurring outside of the feedback loop cannot be tracked or suppressed - this region of phase noise, typically occurring beyond the range of environmental and technical noise contributions, is therefore set by the fundamental linewidth.

In addition to the primary goal of reducing residual phase error, cavity stabilization has secondary benefits for lasers used in an optical phase lock. By first anchoring each of the laser carriers independently, drift is greatly reduced which is a direct benefit for loop robustness in terms of remaining with the hold-in range of the phase lock.

Within the context of this thesis, these results motivate the cavity stabilization approach in combination with SBS lasing for the spectrally pure lasers developed in Chapter 4. By first reducing the close-to-carrier frequency noise of each laser, the demands on the optical phase lock are relaxed. This approach is the defining characteristic of the optical-frequency-stabilized phase locked loop OFS-PLL.

5.5 The optical-frequency-stabilized phase locked loop

Two stable SBS lasers connected over optical fiber form the optical-frequency-stabilized phase locked loop (OFS-PLL). Leveraging the spectral purity and stability of the optical carriers, the OFS-PLL achieves an ultra-low residual phase error variance requiring only low bandwidth loops and electronics. The experimental schematic is shown in Figure 5.6 [60].

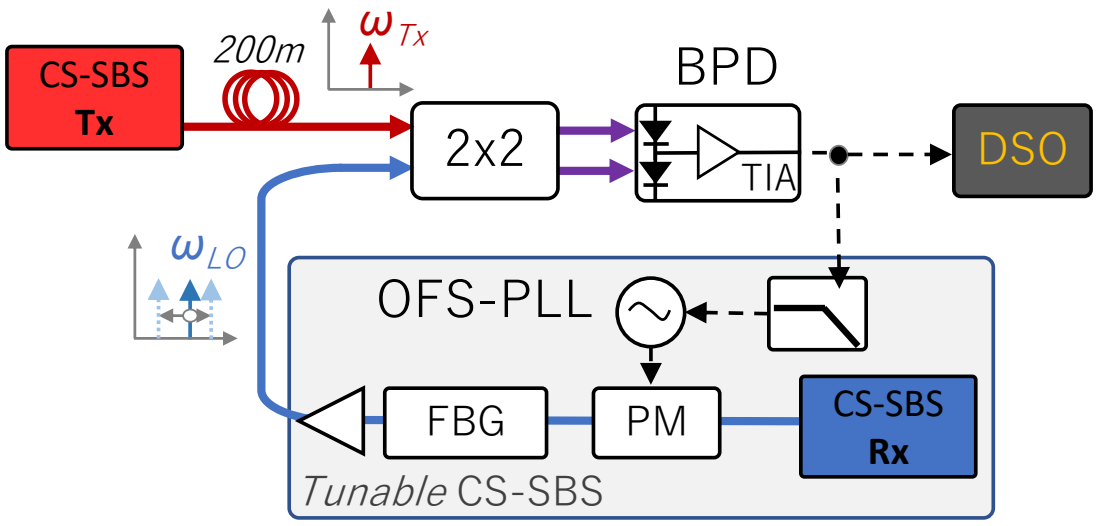

Figure 5.6. Experimental schematic of the optical-frequency-stabilized phase locked loop (OFS-PLL). A CS-SBS laser transmits (Tx) a linewidth-narrowed, stable optical carrier over fiber. A receiver (Rx) stable laser is made tunable by optically filtering (via a fiber Bragg grating, FBG) a phase modulated (PM) sideband driven by a voltage controlled oscillator (VCO) with a control signal derived from a BPD (bandwidth, 45 MHz) with built-in transimpedance amplifier (TIA) as an optical phase detector. A digital storage oscilloscope (DSO) measures the phase error.

In this configuration, tunability of the receiver-side CS-SBS laser was achieved by filtering an optically phase modulated (PM) single sideband with a fiber Bragg grating (FBG). By driving the phase modulator with a voltage controlled oscillator, this results in a frequency controllable local oscillator (LO) that inherits the spectral purity and stability of the stable SBS lasers. The optical phase detector was realized by optically heterodyning the transmit and LO carriers using a two-by-two fiber optic combiner and a balanced photodetector (BPD) with built-in transimpedance amplifier (TIA). The output of the phase detector is given by Eq. 5.11 [35]

$$V_{\phi e}(t) = GR\sqrt{P_{tx}P_{LO}}\cos\left(\phi_{tx}(t) - \phi_{LO}(t)\right) + n(t) \qquad 5.11$$

where R is the responsivity of the balanced photodetector in [A/W], G is the transimpedance gain in [V/A], and P_{tx}, ϕ_{tx}, P_{LO}, and ϕ_{LO} are the optical powers and phases of the transmit and

LO lasers, respectively. The combined shot, detector, and electronics noise are captured in the *n(t)* term [35] as previously discussed in Section 5.2. The transmit and LO laser phase terms in Eq. 5.11 include the nominal frequency increment of optical phase, an arbitrary nominal phase, and the phase noise of the free running lasers as given by Eq. 5.12

$$\phi(t) = \omega t + \phi_0 + \phi_n \tag{5.12}$$

Substituting 5.12 into 5.11, the output of the phase detector under open-loop operation is found to be proportional to the frequency difference between Tx and LO lasers, with a nominal initial phase offset (which does not affect the time dependence of phase error and is removed), and with phase noise contributions of both lasers as seen in Eq. 5.13

$$V_{\phi e,open\ loop} \propto \cos\left(\omega_{tx}(t) - \omega_{LO}(t) + \phi_{n,tx}(t) - \phi_{n,LO}(t)\right) + n(t) \tag{5.13}$$

The open-loop phase error signal takes the form of a sinusoid oscillating at the frequency difference between the two laser carriers, perturbed by the combined phase noise contributions of each independent laser. For the lasers developed in this work, the open-loop error signal is observed having only very, low-frequency phase perturbations as shown in Figure 5.7 under open-loop operation (i.e., 'free-running' heterodyne of the two stable lasers – this is equivalent to the heterodyne EFD baseband noise presented in Section 4.4, but at the beat note carrier frequency).

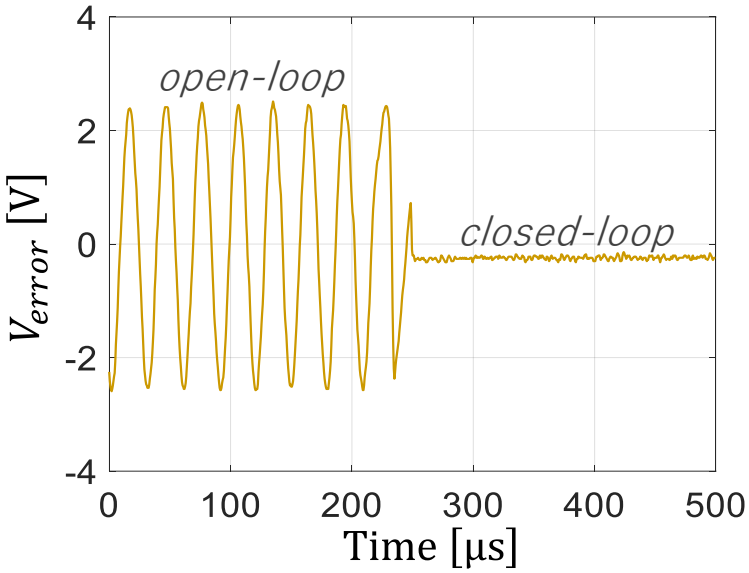

Figure 5.7. Phase error signal showing open- to closed-loop operation of the optical-frequency-stabilized phase locked loop (OFS-PLL). The open loop error signal resembles a pure sinusoid, perturbed by the minor phase noise contributions of both stable lasers.

This error signal pictorially demonstrates the benefit of spectrally pure, stable lasers for optical phase locks. Closing the loop to phase synchronize these two sources equates to driving the phase error signal to zero by active feedback frequency tuning of the local oscillator. After matching the frequencies of each laser, the remaining phase error is simply the combined phase noise of both sources. Successful lock acquisition is observed by the zero-fringe-slip transition from open- to closed-loop operation with the error signal driven near zero, with lock-acquisition range measured to be ~ 800 kHz. With only low mutual phase noise that occurs at low frequencies (longer timescales), the loop action necessary to correct for the phase error is minimal, requiring only low bandwidth feedback electronics.

The digitally sampled closed-loop residual phase error (time trace of Figure 5.7) is characterized in the frequency domain as the residual phase error PSD, $S_{\phi,e}$ [rad^2/Hz], plotted in Figure 5.8 below.

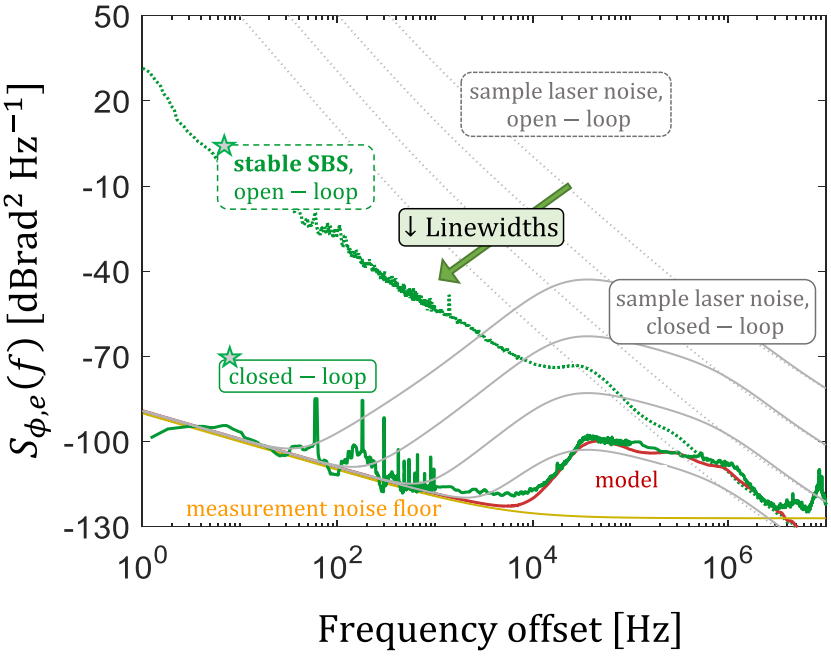

Figure 5.8. Open- (green dashed) and closed-loop (green solid) residual phase error PSD of the optical-frequency-stabilized phase locked loop. Reference lines showing combined phase noise of two lasers with white noise fundamental linewidths between 1 Hz and 1 MHz, (and higher order power law noise) in open- (grey dashed) and modeled closed-loop (grey solid) operation. A model (red) closed-loop prediction of residual phase error using the Tx-Rx stable SBS heterodyne *measured* phase noise as the input noise verifies loop behavior.

The plotted residual phase error PSD provides the most detailed view to characterize OFS-PLL performance. The 'shoulders' at ~ 50 kHz and ~1 MHz, are servo bumps from the cavity stabilization stages (and can be matched with the previously shown open-loop Tx/Rx heterodyne FN traces presented in Section 4.4, Figure 4.11). Noise spurs at multiples of ~ 20 kHz were found to be the result of a noisy power supply perturbing the pump laser for the Rx SBS laser. Noise spurs observed at integer multiples of 60 Hz are the result of power line noise leakage. Higher frequencies noise spurs are the result of intermixing products of PDH phase modulation tones, unsuppressed phase modulated sidebands for the tunable LO, and unsuppressed reflections of pump lasers. Table 5.2 below shows residual phase error

variances calucated by integrating over numerous sub-spans of the phase error PSD, to show the effect of observation interval on phase error.

Table 5.2. Integration of phase noise power spectral density over various frequency sub-spans.

$$\sigma_\phi^2\,[rad^2] = \int_{f_{start}}^{f_{stop}} S_\phi(f)\,df$$

f_{start}	f_{stop}	$\sigma_\phi^2\ (rad^2)$	$\sigma_\phi\ (deg)$
1 Hz	10 kHz	3.4E-7	0.03
1 Hz	100 kHz	1.0E-5	0.18
1 Hz	1 MHz	4.0E-5	0.36
1 Hz	10 MHz	1.9E-4	0.79
1 Hz	45 MHz	3.3E-4	1.04

Residual phase error variance was measured for various received optical powers between -14 dBm and -44 dBm over 20 minute timescales to demonstrate long term operation, as shown in Figure 5.9.

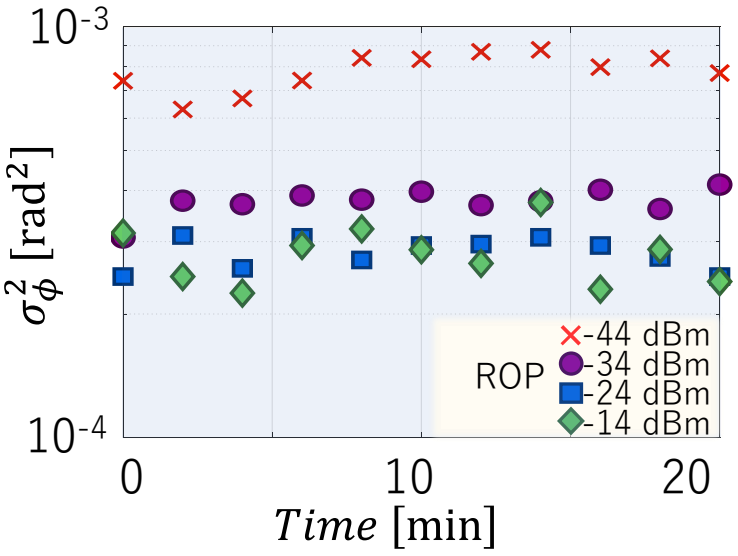

Figure 5.9. Residual phase error variance for several received optical powers (ROP) over 20 minute timescales.

For received optical powers down to as low as -34 dBm, the residual phase error variance was measured to be near its lowest value of ~$3x10^{-4}$ rad^2. At -44 dBm, the value is observed to increase slightly to ~ $8x10^{-4}$ rad^2.

To predict the performance of the OFS-PLL operating over longer spans of fiber, fiber noise was simulated[12] to estimate the length of fiber at which fundamental fiber noise would surpass phase noise of the SBS lasers and therefore set the bounds on phase lock performance. This is estimated to occur for fiber spans longer than ~300 km.

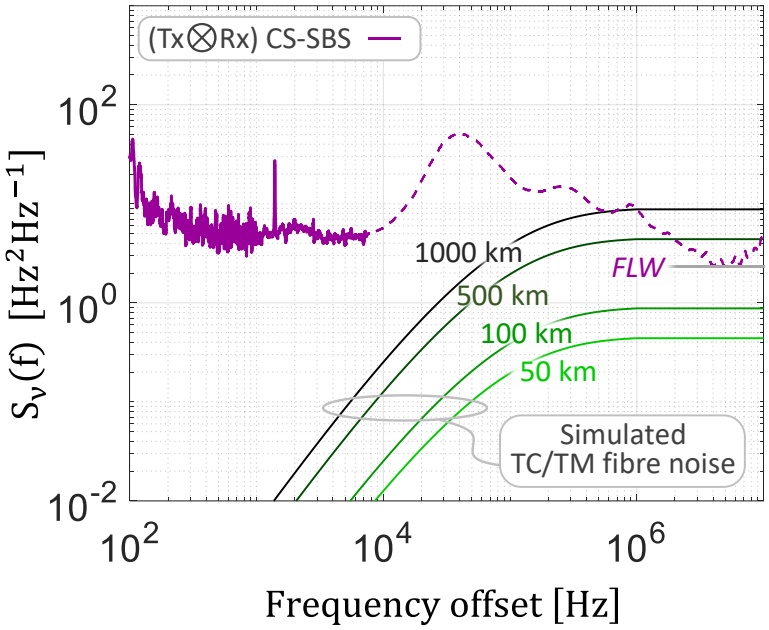

Figure 5.10. Modeled fiber noise from thermo-conductive and thermo-mechanical sources [85], [86]

The approach and 'return on efforts made' in realizing chip-scale spectrally pure sources for high performance optical phase synchronization can be compared to alternatives in terms of laser linewidths, loop bandwidths, power consumption, residual phase error variance, and potential for use in higher order coherent modulation as is done in Table 5.3.

[12] Simulations of fiber thermal noise by J. H. Dallyn are gratefully acknowledged [60]

Table 5.3. Summary comparison (left) of standard approaches to optical phase synchronization for optical phase locked loops (OPLLs, [36]–[38], [80], [87]), digital signal processing (DSP, [88]–[94]), and for the approach presented in this work and its future projection to integrated photonics. *substitution of components already demonstrated in literature, e.g., SiPh single sideband modulators [77]. Power breakdown of the optical phase synchronization approach in this work (right)

	OPLLs	DSP	Spectrally pure phase synchronization		
			This work	With existing substitutions*	Future
Laser LW	1-10 MHz	1-10 MHz	1 Hz FLW, 30 Hz ILW	1 Hz FLW, 30 Hz ILW	<1 Hz FLW, <30 Hz ILW
Bandwidth	1 MHz ~ 1 GHz	high	< 1 MHz	< 1 MHz	100s kHz
σ_ϕ^2 **rad²**	0.1 – 0.01	very good	$3x10^{-4}$	$3x10^{-4}$	$1x10^{-5}$
Power [W]	~100s mW - 2 W	~5-10 W	~10 W	~1.5 W	~500 mW
Modulation Format	QPSK	M-QAM	256-QAM	256-QAM	512-QAM

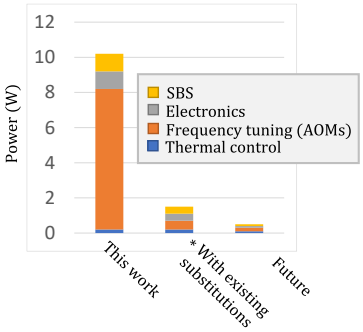

As shown, OPLLs [36] that employ standard integrated semiconductor lasers with linewidths on the order of several MHz demand high bandwidth feedback loops and achieve modest performance in terms of residual phase error variance of ~0.1-0.01 rad^2. The power consumed by these systems is on the order of several hundred milliwatts up to several Watts. They have been demonstrated operating as carrier phase recovery units for QPSK links [80], [95]. Digital signal processors currently employed in long-haul coherent links achieve good carrier phase recovery thus enabling higher order QAM transmission but consume a great deal of power (as much as tens of Watts) [88]–[94], [96]. In this work, the current form of the table-scale proof-of-concept demonstration using fiber-interconnected discrete components is estimated to consume on the order of 10 W, as summarized in Table 5.3 (right). The major power consumers for the current version of this system are the acousto-optic modulators that consume >3 Watts per laser stabilization system. As such, replacing these components with low power alternatives [77] will have great impact on energy efficiency of this approach.

5.6 Discussion

The optical-frequency-stabilized phase locked loop discussed here demonstrates a proof-of-concept for record low residual phase error variance of $3x10^{-4}$ rad^2 using only low bandwidth, low power feedback electronics. Additional design considerations can be developed to realize even more robust loop, such as including an outer frequency-pull-in stage to the OFS-PLL to greatly extend the lock capture range beyond the current ~ 800 kHz. Though the numerous sub-systems were implemented as fiber-connected discrete devices in these initial demonstrations, each of the required functionalities can be integrated as photonic devices in future generations. In particular, the chip-scale bulk reference cavities can be replaced by waveguide integrated device [26], [58], [59]. The tunable LO realized by optical single sideband modulation has been successfully demonstrated in silicon photonic platforms [77], [97] consuming only several hundred mWs of power. These devices can also be used in place of the acousto-optic modulators, to realize the full cavity stable SBS laser on a chip. Additional heterogenous integration of pump lasers [32], [61], [76] can further miniaturize the OFS-PLL footprint. Finally, the low bandwidth loop electronics can be co-packaged in mW-tier bipolar complementary metal-oxide semiconductor (Bi-CMOS) platforms for a truly miniaturized, single chipset with low total power consumption.

6 High order coherent communications application demonstration

6.1 Spectrally pure lasers for energy efficient communications

When an internet user makes a search on the web, streams a movie to a smart TV, or uploads an image to a social media platform, data housed in a distant 'farm' of digital storage is accessed, modified, and returned in the blink of an eye. These massive data storage locations, or *datacenters*, contain endless rows of hard drives that are continuously accessed and modified. This constant transmission of data amounts to a significant power demand, with datacenters accounting for 1.1-1.4% of all global electricity consumption [98]. A nearly 30% annual growth rate of internet traffic estimated to reach *5 Zettabytes per year* by 2022 [99], combined with datacenter overhead estimations that *'for every bit of information that travels a network to an end user, an additional 5 bits of data are transported within a datacenter* [100],' equates to an immense concentration of energy consumers within datacenter interconnects (DCIs).

To address these concerns of power consumption within datacenters, the photonics community, in particular, has played an increasingly important role due to the higher data capacities, longer reach, and lower power consumption of optical fiber technologies yielding favor over their electrical counterparts. Today for example, when a user makes a web query, at some point in the journey between their device and the physical location at which their data exists, a laser and myriad complex photonic integrated circuits (PICs) are involved. These photonic devices manipulate light in a high speed, orchestrated dance, sending signals

of light over optical fiber and enabling the communications links necessary for the world to access its data on demand. These actions still come at a measurable cost in terms of the energy consumed by photonic technologies, however, motivating a great deal of today's research in energy efficient optical communications. Rising to meet these concerns offers an opportunity for major impact on our world, as energy use and green technologies are ever more existentially important.

One solution to these growing bandwidth demands is to bring spectrally efficient, high order modulation formats to short reach links within the DCI. However, existing coherent architectures, while well-suited for longer (10s-100s of km) links, currently rely on digital signal processing (DSP) for data recovery operations and may be too power intensive to find a role in future DCIs. This has motivated promising DSP-free approaches to coherent communications, such those employing electrical/optical phase locked loops (E/OPLLs) for carrier recovery and others that employ pilot-tone aided transmission. However, standard E/OPLLs that employ large linewidth (>100s kHz – though plenty narrow for certain applications e.g., in atomic spectroscopy, integrating this phase noise over 10s of GHz common in communications has a large penalty) commercial semiconductor lasers demand high-bandwidth, high-power feedback loops and typically achieve phase synchronization performance not suitable for higher order formats. Carrier phase recovery using low power electronics with performance suitable for higher order coherent quadrature-amplitude-modulation (QAM) in DCIs has remained a challenge.

This chapter demonstrates the optical-frequency-stabilized phase locked loop in a high-order quadrature-amplitude modulated (QAM) link. The low residual phase error achieved by the spectrally pure optical phase synchronization approach enables a new architecture for

low energy coherent communications, termed the FREquency Stabilized Coherent Optical link (FRESCO)[28]–[30], [60]. A coherent link operating in multiple higher order and high capacity configurations, up to 56 GBd and 64-QAM is demonstrated.

Section 6.2 discussed optical communications and approaches for spectrally efficient modulation formats. Section 6.3 relates residual phase error variance to high-order QAM performance. This is done by assuming phase-noise-limited operation (i.e. link performance and BER are dominated by phase error) to isolate the impact of employing narrow linewidth lasers in a coherent link. More rigorous approaches to analyzing coherent link performance that include additional noise sources such as optical-signal-to-noise ratio (OSNR) and other channel impairments can be found in literature [84], [87], [101]–[103] and are not the focus of this work.

In Section 6.4, the coherent modulation link testbed is presented and briefly discussed. This includes the electrical front- and back-ends (e.g. digital-to-analog and analog-digital convertors (DACs/ADCs) in the form of commercial arbitrary waveform generators (AWGs) and coherent optical modulation analyzer (OMA) systems), electrical-optical coherent data modulators, fiber interconnections, and optical amplifiers.

Section 6.5 demonstrates the FRESCO link operating at high modulation orders (up to 256-QAM at 10 GBd) to highlight spectral efficiency, and high capacity (64-QAM at 56 GBd) to highlight suitability in future, spectrally efficient data center interconnects.

6.2 Optical communications and the datacenter interconnect

With the ubiquity of cost efficient, integrated lasers and low loss fiber optic cables, optical communications has been an enabling technology for networking the globe [104],

[105]. These efforts were initially motivated by the appealing properties of using light as a signal carrier, most notably for its high information capacity and ultra-low propagation loss through optical fiber that enabled long reach channels exceeding 100s and 1000s of kms. Coherent communications, enabled by the advent of DSP for optical signal recovery (notably, enabling digital *carrier phase recovery* to compensate the unstable optical phase of large linewidth standard commercial lasers [89], [101], [106]), played a particularly important role in long haul fiber optic links to form the backbone of intercontinental communications via undersea fiber optic cables, connecting the world at large. In the mid-2000s, fiber optics technologies entered the datacenter interconnect [107], [108] providing 1-10 Gigabit-per-second (Gbps) per single carrier connectivity using direct detection modulation formats. With increasing bandwidth demands, these technologies continued to develop to support data rates of 40 Gbps and soon 100 Gbps by 2014 [109], [110]. Today, rates of 400 Gbps are being developed and standardized [111], [112]. However, for future high-capacity fiber links in the DCI, direct detect formats may soon hit a bottleneck in terms of achievable data capacities, warranting the use of more spectrally efficient coherent formats. Yet, while well suited for long haul links, the DSPs currently required for data recovery for coherent transmission may be too power intensive to fit this role, thus motivating DSP-free coherent technologies [90], [113].

Optical modulation formats and spectral efficiency

Using a lightwave as the signal for carrying information supports digitally encoded bits (1s and 0s) in several ways, each with its advantages and disadvantages. Most easily understood are the methods categorized as *intensity* modulation or ‘direct-detection’: modulating the amplitude (power) of the lightwave to represent encoded information, e.g.,

an ‘on’ state can correspond to a ‘1’ and an ‘off’ state to a ‘0’ and is appropriately termed ‘on-off keying.’ We can call the time slots for each bit the symbol period, T_s, and note that the bit rate for this first method that supports one bit per time slot is $1/T_s$.

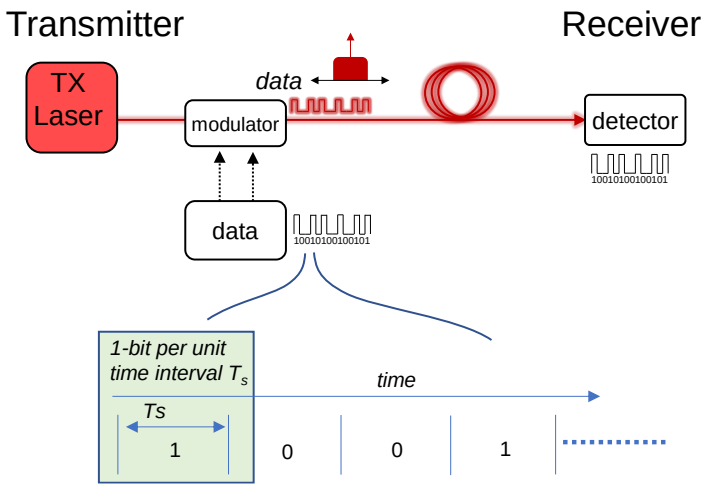

Figure 6.1. Optical communications over a fiber link encoding 1-bit per symbol (on-off keying).

Naively, to increase the data throughput using this encoding format, we can increase the speed that we switch between 1s and 0s, and shorten T_s. This approach reaches limits due to bandwidth limitations of the electronics that support these links. Yet the demand for ever faster data rates persists, thus motivating the use of more sophisticated data encoding methods.

This method of on-off keying uses only one degree of freedom of the lightwave, its amplitude, to support the channel. However, being an electromagnetic wave, light has additional degrees of freedom, such as *phase*, *polarization*, and *spatial modes*, that can be independently encoded with information to increase data throughput [104]. Modulation approaches that use optical phase are given a class aptly named *coherent* modulation [101], [104], [106]. Similar to the intensity modulated scheme described above, a sample scheme for encoding bits to optical phase could be a ‘1’ state represented by an optical phase of

180°, and a ‘0’ state being 0°. This format is named *binary phase shift keying* (BPSK). This approach requires that the data signal optical phase be recovered at the receiver, which is achieved by mixing with a local oscillator (LO) laser [35], [101], [106], [114].

Increasing the data throughput by encoding more information per symbol period can also be achieved by discretizing the levels of amplitude modulation or phase modulation. These schemes are termed *M*-PAM (order = *M* pulse amplitude modulation) and *M*-PSK for order = *M* phase shift keying and result in higher spectral efficiency (SE), or greater information transmitted over a given channel bandwidth.

Channel capacity can be further increased by encoding data over multiple degrees of freedom simultaneously, using multiple discrete levels in modulating both amplitude and phase. This coherent modulation approach is termed *quadrature-amplitude-modulation* (QAM) [101], [103], [106] and is shown in a link schematic in Figure 6.2.

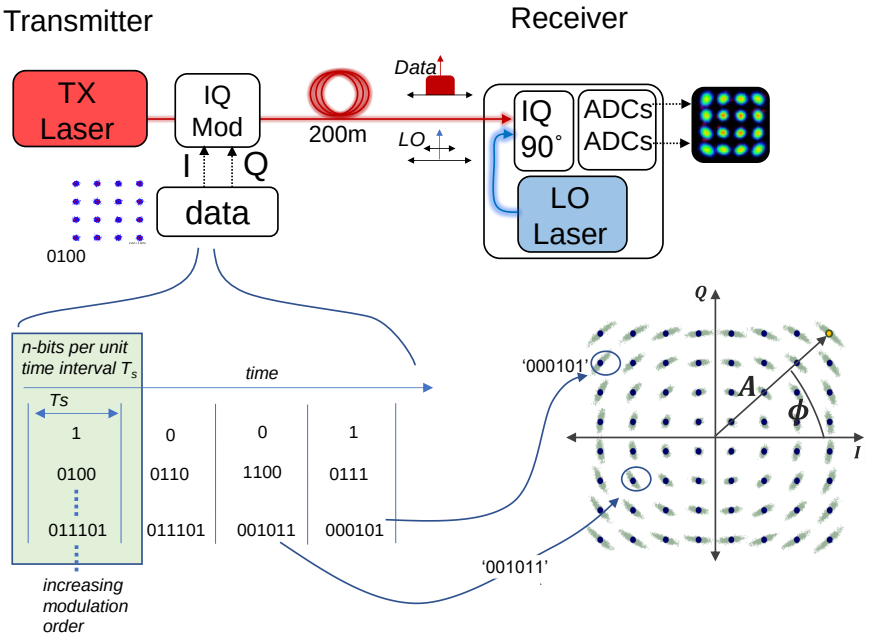

Figure 6.2. Coherent optical link schematic with local oscillator laser on the receiver side to demodulate the data signal and recover carrier phase. Increasing the modulation order encodes more bits to a single symbol (per time slot, T_s). A sample 64-QAM constellation is shown with 6-bits per symbol.

A comparison of the mentioned modulation formats showing symbol locations on a real ('in-phase', *I*), and imaginary ('quadrature', *Q*) axes, as well as the corresponding number of bits per symbol are shown in Figure 6.3.

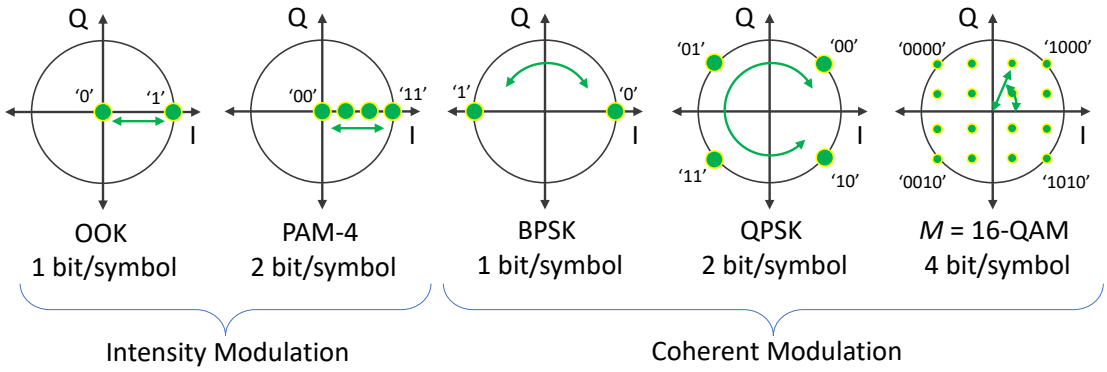

Figure 6.3. Constellations of on-off keying (OOK), pulse amplitude modulation (PAM), binary phase shift keying (BPSK), quadrature phase shift keying (QPSK), and quadrature amplitude modulation with modulation order $M = 16$.

Higher order QAM formats can achieve higher bits/symbol as shown by the sample M = 16-QAM constellation with 4 bits/symbol. QAM formats can be pushed to higher order M [84], [102], [115], achieving higher spectral efficiencies at the cost of system complexity and more stringent noise requirements (though not without bound, as optical nonlinearities set limits for increasing optical power when pushing for the higher signal-noise-ratios needed for higher order formats [116]). In the linear regime, Figure 6.4 below shows that higher order modulation formats increase spectral efficiency and approach the linear Shannon limit [101].

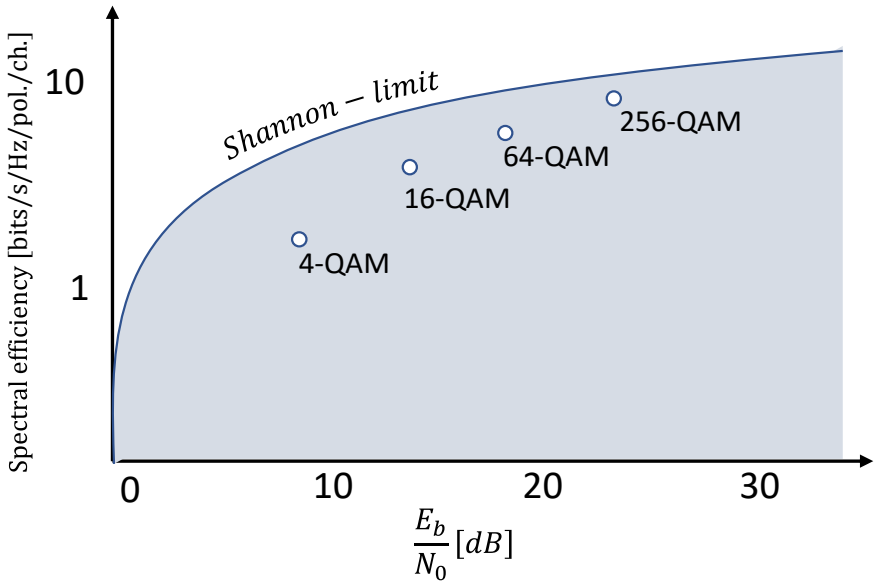

Figure 6.4. Spectral efficiencies of higher order quadrature-amplitude modulation (QAM) formats as a function of signal-to-noise ratio (SNR) per bit [101]. Higher order modulation formats approach the Shannon limit (figure adapted from [101]).

However, numerous additional challenges are faced when moving to higher order modulation formats. The increased signal-noise-ratios required for higher order QAM cannot be directly achieved by simply increasing optical power in the transmitted signal due to the onset of optical nonlinearities [104], [116]. These phenomena result in SNR degradation as optical powers and channel lengths are increased and set upper bounds on spectral efficiency gains when considering higher order formats. Detailed discussion and models of these effects on spectral efficiency are provided in Ref [116]. These impairments are not investigated in this work, though are noted as considerations for future work.

An additional challenge when increasing QAM modulation order is the increased requirements on residual phase error [84], [102], [115]. This is the key challenge addressed in this work and motivates the spectrally pure optical phase synchronization approach previously discussed for use in high order coherent communications.

Digital signal processing and its alternatives

The large linewidths and corresponding high phase noise associated with commercial semiconductor lasers used for communications initially presented issues in achieving optical phase synchronization necessary to recover phase-encoded data. Digital signal processing techniques were developed as a solution. By digitally sampling the optically downconverted data signal at rates commensurate with the symbol rate, the signal waveform can be recovered with sufficient fidelity to reconstruct the transmitted signal. High-speed mathematical operations can then be performed in digital circuitry to correct for channel impairments such as chromatic dispersion, polarization rotation, optical frequency offset error, *carrier phase error* between data and local oscillator lasers, and more [89], [91]–[93], [117]. DSP approaches require digital sampling of the waveform by use of high speed analog-to-digital convertors (ADCs) [91], [118] which can present a concern due to their high power consumption that scales unfavorably with data rate and bit depth [88]. Further, with higher modulation orders, higher bit depth ADCs are required [118] thus imposing high power consumption penalties for links with greater spectral efficiencies. Combined with the high speeds of the operations required, as data rates and channel densities increase, the power consumption of DSP can be on the order of tens of Watts per channel [88], limiting their use to outside of the high traffic density environments of the modern data center interconnect. Transitioning to ever-smaller complementary metal-oxide semiconductor (CMOS) nodes for reduced power consumption [94] in DSPs and other digital circuitry may not directly provide a suitably aggressive solution.

With the power consumption of DSPs being a primary concern for coherent links, DSP-free and DSP-‘lite’ alternatives are an area of active research. For example, recent

demonstrations of DSP-free carrier recovery using simple analog circuitry was demonstrated with an estimated power consumption of 4 Watts [90]. However, the phase error recovery operations are limited in use to low order coherent formats (QPSK). Other promising approaches have employed pilot-tone-aided transmission using duplex fiber to simplify the recovery of optical phase [96]. Transmission of high order modulation formats without the overhead of using of pilot tones, however, has remained a challenge. These mentioned approaches employ phase recovery through the use electrical and optical phase locked loops. They represent a significant area of recent and ongoing research, and while previously somewhat independent of spectrally efficient communications, they have seen recent renewed interest in optical links as an alternative to DSPs [80], [95], [119].

6.3 Residual phase error and high-order QAM performance

This section discusses the impact of phase noise on the performance of a coherent link. A simple approach is taken to relate residual phase error variance to a bit-error-rate illustrating, the impact of employing spectrally pure lasers in high order QAM transmission. For a phase noise limited link, residual phase error variance thresholds are calculated for several modulation orders for a given BER. The BERs chosen for this exercise satisfy one of several forward error correction (FEC) thresholds [63], [64], showing applicability of the FRESCO approach to standardized requirements for commercial coherent transceivers. The low residual phase error variance result for the OFS-PLL presented previously is estimated to be suitable for coherent modulation up to 256-QAM.

A constellation for 64-QAM is shown in Figure 6.5. Using an approach similar to Refs. [84], [102] where extremely high order modulation was demonstrated, the smallest angular

separation between nearest neighbors, ϕ_{nn}, is first calculated. The smallest angular separation occurs for symbols at the outermost corners of the square constellation.

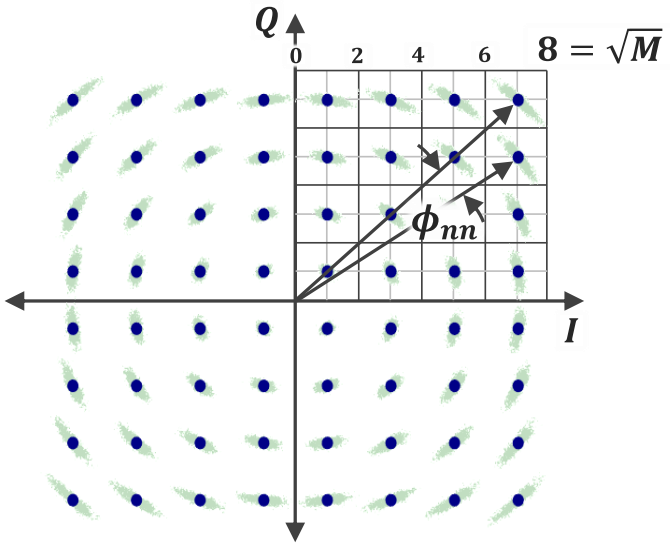

Figure 6.5. Example constellation (64-QAM) showing phase noise limited operation. A grid with numeric labels for the calculation of nearest-neighbor minimum angular separation, ϕ_{nn}, is presented.

Using the coordinate labels in Figure 6.5, the *[I, Q]* indices of the outermost symbol is *[7, 7]*, and its nearest neighbor is *[7, 5]*. In a form generalized with respect to modulation order, M, for a square M-QAM constellation (i.e. symbol locations fill a full square grid, e.g. 16-, 64-QAM, but not 32-QAM, 128-QAM where outermost symbols are not at the square corners, though a similar relation can be found), these symbol locations can be given as vectors with lengths according to Eqs. 6.1 and 6.2,

$$IDX_{outermost} = \left[\sqrt{M} - 1, \sqrt{M} - 1\right] \quad 6.1$$

$$IDX_{outer-1} = \left[\sqrt{M} - 1, \sqrt{M} - 3\right] \quad 6.2$$

Using the simple dot product identity relating the angle, θ, between two vectors, u and v shown in Eq. 6.3,

$$\boldsymbol{u} \cdot \boldsymbol{v} = \left||u|\right| \left||v|\right| \cos(\theta) \qquad 6.3$$

the smallest angular separation for the square QAM constellations can be calculated and is summarized in Table 6.1.

Table 6.1. Summary of minimum angular separation between nearest neighbor symbols for *M*= 16-, 64-, 256-, and 1024-QAM formats

M-QAM	ϕ_{nn}°	ϕ_{nn} rad
16	26.6	0.46
64	9.46	0.17
256	4.09	7.13e-2
1024	1.91	3.33e-2

As an estimation for phase error thresholds for a given QAM order, these values for minimum angular separations can be directly used as approximate bounds as is done in Refs. [84], [102]. This does not statistically relate a given phase error to a BER, however, as will be done now to further extend this approximation of low residual phase error thresholds to high order QAM links and commercial FEC thresholds [112], [120]. Several assumptions are made for this approximation:

1) Link performance is limited by phase noise only. Approximation does not include other common noise sources such as OSNR or other channel impairments (rigorous models have been presented in literature, such as in Refs. [103], [106], [116]
2) Phase error distribution is Gaussian and zero mean
3) Phase error is small, justifying use of a standard Gaussian distribution. Since the phase error is angularly spread, a more accurate model would employ a wrapped normal, or *Tikhonov*, distribution as is done in Ref. [103].

4) Errors for only the outermost symbol are considered, as these locations are most sensitive to phase error (minimum nearest neighbor angular separation)

Standard tools for Gaussian statistics can be used to relate a given BER to the phase error variance required for meeting that error probability threshold. Figure 6.6 illustrates a normal distribution of phase noise with standard deviation, σ_ϕ, centered about one of the outermost symbols of a 64-QAM constellation.

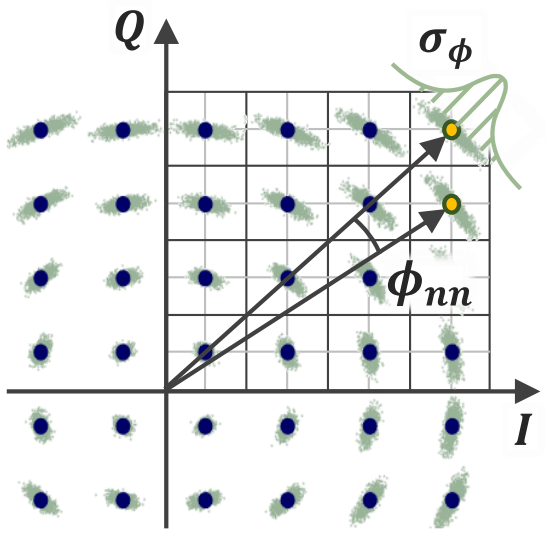

Figure 6.6. Phase noise is assumed to be Gaussian and centered around each constellation point

Using the calculated minimum angular separations, ϕ_{nn}, as bounds on a standard normal distribution, calculating the Z-score relates probability of error to phase error variance as shown in Eq. 6.4,

$$P\left(Z > \frac{x}{\sigma}\right) = BER;\ \sigma^2_{\phi,req.} = \left(\frac{\phi_{nn}}{Z}\right)^2 \qquad 6.4$$

where Z is calculated for a given BER. Substituting values of ϕ_{nn} for each modulation order M yields the required phase error variance, $\sigma^2_{\phi,req.}$. Using this approach, the required

residual phase error variances for modulation orders *M* = 16-, 64-, 256-, and 1024-QAM for BER values between $1x10^{-1}$ and $1x10^{-6}$ are plotted in Figure 6.7.

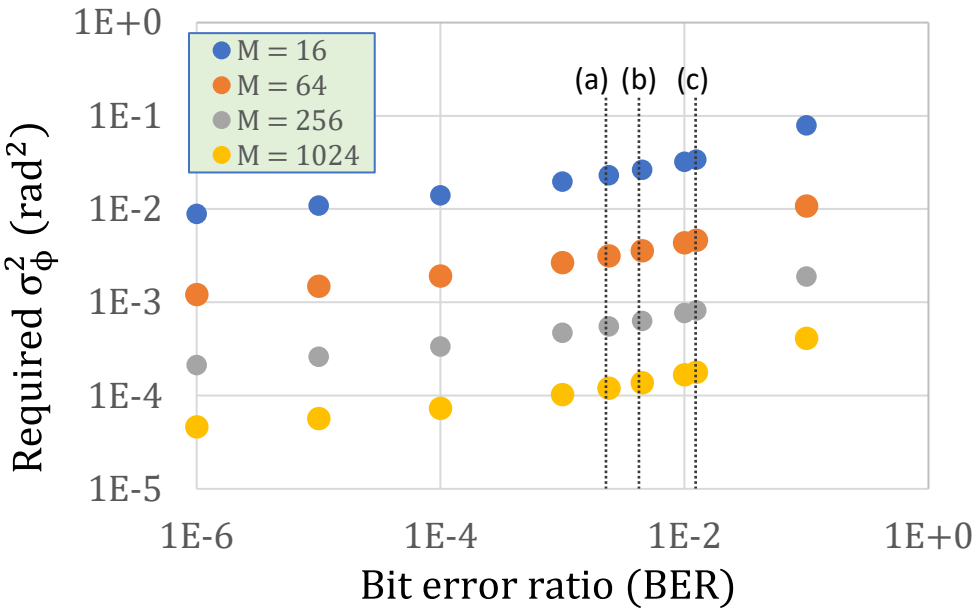

Figure 6.7. Required residual phase error variance, σ_ϕ^2, to achieve a given bit error ratio (BER) for modulation orders *M* = 16-, 64-, 256-, and 1024-QAM. BER thresholds labeled (a-c) correspond to KP4 FEC @ $2.4x10^{-3}$, Staircase FEC @ $4.5x10^{-3}$, and Concatenated Hamming + Staircase FEC @ $1.25x10^{-2}$ [112], [120].

The three BER thresholds labeled as (a-c) on Figure 6.7 correspond to forward error correction schemes of KP4 FEC @ BER = $2.4x10^{-3}$, staircase FEC @ BER = $4.5x10^{-3}$, and concatenated Hamming + staircase FEC @ BER = $1.25x10^{-2}$, respectively [112], [120].

These calculated residual phase error thresholds are next illustrated alongside the experimental OFS-PLL residual phase error results in Figure 6.8, demonstrating compatibility in a high order QAM link.

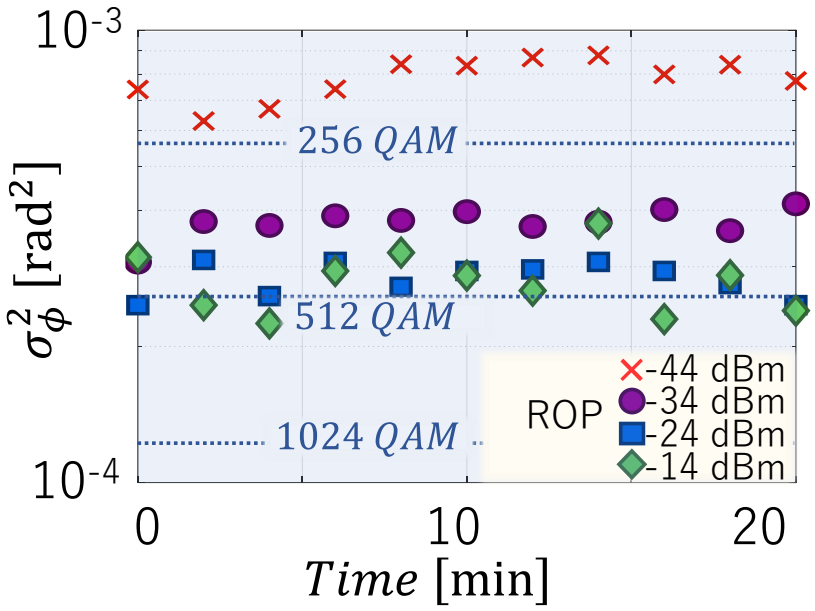

Figure 6.8. Residual phase error variance, σ_ϕ^2 [rad^2], of the optical-frequency-stabilized phase locked loop for various received optical carrier powers (ROP). High-order QAM thresholds for phase noise limited links at a bit error ratio (BER) of 2.4x10^{-3} are plotted, corresponding to the KP4-FEC threshold.

Using this estimation approach, a residual phase error variance of ~3x10^{-4} is predicted to be sufficient for at least 256-QAM transmission at received carrier optical powers as low as -34 dBm. With minor improvements to the phase lock performance to reach residual phase error variance better than 1x10^{-4} rad^2 in future generations, suitability for 512-QAM can be achieved.

6.4 Coherent link testbed

This section describes the construction and configuration of the communication electronics sub-systems for a high-capacity optical coherent link testbed. These systems include electrical data generation using an arbitrary waveform generator (AWG), electrical-to-optical data modulators using discrete commercial lithium niobate coherent modulators, and electrical coherent receiver using a commercial optical modulation analyzer (OMA).

This link setup served as the test environment for all optical transmission experiments, allowing direct comparison of a standard homodyne reference link to the FRESCO link results presented in Section 6.5. Parameters for the test setup are provided to enable a user to replicate the performance demonstrated here.

An experimental schematic of the electronics chain for the coherent link is shown in Figure 6.9.

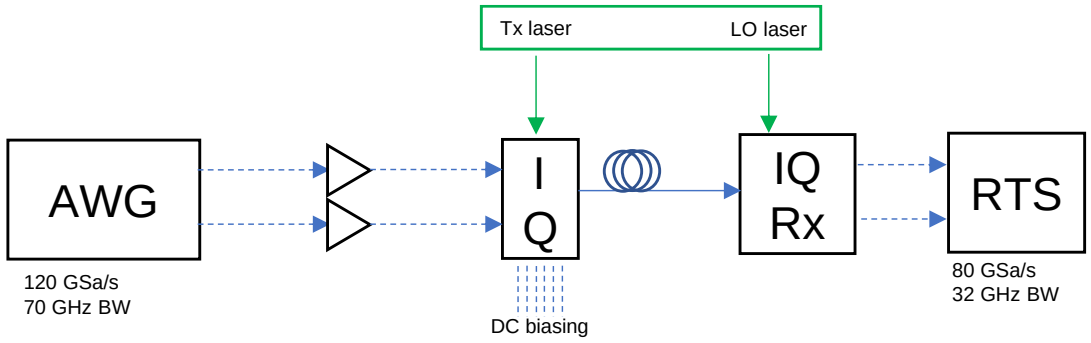

Figure 6.9. Electronic chain for the coherent link testbed. An arbitrary waveform generator (AWG) sources the electrical data signal. An electro-optic coherent modulator (IQ) writes the electrical data signal onto an optical carrier (transmit laser, Tx). A local oscillator is mixed with the optical data signal in a coherent 90 degree hybrid receiver (IQ Rx) and sampled on a real-time oscilloscope (RTS).

An arbitrary waveform generator (AWG, Keysight M8194a) sources the electrical data signal (effectively, a digital-to-analog convertor, DAC). An electro-optic coherent nested Mach-Zehnder modulator (commercial lithium niobate dual polarization discrete modulator with 35 GHz 3 dB bandwidth, Oclaro DP-IQ-MZM) modulates the electrical data signal onto an optical carrier (transmit laser, Tx). The local oscillator (LO) is mixed with the optical data signal in a coherent 90 degree hybrid receiver (IQ Rx) and sampled on a real-time oscilloscope (RTS). The optical receiver and real-time-scope (high speed analog-to-digital convertors, ADCs) used in these experiments were bundled in a commercial optical modulation analyzer (OMA, Keysight N4391A) with 32 GHz analog bandwidth and 80

GSa/s. Built-in commercial software was used to decode and recover the coherent data, providing experimental constellations and link performance metrics such as BER.

Parameters for the transmitter electronics are provided in Table 6.2 and for receiver electronics and software in Table 6.3.

Table 6.2. Symbol encoding / DAC settings on arbitrary waveform generator for baseline performance

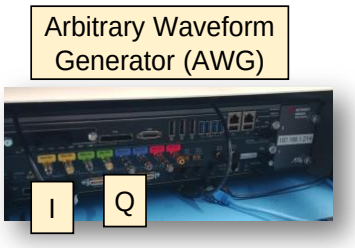

AWG setting/parameter	Value
CH1 amplitude, offset (I)	144 mV, 0 mV
CH2 amplitude, offset (Q)	147 mV, 0 mV
Sample rate	120e9 Hz
Symbol rate	10-56 GBd
Type of data	PRBS 2^{11}-1
# Symbols	3000
Modulation Type	QPSK, …, 256-QAM
Pulse shaping	Root Raised Cosine
Filter length	80
Roll-off (alpha)	0.35
Quadrature error	0 dB
IQ Skew	35.4 ps
Gain Imbalance	0 dB
Carrier offset	0 Hz
Download config	I→CH1, Q→CH2

Table 6.3. Settings for ADCs, IQ data recovery built into optical modulation analyzer (OMA)

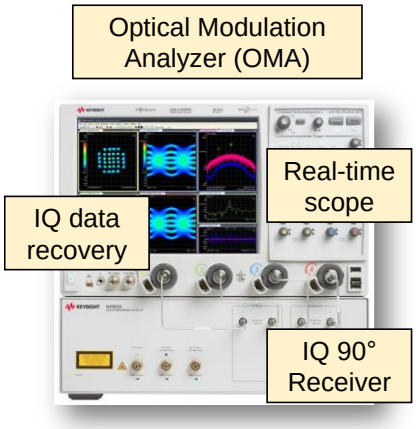

OMA setting/parameter	Value
Constellation	4-QAM, …, 256-QAM
Symbol Rate	10-56 GHz
Result length	1000 symbols
Measurement filter	Root Raised Cosine
Reference filter	Raised Cosine
Alpha/BT	0.35
Equalization Enable?	Yes = adaptive EQ, No = EQ loaded into AWG signal
Filter length	0-99 taps
Convergence	1e-6
Bit-error measurement?	Yes
Reference	PRBSes, 2^{11}-1
Window size for BER	20 Frames
Upper measurement limit	10000 Symbols
Frequency estimation?	NO = OFS-PLL YES = default
IQ Normalization?	Yes, constellation max

Channel frequency response data was measured for each I and Q signal paths independently in order to apply linear pre-distortion to flatten the channel. This was done with built-in IQTools package (Keysight proprietary software), though similar routines could be developed in-house using a vector network analyzer (VNA) or by measuring the receive-side electrical spectrum directly from the real time oscilloscope. The frequency responses are shown in Figure 6.10.

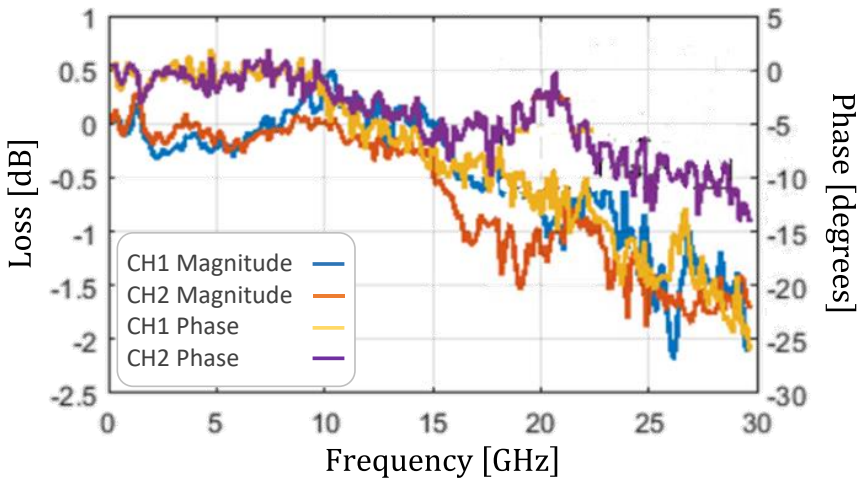

Figure 6.10. Measured electrical magnitude and phase frequency responses for signal CHs 1 and 2 (I and Q). This response is inverted and applied to the arbitrary waveform generator digital-to-analog convertors (DACs) such the transmitted signal frequency response is flat.

For both *I* and *Q* channels, the transmit electrical chains show a <2 dB rolloff up to 30 GHz. These components are shown in the photograph in Figure 6.11 in a rack-mountable enclosure that housed the discrete IQ modulator and driver amplifiers (SHF 807c).

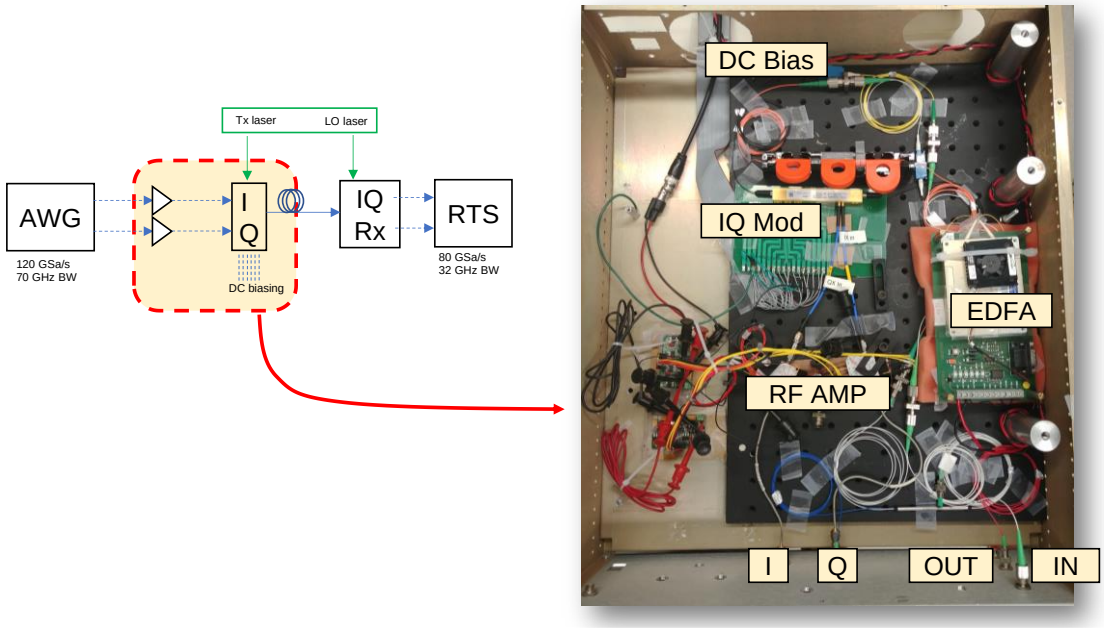

Figure 6.11. The coherent modulator (dual polarization nested MZM) and modulator drivers (high-speed RF amplifiers) were housed in a rack-mounted metal enclosure. Bulkhead fiber connectors enabled simple interfacing with external laser sources.

Housing the sensitive transmission electronics and fiber interfaces in a rack-mounted enclosure allowed for simple swapping of fiber optic inputs, and therefore simple swapping of test lasers to directly compare performance between spectrally pure sources. The link was first optimized in a standard homodyne reference link configuration, then operated directly with a FRESCO laser source and phase recovery in a best effort to hold all other link parameters constant. Results for a FRESCO link and OFS-PLL are discussed in the following Section 6.5.

6.5 The FRESCO link

This section demonstrates OFS-PLL phase recovery to enable a FREquency Stabilized Coherent Optical (FRESCO) link. The high performance (low residual phase error variance) phase recovery is shown to be suitable for use in a high-order QAM link without the need for DSP-based carrier recovery or frequency offset correction. These results demonstrate promise for future low power, high spectral efficiency DSP-free datacenter interconnects.

A high-level experimental schematic showing the OFS-PLL in a coherent link is shown in Figure 6.12. Two stable lasers source the transmit and local oscillator carriers. An AWG and IQ modulator encode data on the transmit carrier. After transmission over an optical fiber span, a 2x4 hybrid splits and optically mixes the data and LO signals onto a balanced photodetector as a phase error detector, as described for the OFS-PLL previously in Chapter 5. Under closed loop operation, the LO and data signals are phase synchronized and I and Q signals are demodulated by the 90° hybrid and real-time-scope. The coherent constellation is processed and recovered to report link performance metrics such as PRBS error counting.

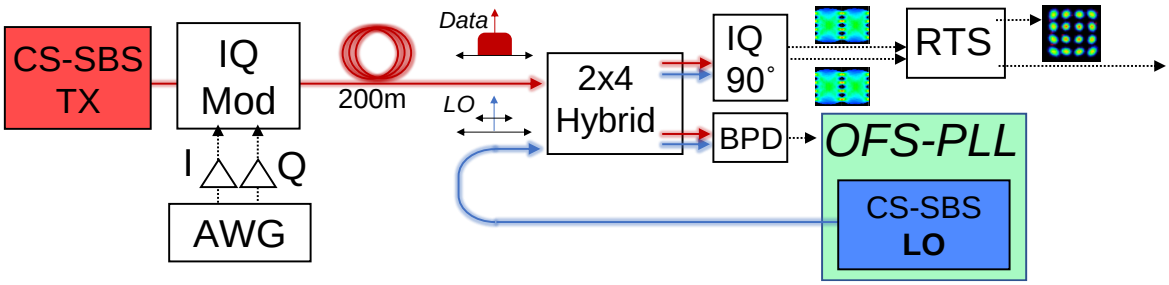

Figure 6.12. Two stable lasers (CS-SBS) source the transmit (Tx) and local oscillator (LO) carriers. An arbitrary waveform generator (AWG) and coherent modulator (IQ Mod) encode data on the transmit carrier. A 2x4 optical hybrid splits the optical signals into the phase detection and data detection branches. The optical-frequency-stabilized phase locked loop (OFS-PLL) performs the carrier phase lock on the receiver side. A real-time-scope recovers the demodulated data.

The FRESCO system was experimentally realized using fiber interconnected, chip-scale subsystems as shown in Figure 6.13. The transmit and local oscillators were constructed on independent optical tables, separated by a rack that housed the communications electronics and coherent modulator testbed.

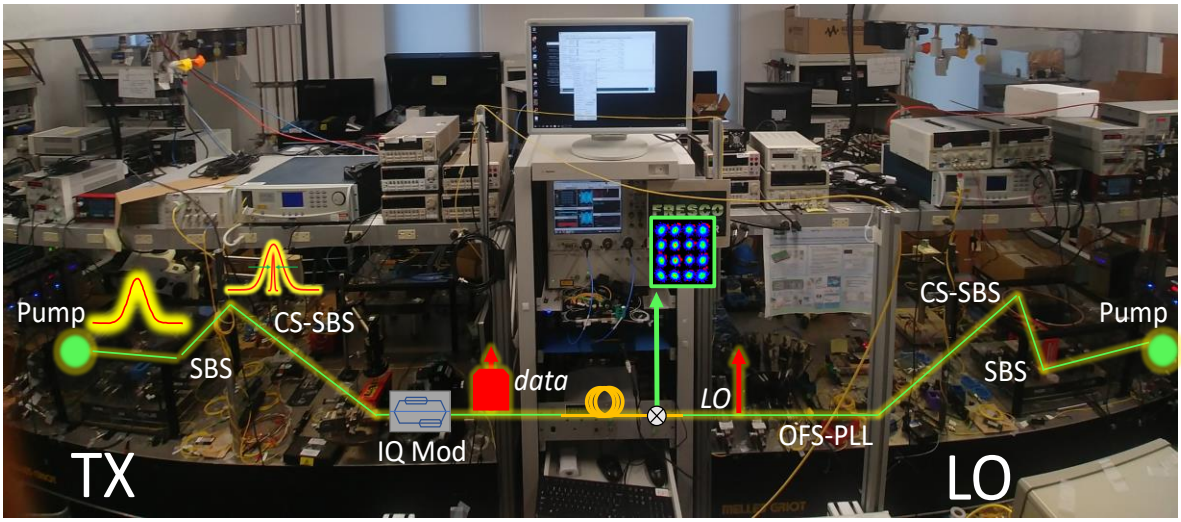

Figure 6.13. Laboratory setup of the FREquency Stabilized Coherent Optical (FRESCO) link. Two cavity-stabilized SBS lasers (SBS) serve as the transmit (TX) and local oscillators. Carrier phase recovery is realized using the optical-frequency stabilized phase locked loop (OFS-PLL). Coherent data and constellation recovery is performed using a commercial optical modulation analyzer (OMA).

Optical signal-to-noise-ratio for the FRESCO link

Though the OFS-PLL achieves a low residual phase error, satisfying one major requirement for high order QAM transmission, other sources of noise that impair link performance were also considered and independently optimized. Of particular concern was maintaining a high optical signal-to-noise ratio (OSNR), especially due to the multiple stages of optical amplification in the stable laser sources that could potentially result in a high level of background amplified spontaneous emission (ASE). Careful OSNR measurements were conducted at multiple locations within both the Tx and LO FRESCO systems to identify key points in the link for reducing optical loss and/or improving optical amplification noise figures, both of which are critical for high OSNR. A schematic showing a detailed view of the FRESCO subsystems and OSNR measurement locations labeled (a-f) for both the Tx and LO stable laser sources is shown in Figure 6.14.

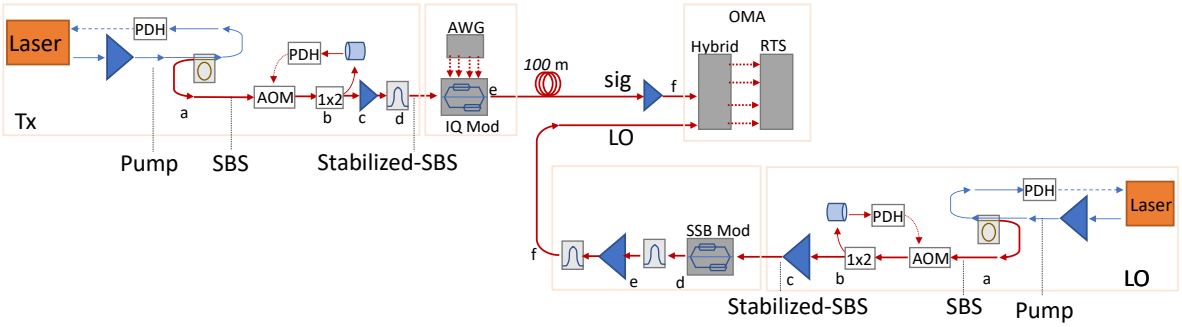

Figure 6.14. Detailed schematic of the FRESCO subsystems with key OSNR measurement locations labeled (a-f) for both the transmit and local oscillator stable lasers.

An optical spectrum analyzer (OSA) with resolution bandwidth set to 0.1 nm was used to measure OSNR at each point in the system labeled above. OSNR values were extracted by measuring the difference between carrier power and background optical noise level due to amplified spontaneous emission (ASE). To do this, a routine was developed to find the peak optical power, fit a spline to the background ASE level, and then calculate the difference

between these two levels as the OSNR. Additional information on this method as well as a thorough characterization of EDFAs in single- and cascaded-operation are given in Appendix A. At measurement locations (a-f), peak optical powers and OSNRs are summarized for the Tx and LO stable laser carriers in Table 6.4.

Table 6.4. Transmit and local oscillator peak optical powers and optical signal-to-noise ratios (OSNR) at each of the measurement locations (a-f) labeled in Figure 6.14. Tx measurements at e* and f* are OSNRs of data modulated signals with baudrates of 10, 28 and 56 GBd (e*) and 28 and 56 GBd (f*)

Tx			LO		
Loc.	**P_{peak}**	**OSNR**	**Loc.**	**P_{peak}**	**OSNR**
a	7.4	62.9	a	7.0	59.6
b	-4.8	58.9	b	-5.3	58.5
c	17.5	49.8	c	16.8	51.6
d	14.9	50.1	d	2.6	54.3
e*	-13,-18,-22	48,44,42	e	-6.3	52.9
f*	-3.6,-5.9	44, 40	f	16.6	49.1

For the transmitter, the largest OSNR degradation occurs at the coherent modulator (between points (d) and (e)) due to high optical loss, which ranged from 30 dB for 10 GBd modulation to as high as 37 dB for 56 GBd modulation. This dependence on baudrate is a result of constant total power in the carrier but larger modulation bandwidth, which spreads signal power over a larger span of ASE. This results in a larger total noise power for a constant signal power and therefore a larger OSNR. As such, modulator insertion loss and signal rates must be carefully considered when operating a coherent link. As an indicator of best case OSNR for the transmit and local oscillator stable lasers, an OSNR measurement of the unmodulated transmit carrier and tunable local oscillator is shown in Figure 6.15.

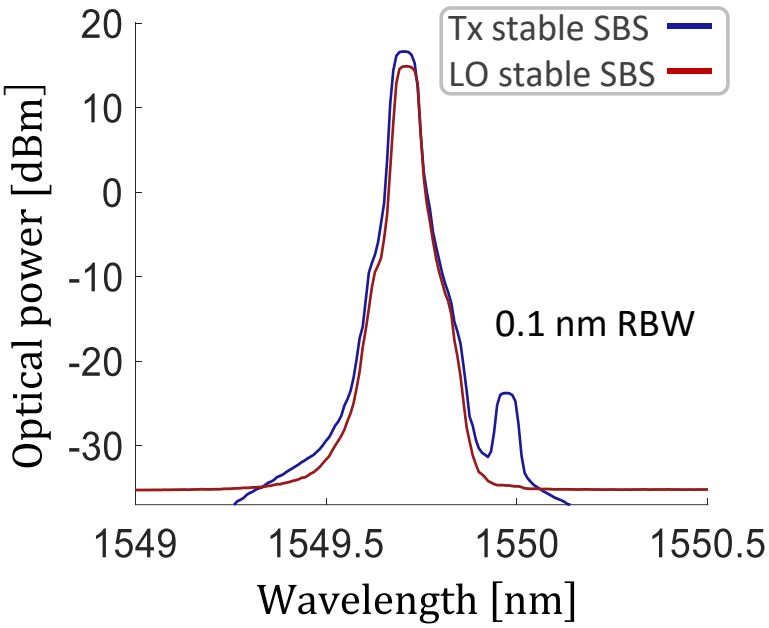

Figure 6.15. OSNR of the unmodulated transmit- and local oscillator stable SBS lasers. For the LO carrier, an unsuppressed sideband from the single-sideband modulator is observed ~40 dB below the carrier.

These measurements of OSNR show suitability of FRESCO lasers for high-order coherent modulation [101].

FRESCO transmission, constellations, and BER

This section presents FRESCO transmission results for multiple data rates and modulation orders. To demonstrate successful operation in a format with high sensitivity to phase error (due to very low angular separation of nearest neighbor symbols), a 256-QAM link was achieved at 10 GBd. To show high net data capacity, a 56 GBd 64-QAM link was achieved yielding a pre-FEC aggregate data rate of 56GBd · √64QAM = 336 Gbit/s. Constellations and eye diagrams of numerous link configurations are shown in Figure 6.16.

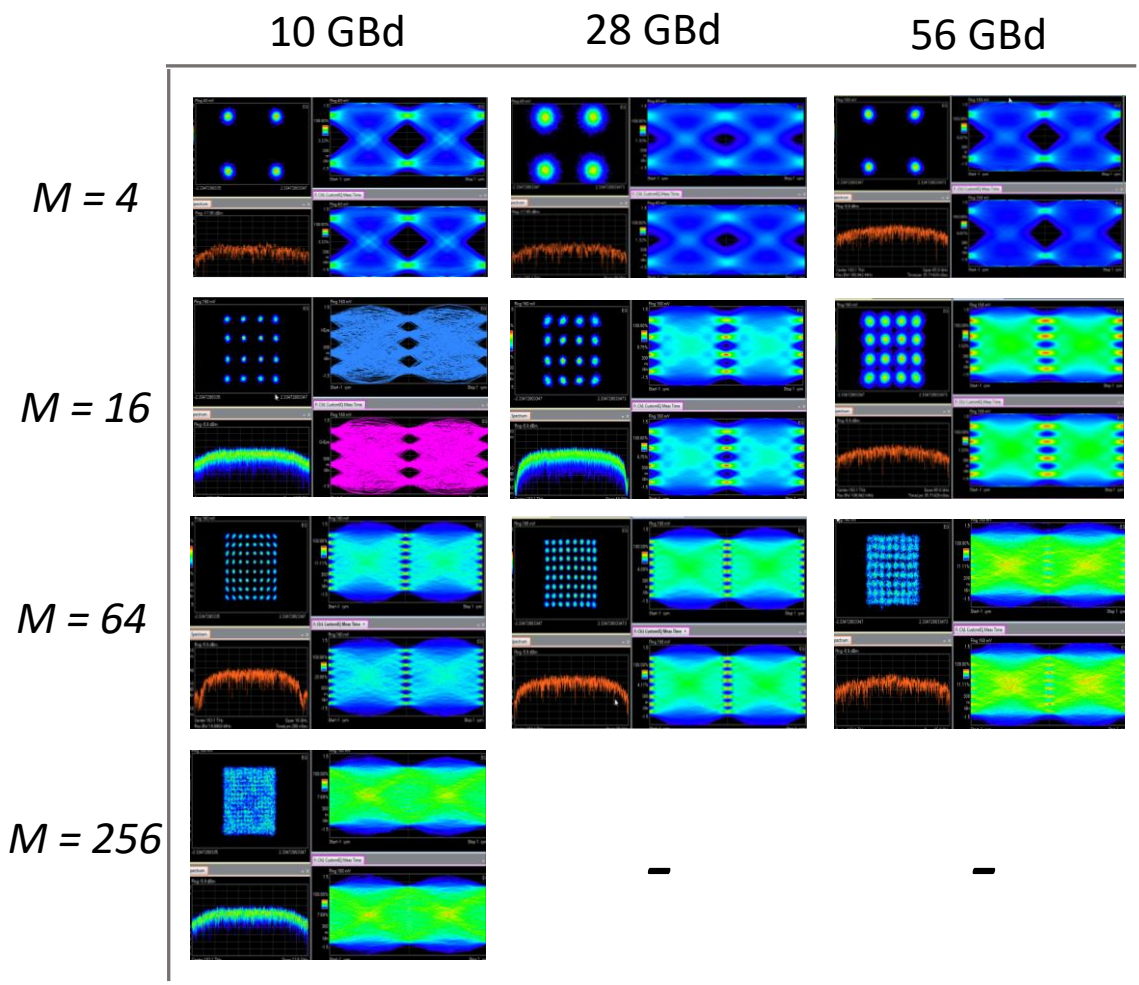

Figure 6.16. FRESCO constellations and eye diagrams for symbol rates of 10, 28, and 56 GBd and modulation orders M = 4-, 16-, 64-, and 256-QAM. **For the 10- and 28 GBd 4-QAM tiles, the receiver did not include an optical preamplifier EDFA resulting in the higher SNR constellations in comparison to 56GBd 4-QAM. Transmission of 256-QAM at data rates of 28 and 56 GBd was not achieved in these demonstrations

At a symbol rate of 10 GBd, constellations for modulation orders spanning QPSK to 256-QAM were successfully recovered. The recovery of an M = 256-QAM is an indicator that the phase recovery is suitable for high order QAM transmission, and that link performance is not limited by OFS-PLL performance. However, as symbol rates were increased to 28 GBd and 56 GBd, the highest recoverable modulation format was 64-QAM. The 5x higher symbol rates additionally strained the channel due to the required higher bandwidths, tighter restrictions on channel distortion compensation, and/or larger integration of channel noise.

To better characterize FRESCO link performance, BER was measured as a function of received optical power (ROP, power measured directly before the coherent hybrid receiver), plotted in Figure 6.17 for link configurations of QPSK (4-QAM) up to 64-QAM and baudrates of 10 GBd to 56 GBd. Also plotted are data points for a homodyne coherent reference link operating at 28 GBd, 64-QAM to directly compare FRESCO performance to a standard link.

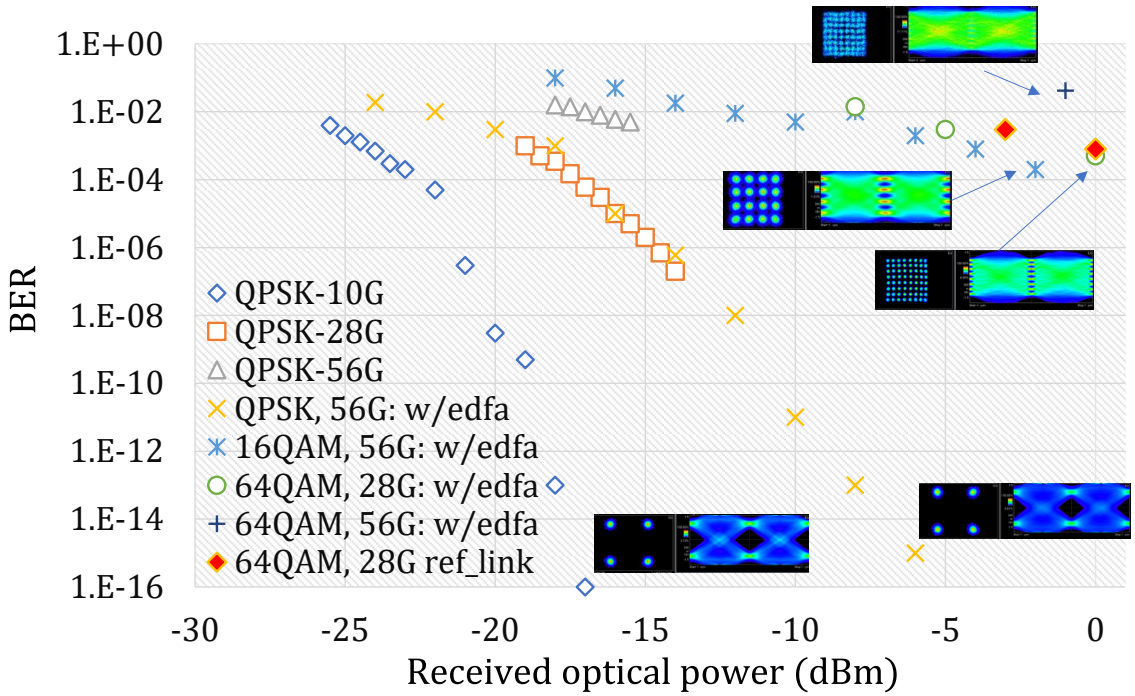

Figure 6.17. Bit error ratio versus received optical powers for multiple FRESCO transmission configurations (w/, w/o EDFA refers to receiver with an optical preamplifier). A homodyne reference link for 28GBd 64-QAM is plotted in red diamonds

For lower order modulation formats, error free data transmission was achieved without the need of an optically pre-amplified receiver as shown in the QPSK traces for data rates of 10, 28, and 56 GBd. At the highest QPSK data rate of 56 GBd, an additional comparison was done between a link with and without an optically pre-amplified receiver, and performance was observed to improve with the amplifier.

As modulation orders and baudrates were increased, performance degraded as can be observed by the BER v. ROP curves shifting to the right and 'flattening' at higher received optical powers. Shifting of the curves for higher modulation orders can be expected, as the tighter decision boundaries place more stringent requirements on signal-to-noise ratio [101], [106]. The effects of increasing baudrate, however, can be more nuanced as the SNR impairments can be a combination of bandwidth limitations of link components, increasing restrictions on channel equalization, and larger integration bounds on channel ASE and therefore increased sensitivity to OSNR. The flattening of the curves with respect to high received optical powers at first suggests that OSNR could have been a limiting factor, as increasing optical power had little effect on improving link performance. In other words, regardless of increased received optical power, the BER remained constant which might imply a constant SNR. This makes sense if OSNR was the limiting factor, as increasing the average optical power increases both the carrier and ASE powers, i.e., OSNR is left unchanged and therefore no improvement in BER should be expected. However, the previously presented measurements of signal OSNRs (>42 dB) exceed the requirements typically reported in literature for high order QAM transmission (e.g., 23 dB for 64-QAM @ BER=$1x10^{-3}$ [121]). This suggests that other link impairments (possibly bandwidth limitations or possibly, nonlinearities [116]) were straining link performance, and its investigation remains a subject of ongoing and future work.

Receiver sensitivities, defined as the received optical power required to meet a certain BER (here, a BER of $1x10^{-3}$ was chosen) are summarized in Figure 6.18. For receiver sensitivities, lower is better, as this corresponds to a lower optical power requirement to

achieve a given BER performance. The optical modulation analyzer configuration with- and without- optically pre-amplified detection at the 90° hybrid is also shown.

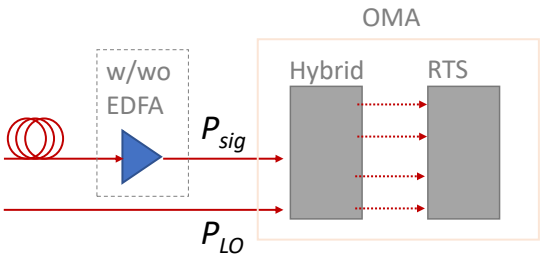

M	GBd	GBps	edfa Preamp?	Rx Sens @ 1e-3
4	10	20	no	-24 dBm
4	28	56	no	-19 dBm
4	56	112	no	n/a
4	56	112	yes	-19 dBm
16	56	224	yes	-5 dBm
64	28	168	yes	-2 dBm
64	56	336	yes	n/a
64	28	168	yes	-1 dBm

Figure 6.18. Receiver (optical modulation analyzer, OMA) configuration showing 'with' and 'without' erbium-doped fiber preamplifier. Receiver sensitivities for the tested FRESCO configurations (lower is better). Reference homodyne link (red diamond) shows similar performance to FRESCO link, suggesting performance is limited by the testbed and not the FRESCO systems

QPSK transmission without an optical preamplifier was possible with receiver sensitivities of -24 dBm and -19 dBm for 10 GBd and 28 GBd, respectively. At 56 GBd, QPSK was unrecoverable without the optical preamplifier and receiver sensitivity was measured to be -19 dBm again with the preamplifier in use. At higher modulation orders and baudrates, receiver sensitivities approached 0 dBm. For the highest format and baudrate, 64-QAM @ 56-GBd, the measured BER exceeded the chosen threshold of $1x10^{-3}$ and a receiver sensitivity is not reported. The homodyne reference 28 GBd 64-QAM link achieved a receiver sensitivity of -1 dBm, which actually exceeds the FRESCO link receiver sensitivity of -2 dB for the same configuration, *suggesting that the FRESCO link performance is limited by the coherent link testbed and not by the chip-scale lasers and phase synchronization systems*.

To provide context of these transmission results in terms of suitability for ultra-high capacity coherent communications, the aggregate pre-FEC data rates for these tested FRESCO configurations is summarized in Table 6.5.

Table 6.5. Aggregate pre-FEC data rates for each of the tested FRESCO configurations. Power of the phase synchronization approach and corresponding energy per bit for this work and future projections.

Aggregate pre-FEC data rate (Gbps)			
QAM \ Gbd	10	28	56
4	20	56	112
16	40	112	224
64	60	168	336
256	80	224	448

Power W	pJ/bit	
10	~30	*this work
1.5	~5	future
0.5	~2	↓

The high-speed FRESCO demonstration of 64-QAM at 56 GBd achieves a pre-FEC data rate of 336 Gbps for a single carrier. However, current results demonstrate this at a relatively high BER (~$1x10^{-2}$), requiring one of the more relaxed forward error correction schemes, a concatenated Hamming + staircase FEC [112], [120], with a threshold BER of $1.25x10^{-2}$. The FEC overhead, or the percentage of signal stream that encodes the error correction bits versus information bits, for this scheme is 14.8%. This results in a post-FEC effective data rate of ~ 287 Gbps. The power consumption for this scheme is ~ 3x higher than the more common KP4 FEC scheme and additionally suffers from higher latency [120]. As such, the slight improvement in FRESCO link performance to reach the KP4 FEC threshold of $2.4x10^{-3}$ [112] is a worthwhile endeavor and subject of ongoing efforts.

7 Conclusion

This thesis has reported the development of chip-scale spectrally pure optical sources with ~1 Hz fundamental linewidths, 30 Hz integral linewidths, and carrier instabilities better than $2x10^{-13}$ at timescales of 50 ms. These sources were demonstrated in an optically phase synchronized fiber optic link, realizing the optical-frequency-stabilized phase locked loop (OFS-PLL) with ultra-low residual phase error variance of $3x10^{-4}$ rad^2 at low received optical powers of -34 dBm. Finally, the phase synchronization approach was used for carrier phase synchronization to enable coherent data transmission at data rates and modulation orders between of 256-QAM at 10 GBd and 64-QAM at 56 GBd.

Future realizations of these spectrally pure chip scale lasers and phase synchronization systems can benefit from greater levels of silicon photonic integration, such as heterogeneously integrated pump sources [32], [33], [61], [76], frequency tuners [77], [97], and mW-tier Bi-CMOS electronics for further reduced power and footprint. Notably, by replacing the currently used acousto-optic modulators that consume ~3 Watts per stabilization loop, a major improvement can be made in energy efficiency. Promising replacements that have been demonstrated in literature are SiPh single sideband modulators fabricated within 3 mm^2 footprint with power consumption of just under 200 mW [77].

For reduced footprint and improved scalability, waveguide integrated reference cavities can be used in place of the compact bulk optical reference cavity. Demonstrations of thermally engineered waveguide coil [122] and ring reference cavities [58], [59] for stabilization are promising alternatives.

In coherent communications applications, extension to wave-division multiplexed (WDM) operation while maintaining high-spectral purity [27], [123] can amortize cost and

complexity over multiple optical channels. The achieved performance and potential for energy-efficiency ultra-high capacity links offer promise for bringing high order QAM transmission to future DSP-free, data center interconnects.

References

[1] R. W. P. Drever *et al.*, "Laser phase and frequency stabilization using an optical resonator," *Appl. Phys. B*, vol. 31, no. 2, pp. 97–105, Jun. 1983, doi: 10.1007/BF00702605.

[2] T. Kessler *et al.*, "A sub-40-mHz-linewidth laser based on a silicon single-crystal optical cavity," *Nature Photon*, vol. 6, no. 10, pp. 687–692, Oct. 2012, doi: 10.1038/nphoton.2012.217.

[3] D. G. Matei *et al.*, "1.5 μm lasers with sub-10 mHz linewidth," *Phys. Rev. Lett.*, vol. 118, no. 26, p. 263202, Jun. 2017, doi: 10.1103/PhysRevLett.118.263202.

[4] Y. Y. Jiang *et al.*, "Making optical atomic clocks more stable with 10−16-level laser stabilization," *Nature Photon*, vol. 5, no. 3, pp. 158–161, Mar. 2011, doi: 10.1038/nphoton.2010.313.

[5] L.-S. Ma, P. Jungner, J. Ye, and J. L. Hall, "Delivering the same optical frequency at two places: accurate cancellation of phase noise introduced by an optical fiber or other time-varying path," *Opt. Lett.*, vol. 19, no. 21, p. 1777, Nov. 1994, doi: 10.1364/OL.19.001777.

[6] J. L. Hall and M. Zhu, "An introduction to phase-stable optical sources," in *International School of Physics Enrico Fermi Course CXVII, Laser Manipulation of Atoms and Ions*, North Holland, CH, Apr. 1993, pp. 671–702.

[7] S. M. Foreman, K. W. Holman, D. D. Hudson, D. J. Jones, and J. Ye, "Remote transfer of ultrastable frequency references via fiber networks," *Review of Scientific Instruments*, vol. 78, no. 2, p. 021101, Feb. 2007, doi: 10.1063/1.2437069.

[8] S. M. Foreman, A. D. Ludlow, M. H. G. de Miranda, J. E. Stalnaker, S. A. Diddams, and J. Ye, "Coherent optical phase transfer over a 32-km fiber with 1 s instability at 10-17," *Phys. Rev. Lett.*, vol. 99, no. 15, p. 153601, Oct. 2007, doi: 10.1103/PhysRevLett.99.153601.

[9] D. Calonico *et al.*, "High-accuracy coherent optical frequency transfer over a doubled 642-km fiber link," *Appl. Phys. B*, vol. 117, no. 3, pp. 979–986, Dec. 2014, doi: 10.1007/s00340-014-5917-8.

[10] C. Clivati *et al.*, "A coherent fiber link for very long baseline interferometry," *IEEE Transactions on Ultrasonics, Ferroelectrics, and Frequency Control*, vol. 62, no. 11, pp. 1907–1912, Nov. 2015, doi: 10.1109/TUFFC.2015.007221.

[11] B. M. Roberts *et al.*, "Search for transient variations of the fine structure constant and dark matter using fiber-linked optical atomic clocks," *New J. Phys.*, vol. 22, no. 9, p. 093010, Sep. 2020, doi: 10.1088/1367-2630/abaace.

[12] P. Delva *et al.*, "Test of Special Relativity Using a Fiber Network of Optical Clocks," *Phys. Rev. Lett.*, vol. 118, no. 22, p. 221102, Jun. 2017, doi: 10.1103/PhysRevLett.118.221102.

[13] C. Clivati *et al.*, "Common-clock very long baseline interferometry using a coherent optical fiber link," *Optica, OPTICA*, vol. 7, no. 8, pp. 1031–1037, Aug. 2020, doi: 10.1364/OPTICA.393356.

[14] M. Fujieda, M. Kumagai, S. Nagano, A. Yamaguchi, H. Hachisu, and T. Ido, "All-optical link for direct comparison of distant optical clocks," *Opt. Express*, vol. 19, no. 17, p. 16498, Aug. 2011, doi: 10.1364/OE.19.016498.

[15] F. Riehle, “Optical clock networks,” *Nature Photon*, vol. 11, no. 1, pp. 25–31, Jan. 2017, doi: 10.1038/nphoton.2016.235.
[16] J. Grotti *et al.*, “Geodesy and metrology with a transportable optical clock,” *Nature Phys*, vol. 14, no. 5, pp. 437–441, May 2018, doi: 10.1038/s41567-017-0042-3.
[17] C. Lisdat *et al.*, “A clock network for geodesy and fundamental science,” *Nat Commun*, vol. 7, no. 1, p. 12443, Nov. 2016, doi: 10.1038/ncomms12443.
[18] W. Zhang *et al.*, “Ultranarrow linewidth photonic-atomic laser,” *Laser & Photonics Reviews*, vol. 14, no. 4, p. 1900293, Apr. 2020, doi: 10.1002/lpor.201900293.
[19] L. Stern *et al.*, “Ultra-precise optical-frequency stabilization with heterogeneous III–V/Si lasers,” *Opt. Lett.*, vol. 45, no. 18, p. 5275, Sep. 2020, doi: 10.1364/OL.398845.
[20] H. Lee, M.-G. Suh, T. Chen, J. Li, S. A. Diddams, and K. J. Vahala, “Spiral resonators for on-chip laser frequency stabilization,” *Nat Commun*, vol. 4, no. 1, p. 2468, Dec. 2013, doi: 10.1038/ncomms3468.
[21] W. Loh *et al.*, “Dual-microcavity narrow-linewidth Brillouin laser,” *Optica*, vol. 2, no. 3, p. 225, Mar. 2015, doi: 10.1364/OPTICA.2.000225.
[22] W. Loh *et al.*, “A microrod-resonator Brillouin laser with 240 Hz absolute linewidth,” *New J. Phys.*, vol. 18, no. 4, p. 045001, Apr. 2016, doi: 10.1088/1367-2630/18/4/045001.
[23] W. Liang *et al.*, “Ultralow noise miniature external cavity semiconductor laser,” *Nat Commun*, vol. 6, no. 1, p. 7371, Nov. 2015, doi: 10.1038/ncomms8371.
[24] W. Liang, V. S. Ilchenko, A. A. Savchenkov, A. B. Matsko, D. Seidel, and L. Maleki, “Whispering-gallery-mode-resonator-based ultranarrow linewidth external-cavity semiconductor laser,” *Opt. Lett.*, vol. 35, no. 16, p. 2822, Aug. 2010, doi: 10.1364/OL.35.002822.
[25] K. Liu *et al.*, “Self-Similar Ultra-High Q Si3N4 Integrated Resonators for Brillouin Laser Linewidth Narrowing and Stabilization,” in *2021 Optical Fiber Communications Conference and Exhibition (OFC)*, Jun. 2021, pp. 1–3.
[26] K. Liu *et al.*, “Photonic circuits for laser stabilization with ultra-low-loss and nonlinear resonators,” p. 21.
[27] W. Jin *et al.*, “Hertz-linewidth semiconductor lasers using CMOS-ready ultra-high-Q microresonators,” *Nat. Photonics*, vol. 15, no. 5, pp. 346–353, May 2021, doi: 10.1038/s41566-021-00761-7.
[28] D. J. Blumenthal *et al.*, “Frequency Stabilized Lasers for Coherent Fiber Interconnects in the Datacenter (Invited Talk),” in *2019 IEEE Optical Interconnects Conference (OI)*, Santa Fe, NM, USA, Apr. 2019, pp. 1–2. doi: 10.1109/OIC.2019.8714367.
[29] D. J. Blumenthal *et al.*, “Frequency-stabilized links for coherent WDM fiber interconnects in the datacenter,” *Journal of Lightwave Technology*, vol. 38, no. 13, pp. 3376–3386, Jul. 2020, doi: 10.1109/JLT.2020.2985275.
[30] G. M. Brodnik *et al.*, “Chip-scale, optical-frequency-stabilized PLL for DSP-free, low-power coherent QAM in the DCI,” in *Optical Fiber Communication Conference (OFC) 2020*, San Diego, California, 2020, p. M3A.6. Accessed: May 11, 2020. [Online]. Available: https://www.osapublishing.org/abstract.cfm?URI=OFC-2020-M3A.6
[31] P. A. Morton and M. J. Morton, “High-power, ultra-low noise hybrid lasers for microwave photonics and optical sensing,” *J. Lightwave Technol.*, vol. 36, no. 21, pp. 5048–5057, Nov. 2018, doi: 10.1109/JLT.2018.2817175.

[32] D. Huang *et al.*, “High-power sub-kHz linewidth lasers fully integrated on silicon,” *Optica*, vol. 6, no. 6, p. 745, Jun. 2019, doi: 10.1364/OPTICA.6.000745.
[33] G. M. Brodnik *et al.*, “Ultra-narrow linewidth chip-scale heterogeneously integrated silicon/III-V tunable laser pumped Si/Si3N4 SBS laser,” *CLEO 2020*, May 2020.
[34] S. Gundavarapu, “Sub-Hz Fundamental Linewidth Silicon Nitride Integrated Brillouin Lasers and Their,” UCSB, 2018.
[35] L. G. Kazovsky, “Balanced phase-locked loops for optical homodyne receivers: performance analysis, design considerations, and laser linewidth requirements,” *Journal of Lightwave Technology*, vol. LT-4, no. 2, pp. 182–195, 1986.
[36] K. Balakier, L. Ponnampalam, M. J. Fice, C. C. Renaud, and A. J. Seeds, “Integrated semiconductor laser optical phase lock loops,” *IEEE J. Select. Topics Quantum Electron.*, vol. 24, no. 1, pp. 1–12, Jan. 2018, doi: 10.1109/JSTQE.2017.2711581.
[37] N. Satyan, W. Liang, A. Yariv, and L. Fellow, “Optical Phase-Lock Loops,” *Quantum Electronics*, vol. 2009, no. July, pp. 1–7, 2009.
[38] N. Satyan, “Phase noise reduction of a semiconductor laser in a composite optical phase-locked loop,” *Opt. Eng*, vol. 49, no. 12, p. 124301, Dec. 2010, doi: 10.1117/1.3518077.
[39] M. Lu *et al.*, “Highly integrated optical heterodyne phase-locked loop with phase/frequency detection,” *Opt. Express*, vol. 20, no. 9, p. 9736, Apr. 2012, doi: 10.1364/OE.20.009736.
[40] L. N. Langley *et al.*, “Packaged semiconductor laser optical phase-locked loop (OPLL) for photonic generation, processing and transmission of microwave signals,” *IEEE Trans. Microwave Theory Techn.*, vol. 47, no. 7, pp. 1257–1264, Jul. 1999, doi: 10.1109/22.775465.
[41] A. C. Bordonalli, C. Walton, and A. J. Seeds, “High-performance phase locking of wide linewidth semiconductor lasers by combined use of optical injection locking and optical phase-lock loop,” *J. Lightwave Technol.*, vol. 17, no. 2, pp. 328–342, Feb. 1999, doi: 10.1109/50.744252.
[42] M. Grant, W. Michie, and M. Fletcher, “The performance of optical phase-locked loops in the presence of nonnegligible loop propagation delay,” *Journal of Lightwave Technology*, vol. 5, no. 4, pp. 592–597, Apr. 1987, doi: 10.1109/JLT.1987.1075532.
[43] R. T. Ramos and A. J. Seeds, “Comparison between first-order and second-order optical phase-lock loops,” *IEEE Microwave and Guided Wave Letters*, vol. 4, no. 1, pp. 6–8, Jan. 1994, doi: 10.1109/75.267677.
[44] A. M. Marino and C. R. Stroud, “Phase-locked laser system for use in atomic coherence experiments,” *Review of Scientific Instruments*, vol. 79, no. 1, p. 013104, Jan. 2008, doi: 10.1063/1.2823330.
[45] N. Hinkley *et al.*, “An Atomic Clock with 10-18 Instability,” *Science*, vol. 341, no. 6151, pp. 1215–1218, Sep. 2013, doi: 10.1126/science.1240420.
[46] M. I. Bodine *et al.*, “Optical atomic clock comparison through turbulent air,” *Phys. Rev. Research*, vol. 2, no. 3, p. 033395, Sep. 2020, doi: 10.1103/PhysRevResearch.2.033395.
[47] E. D. Black, “An introduction to Pound – Drever – Hall laser frequency stabilization,” *American Journal of Physics*, vol. 69, no. 1, pp. 79–87, 2001, doi: 10.1119/1.1286663.
[48] W. J. Riley, “Handbook of Frequency Stability Analysis,” p. 136.

[49] D. W. Allan, “Time and Frequency (Time-Domain) Characterization, Estimation, and Prediction of Precision Clocks and Oscillators,” *IEEE Transactions on Ultrasonics, Ferroelectrics, and Frequency Control*, vol. 34, no. 6, pp. 647–654, Nov. 1987, doi: 10.1109/T-UFFC.1987.26997.
[50] D. W. Allan, D. A. Howe, F. L. Walls, and D. B. Sullivan, “Characterization of clocks and oscillators,” National Bureau of Standards, Gaithersburg, MD, NBS TN 1337, 1990. doi: 10.6028/NIST.TN.1337.
[51] C. Henry, “Theory of the linewidth of semiconductor lasers,” *IEEE Journal of Quantum Electronics*, vol. 18, no. 2, pp. 259–264, Feb. 1982, doi: 10.1109/JQE.1982.1071522.
[52] A. L. Schawlow and C. H. Townes, “Infrared and Optical Masers,” *Phys. Rev.*, vol. 112, no. 6, pp. 1940–1949, Dec. 1958, doi: 10.1103/PhysRev.112.1940.
[53] P. Gallion and G. Debarge, “Quantum phase noise and field correlation in single frequency semiconductor laser systems,” *IEEE J. Quantum Electron.*, vol. 20, no. 4, pp. 343–349, Apr. 1984, doi: 10.1109/JQE.1984.1072399.
[54] G. Di Domenico, S. Schilt, and P. Thomann, “Simple approach to the relation between laser frequency noise and laser line shape,” *Appl. Opt.*, vol. 49, no. 25, p. 4801, Sep. 2010, doi: 10.1364/AO.49.004801.
[55] S. Gundavarapu *et al.*, “Sub-hertz fundamental linewidth photonic integrated Brillouin laser,” *Nature Photonics*, vol. 13, no. January, 2019, doi: 10.1038/s41566-018-0313-2.
[56] D. R. Hjelme, A. R. Mickelson, and R. G. Beausoleil, “Semiconductor laser stabilization by external optical feedback,” *IEEE J. Quantum Electron.*, vol. 27, no. 3, pp. 352–372, Mar. 1991, doi: 10.1109/3.81333.
[57] B. Li *et al.*, “Reaching fiber-laser coherence in integrated photonics,” *Opt. Lett.*, vol. 46, no. 20, p. 5201, Oct. 2021, doi: 10.1364/OL.439720.
[58] Q. Zhao *et al.*, “Integrated reference cavity with dual-mode optical thermometry for frequency correction,” *Optica*, vol. 8, no. 11, p. 1481, Nov. 2021, doi: 10.1364/OPTICA.432194.
[59] Q. Zhao *et al.*, “Low-loss low thermo-optic coefficient Ta2O5 on crystal quartz planar optical waveguides,” *APL Photonics*, vol. 5, no. 11, p. 116103, Nov. 2020, doi: 10.1063/5.0024743.
[60] G. M. Brodnik *et al.*, “Optically synchronized fibre links using spectrally pure chip-scale lasers,” *Nat. Photon.*, Jun. 2021, doi: 10.1038/s41566-021-00831-w.
[61] M. A. Tran, D. Huang, and J. E. Bowers, “Tutorial on narrow linewidth tunable semiconductor lasers using Si/III-V heterogeneous integration,” *APL Photonics*, vol. 4, no. 11, p. 111101, Nov. 2019, doi: 10.1063/1.5124254.
[62] S. Schilt *et al.*, “Frequency discriminators for the characterization of narrow-spectrum heterodyne beat signals: Application to the measurement of a sub-hertz carrier-envelope-offset beat in an optical frequency comb,” *Review of Scientific Instruments*, vol. 82, no. 12, p. 123116, Dec. 2011, doi: 10.1063/1.3670357.
[63] D. Derickson, *Fiber Optic Test and Measurement*. Prentice Hall, Upper Saddle River, NJ, USA, 1998.
[64] H. Wang, L. Wu, Z. Yuan, and K. Vahala, “Towards milli-Hertz laser frequency noise on a chip,” in *Conference on Lasers and Electro-Optics*, San Jose, California, 2021, p. SF2O.2. doi: 10.1364/CLEO_SI.2021.SF2O.2.

[65] S. Camatel and V. Ferrero, “Narrow Linewidth CW Laser Phase Noise Characterization Methods for Coherent Transmission System Applications,” *Journal of Lightwave Technology*, vol. 26, no. 17, pp. 3048–3055, Sep. 2008, doi: 10.1109/JLT.2008.925046.
[66] J. R. Vig and E. S. Ferre-Pikal, “IEEE Std 1139-1999 IEEE Standard Definitions of Physical Quantities fo r Fundamental Frequency and Time Metrology— Random Instabilities,” p. 36, 1999.
[67] A. Mooradian, “Laser Linewidth,” *Physics Today*, pp. 43–46, May 1985.
[68] H. Wang, L. Wu, Z. Yuan, and K. Vahala, “Towards milli-Hertz laser frequency noise on a chip,” *arXiv:2010.09248 [physics]*, Oct. 2020, Accessed: Nov. 02, 2021. [Online]. Available: http://arxiv.org/abs/2010.09248
[69] A. D. Ludlow *et al.*, “Compact, thermal-noise-limited optical cavity for diode laser stabilization at 1x10^-15,” *Optics Letters*, vol. 32, no. 6, pp. 641–643, Mar. 2007.
[70] T. Huffman, G. M. Brodnik, C. Pinho, S. Gundavarapu, D. M. Baney, and D. J. Blumeuthal, “Integrated Resonators in an Ultra -Low Loss Si 3 N 4/SiO 2 Platform for Multifunction Application s,” *IEEE Journal on Selected Topics in Quantum Electronics*, 2017.
[71] W. Zhang, F. Baynes, S. A. Diddams, and S. B. Papp, “Microrod Optical Frequency Reference in the Ambient Environment,” *Phys. Rev. Applied*, vol. 12, no. 2, p. 024010, Aug. 2019, doi: 10.1103/PhysRevApplied.12.024010.
[72] J. Lim *et al.*, “Chasing the thermodynamical noise limit in whispering-gallery-mode resonators for ultrastable laser frequency stabilization,” *Nat Commun*, vol. 8, no. 1, p. 8, Dec. 2017, doi: 10.1038/s41467-017-00021-9.
[73] A. Debut, S. Randoux, and J. Zemmouri, “Linewidth narrowing in Brillouin lasers: Theoretical analysis,” *Phys. Rev. A*, vol. 62, no. 2, p. 023803, Jul. 2000, doi: 10.1103/PhysRevA.62.023803.
[74] A. Debut, S. Randoux, and J. Zemmouri, “Experimental and theoretical study of linewidth narrowing in Brillouin fiber ring lasers,” *J. Opt. Soc. Am. B*, vol. 18, no. 4, p. 556, Apr. 2001, doi: 10.1364/JOSAB.18.000556.
[75] R. O. Behunin, N. T. Otterstrom, P. T. Rakich, S. Gundavarapu, and D. J. Blumenthal, “Fundamental noise dynamics in cascaded-order Brillouin lasers,” *Phys. Rev. A*, vol. 98, no. 2, p. 023832, Aug. 2018, doi: 10.1103/PhysRevA.98.023832.
[76] M. Tran, D. Huang, T. Komljenovic, J. Peters, A. Malik, and J. Bowers, “Ultra-Low-Loss Silicon Waveguides for Heterogeneously Integrated Silicon/III-V Photonics,” *Applied Sciences*, vol. 8, no. 7, p. 1139, Jul. 2018, doi: 10.3390/app8071139.
[77] M. H. Idjadi and F. Aflatouni, “Nanophotonic phase noise filter in silicon,” *Nat. Photonics*, vol. 14, no. 4, pp. 234–239, Apr. 2020, doi: 10.1038/s41566-020-0605-1.
[78] M. Nazarathy, W. V. Sorin, D. M. Baney, and S. A. Newton, “Spectral analysis of optical mixing measurements,” *Journal of Lightwave Technology*, vol. 7, no. 7, pp. 1083–1096, Jul. 1989, doi: 10.1109/50.29635.
[79] F. M. Gardner, *Phaselock Techniques, 3rd Edition*, 3rd ed. Hoboken, New Jersey: John Wiley and Sons Inc., Hoboken, New Jersey, 2005.
[80] H. Park *et al.*, “40Gbit / s coherent optical receiver using a Costas loop,” vol. 16, no. 2, 2012.

[81] R. T. Ramos and A. J. Seeds, “Delay, linewidth and bandwidth limitations in optical phase-locked loop design,” *Electron. Lett.*, vol. 26, no. 6, p. 389, 1990, doi: 10.1049/el:19900254.
[82] S. Ristic, A. Bhardwaj, M. J. Rodwell, L. A. Coldren, and L. A. Johansson, “An Optical Phase-Locked Loop Photonic Integrated Circuit,” *J. Lightwave Technol.*, vol. 28, no. 4, pp. 526–538, Feb. 2010, doi: 10.1109/JLT.2009.2030341.
[83] P. Corrc, O. Girad, and I. F. de Faria, “On the thermal contribution to the FM response of DFB lasers: theory and experiment,” *IEEE Journal of Quantum Electronics*, vol. 30, no. 11, pp. 2485–2490, Nov. 1994, doi: 10.1109/3.333699.
[84] M. Nakazawa, T. Hirooka, M. Yoshida, and K. Kasai, “Extremely higher-order modulation formats,” in *Optical Fiber Telecommunications (Sixth Edition)*, I. P. Kaminow, T. Li, and A. E. Willner, Eds. Boston: Academic Press, Boston, MA, 2013, pp. 297–336. Accessed: Mar. 05, 2021. [Online]. Available: https://www.sciencedirect.com/science/article/pii/B9780123969606000079
[85] J. Dong, J. Huang, T. Li, and L. Liu, “Observation of fundamental thermal noise in optical fibers down to infrasonic frequencies,” *Appl. Phys. Lett.*, vol. 108, no. 2, p. 021108, Jan. 2016, doi: 10.1063/1.4939918.
[86] L. Duan, “General treatment of the thermal noises in optical fibers,” *Phys. Rev. A*, vol. 86, no. 2, p. 023817, Aug. 2012, doi: 10.1103/PhysRevA.86.023817.
[87] M. Lu, “Integrated Optical Phase-locked Loops,” Thesis, University of California, Santa Barbara, 2013.
[88] B. S. G. Pillai *et al.*, “End-to-end energy modeling and analysis of long-haul coherent transmission systems,” *J. Lightwave Technol.*, vol. 32, no. 18, pp. 3093–3111, Sep. 2014, doi: 10.1109/JLT.2014.2331086.
[89] M. Kuschnerov *et al.*, “DSP for Coherent Single-Carrier Receivers,” *Journal of Lightwave Technology*, vol. 27, no. 16, pp. 3614–3622, Aug. 2009, doi: 10.1109/JLT.2009.2024963.
[90] J. K. Perin, A. Shastri, and J. M. Kahn, “Design of low-power DSP-free coherent receivers for data center links,” *J. Lightwave Technol.*, vol. 35, no. 21, pp. 4650–4662, Nov. 2017, doi: 10.1109/JLT.2017.2752079.
[91] C. Laperle and M. O’Sullivan, “Advances in high-speed DACs, ADCs, and DSP for optical coherent transceivers,” *J. Lightwave Technol.*, vol. 32, no. 4, pp. 629–643, Feb. 2014, doi: 10.1109/JLT.2013.2284134.
[92] T. Kupfer, A. Bisplinghof, T. Duthel, C. Fludger, and S. Langenbach, “Optimizing Power Consumption of a Coherent DSP for Metro and Data Center Interconnects,” in *Optical Fiber Communication Conference*, Los Angeles, California, 2017, p. Th3G.2. doi: 10.1364/OFC.2017.Th3G.2.
[93] M. Nazarathy and A. Tolmachev, “Efficient DSP methods for coherent optical receiver,” in *2012 IEEE 27th Convention of Electrical and Electronics Engineers in Israel*, Nov. 2012, pp. 1–4. doi: 10.1109/EEEI.2012.6377095.
[94] R. Nagarajan, I. Lyubomirsky, and O. Agazzi, “Low Power DSP-Based Transceivers for Data Center Optical Fiber Communications (Invited Tutorial),” *J. Lightwave Technol.*, vol. 39, no. 16, pp. 5221–5231, Aug. 2021, doi: 10.1109/JLT.2021.3089901.
[95] T. Hirokawa *et al.*, “Analog Coherent Detection for Energy Efficient Intra-Data Center Links at 200 Gbps Per Wavelength,” *Journal of Lightwave Technology*, vol. 39, no. 2, pp. 520–531, Jan. 2021, doi: 10.1109/JLT.2020.3029788.

[96] M. Morsy-Osman *et al.*, “DSP-free ‘coherent-lite’ transceiver for next generation single wavelength optical intra-datacenter interconnects,” *Opt. Express*, vol. 26, no. 7, p. 8890, Apr. 2018, doi: 10.1364/OE.26.008890.
[97] M. H. Idjadi and F. Aflatouni, “Integrated Pound–Drever–Hall laser stabilization system in silicon,” *Nat Commun*, vol. 8, no. 1, p. 1209, Dec. 2017, doi: 10.1038/s41467-017-01303-y.
[98] V. Coroama, “Investigating the Inconsistencies among Energy and Energy Intensity Estimates of the Internet,” p. 42.
[99] “Cisco visual networking index, forecast and trends 2017-2022_2019_white paper.pdf.”
[100] “Data Centres and Data Transmission Networks, IEA, Paris,” IEA, 2021. [Online]. Available: https://www.iea.org/reports/data-centres-and-data-transmission-networks
[101] K. Kikuchi, “Fundamentals of coherent optical fiber communications,” *J. Lightwave Technol.*, vol. 34, no. 1, pp. 157–179, Jan. 2016, doi: 10.1109/JLT.2015.2463719.
[102] Y. Koizumi, K. Toyoda, M. Yoshida, and M. Nakazawa, “1024 QAM (60 Gbit/s) single-carrier coherent optical transmission over 150 km,” *Opt. Express*, vol. 20, no. 11, p. 12508, May 2012, doi: 10.1364/OE.20.012508.
[103] E. Ip and J. Kahn, “Carrier synchronization for 3-and 4-bit-per-symbol optical transmission,” *Journal of Lightwave Technology*, vol. 23, no. 12, pp. 4110–4124, 2005, doi: 10.1109/JLT.2005.859428.
[104] P. J. Winzer and R.-J. Essiambre, “Advanced Optical Modulation Formats,” *Proc. IEEE*, vol. 94, no. 5, pp. 952–985, May 2006, doi: 10.1109/JPROC.2006.873438.
[105] P. J. Winzer, “High-Spectral-Efficiency Optical Modulation Formats,” *J. Lightwave Technol.*, vol. 30, no. 24, pp. 3824–3835, Dec. 2012, doi: 10.1109/JLT.2012.2212180.
[106] E. Ip, A. P. T. Lau, D. J. F. Barros, and J. M. Kahn, “Coherent detection in optical fiber systems,” *Optics Express*, vol. 16, no. 2, p. 753, 2008, doi: 10.1364/OE.16.000753.
[107] Q. Cheng, M. Bahadori, M. Glick, S. Rumley, and K. Bergman, “Recent advances in optical technologies for data centers: a review,” *Optica*, vol. 5, no. 11, p. 1354, Nov. 2018, doi: 10.1364/OPTICA.5.001354.
[108] X. Z. Xiang Zhou, H. L. Hong Liu, and and R. U. and Ryohei Urata, “Datacenter optics: requirements, technologies, and trends (Invited Paper),” *Chin. Opt. Lett.*, vol. 15, no. 5, pp. 120008–120011, 2017, doi: 10.3788/COL201715.120008.
[109] C. F. Lam, “Optical network technologies for datacenter networks (invited paper),” in *2010 Conference on Optical Fiber Communication (OFC/NFOEC), collocated National Fiber Optic Engineers Conference*, Mar. 2010, pp. 1–3.
[110] A. Singh *et al.*, “Jupiter Rising: A Decade of Clos Topologies and Centralized Control in Google’s Datacenter Network,” in *Proceedings of the 2015 ACM Conference on Special Interest Group on Data Communication*, London United Kingdom, Aug. 2015, pp. 183–197. doi: 10.1145/2785956.2787508.
[111] T. Rokkas, I. Neokosmidis, B. Shariati, and I. Tomkos, “Techno-economic evaluations of 400G optical interconnect implementations for datacenter networks,” presented at the Optical Fiber Communications Conference, 2018. Accessed: Dec. 02, 2021. [Online]. Available: https://www.osapublishing.org/DirectPDFAccess/CDF8F68A-13F9-4866-9B9F9C9EC50652A8_382327/OFC-2018-M1A.1.pdf?da=1&id=382327&uri=OFC-2018-M1A.1&seq=0&mobile=no

[112] Sluyski, Mike A., Gass, Karl, and Stauffer, David R., “Implementation Agreement 400ZR OI-400ZR-01.0,” Optical Internetworking Forum, Mar. 2020. Accessed: Mar. 10, 2021. [Online]. Available: Optical Internetworking Forum
[113] J. K. Perin, A. Shastri, and J. M. Kahn, “Data center links beyond 100 Gbit/s per wavelength,” *Optical Fiber Technology*, vol. 44, pp. 69–85, Aug. 2018, doi: 10.1016/j.yofte.2017.12.006.
[114] F. Derr, “Coherent Optical QPSK Intradyne System: Concept and Digital Receiver Realization,” *Journal of Lightwave Technology*, vol. 10, no. 9, pp. 1290–1296, 1992, doi: 10.1109/50.156881.
[115] S. Beppu, K. Kasai, M. Yoshida, and M. Nakazawa, “2048 QAM (66 Gbit/s) single-carrier coherent optical transmission over 150 km with a potential SE of 153 bit/s/Hz,” *Opt. Express*, vol. 23, no. 4, p. 4960, Feb. 2015, doi: 10.1364/OE.23.004960.
[116] R.-J. Essiambre, G. Kramer, P. J. Winzer, G. J. Foschini, and B. Goebel, “Capacity Limits of Optical Fiber Networks,” *J. Lightwave Technol.*, vol. 28, no. 4, pp. 662–701, Feb. 2010, doi: 10.1109/JLT.2009.2039464.
[117] B. Châtelain *et al.*, “A family of Nyquist pulses for coherent optical communications,” *Opt. Express*, vol. 20, no. 8, p. 8397, Apr. 2012, doi: 10.1364/OE.20.008397.
[118] C. Schmidt *et al.*, “Data Converter Interleaving: Current Trends and Future Perspectives,” *IEEE Communications Magazine*, vol. 58, no. 5, pp. 19–25, May 2020, doi: 10.1109/MCOM.001.1900683.
[119] T. Hirokawa, S. Pinna, J. Klamkin, J. F. Buckwalter, and C. L. Schow, “Energy Efficiency Analysis of Coherent Links for Datacenters,” in *2019 IEEE Optical Interconnects Conference (OI)*, Apr. 2019, pp. 1–2. doi: 10.1109/OIC.2019.8714461.
[120] I. Lyubomirsky, B. Smith, and S. Bhoja, “Leveraging 400G ZR FEC Technology,” p. 10.
[121] T. Pfau, S. Hoffmann, and R. Noe, “Hardware-Efficient Coherent Digital Receiver Concept With Feedforward Carrier Recovery for M-QAM Constellations,” *J. Lightwave Technol.*, vol. 27, no. 8, pp. 989–999, Apr. 2009, doi: 10.1109/JLT.2008.2010511.
[122] K. Liu *et al.*, “36 Hz integral linewidth laser based on a photonic integrated 4.0-meter coil resonator,” *arXiv:2112.09246*.
[123] M. W. Harrington *et al.*, “Kerr soliton microcomb pumped by an integrated SBS laser for ultra-low linewidth WDM sources,” in *Optical Fiber Communication Conference (OFC) 2020*, San Diego, California, 2020, p. T4G.6. doi: 10.1364/OFC.2020.T4G.6.

A. Optical signal-to-noise ratios of Erbium-doped fiber amplifiers